

Theoretische Physik

Capillarity- and Wettability-Dominated Instabilities of Liquids on Solid Substrates

Inaugural-Dissertation
zur Erlangung des Doktorgrades
der Naturwissenschaften im Fachbereich Physik
der Mathematisch-Naturwissenschaftlichen Fakultät
der Westfälischen Wilhelms-Universität Münster

vorgelegt von
Walter Bernard Hans Tewes
aus Höxter

2018



Dekan: Prof. Dr. Michael Klasen

Erster Gutachter: Prof. Dr. Uwe Thiele

Zweiter Gutachter: Prof. Dr. Andreas Heuer

Tag der mündlichen Prüfung: _____

Tag der Promotion: _____

Partly revised version

Kurzzusammenfassung

In der vorliegenden Arbeit werden verschiedene Phänomene theoretisch untersucht, welche in Zusammenhang mit Instabilitäten von dünnen Flüssigkeitsfilmen, Tropfen oder Flüssigkeitskämmen auf festen Substraten stehen. Der Großteil der in der Arbeit verwendeten Modelle basiert dabei auf der sogenannten *Dünnfilmgleichung*. Hierbei handelt es sich um eine nichtlineare, partielle Differentialgleichung, welche die Dynamik des Höhenprofils einer partiell benetzenden viskosen Flüssigkeit auf einem festen Substrat beschreibt. Die Dünnfilmgleichung hat die mathematische Struktur einer Gradientendynamik auf einem effektiven Grenzflächen-Hamiltonian. Letzterer modelliert sowohl die Grenzflächenenergie der Grenzfläche zwischen Flüssigkeit und Gas, als auch, mit Hilfe eines sogenannten *binding potential*, die Benetzbarkeit des Substrates.

Im ersten Teil der Arbeit erläutern wir das Onsagersche Variationsprinzip, welches einen vielseitigen Variationsformalismus mit großer Relevanz für die Theorie weicher Materie und insbesondere dünner Flüssigkeitsfilme darstellt. Des Weiteren zeigen wir eine Herleitung der Dünnfilmgleichung mit besonderem Augenmerk auf dem Variationsprinzip, welches den hydrodynamischen Gleichungen zu Grunde liegt.

Im zweiten Teil der Arbeit wird zunächst eine Dünnfilmgleichung verwendet, um Plateau-Rayleigh Instabilitäten von Flüssigkeitskämmen auf chemisch streifenförmig vorstrukturierten Substraten zu untersuchen. Hierbei werden insbesondere Instabilitäten von zwei wechselwirkenden Flüssigkeitskämmen betrachtet. Für die Instabilität einzelner Flüssigkeitskämme werden Ergebnisse der Dünnfilmgleichung mit entsprechenden Ergebnissen aus kinetischen Monte-Carlo- (KMC) Simulationen qualitativ, jedoch systematisch, verglichen. Als einen ersten Schritt hin zu einem quantitativen Abbilden von KMC Simulationen auf ein Modell ähnlich der Dünnfilmgleichung, zeigen wir des Weiteren ein neues numerisches Verfahren zur Berechnung eines binding potential aus einer Dichtefunktionaltheorie (DFT).

Im dritten Teil der Arbeit werden verschiedene Phänomene diskutiert, die in Zusammenhang mit Frontpropagation von Instabilitäten in Flüssigkeitsstrukturen stehen. Hier untersuchen wir zunächst die Ausbreitung von Instabilitäten in dünnen Flüssigkeitsfilmen auf horizontalen Substraten mit Hilfe einer *marginalen Stabilitätsanalyse*. Auch die Propagation von Plateau-Rayleigh Instabilitäten von Flüssigkeitskämmen wird mit Hilfe dieser Methode analysiert. Des Weiteren wird ein Modell für *dip-coating* mit partiell benetzenden Flüssigkeiten eingeführt. Im Rahmen dieses Modells diskutieren wir einen speziellen Lösungstyp, welcher einer periodischen Ablagerung von Flüssigkeitsstreifen parallel zum Meniskus entspricht. Diese zeitperiodischen Lösungen werden in Zusammenhang mit der zuvor erwähnten Frontpropagation von Instabilitäten sowie mit Hilfe von numerischer Kontinuierung theoretisch analysiert.

Im letzten Teil der Arbeit stellen wir zwei verschiedene Methoden zur grobkörnigen Beschreibung von verschiedenen Phänomenen im Kontext getriebener Tropfen vor. Zum Einen modellieren wir die in großskaligen Zeitsimulationen eines Dünnfilmmodells gefundene Vergrößerungsdynamik in einem Ensemble von rutschenden Tropfen mit Hilfe einer verallgemeinerten *Smoluchowski-Koagulationsgleichung*. Letztere beschreibt die zeitliche Entwicklung der Tropfengrößenverteilung. Die Gleichung baut auf Informationen aus der Pfad-Kontinuierung

einzelner rutschender Tropfen auf und ermöglicht insbesondere eine quantitative Modellierung der Zeitentwicklung der Anzahl von Tropfen im Ensemble.

Das zweite betrachtete System besteht aus einem Tropfen einer partiell benetzenden Flüssigkeit auf einem rotierenden Zylinder. In Abhängigkeit von der Rotationsgeschwindigkeit des Zylinders kann der Tropfen entweder durch die Schwerkraft gepinnt sein oder, mit einer eigenen Geschwindigkeit, angetrieben durch den Zylinder, rotieren. Ausgehend von einer Dünnschichtgleichung für dieses Modellsystem leiten wir eine gewöhnliche Differentialgleichung für die Position des Tropfens ab. Diese Differentialgleichung ist für den Grenzfall sehr kleiner Verformungen des Tropfens durch die Gravitation gültig und zeigt hier eine bemerkenswerte Übereinstimmung mit Ergebnissen aus der Kontinuierung und Zeitsimulationen des entsprechenden Dünnschichtmodells.

Abstract

In the present thesis, we theoretically investigate a number of phenomena related to instabilities of thin liquid films, drops and ridges on solid substrates. Most of the considered models are based on the so-called *thin-film equation*. Here, this equation is a nonlinear partial differential equation for the time evolution of the height profile of a viscous partially wetting liquid on a solid substrate. Furthermore, the thin-film equation has the mathematical structure of a gradient dynamics on an effective interface Hamiltonian, which models the liquid-gas interfacial energy and, in terms of a so-called *binding potential*, also the wettability of the substrate.

In the first part, we review *Onsager's variational principle* as a general variational formalism which is highly relevant for soft matter modeling and, in particular, thin-film models. With an emphasis on the variational principle underlying the basic hydrodynamic equations, we then review the derivation of the thin-film equation.

In the second part, a thin-film model is then employed to investigate Plateau-Rayleigh instabilities of ridges on stripe-prepatterned substrates with a special focus on coupled instabilities of two adjacent liquid ridges. Results of the thin-film modeling of the instability of a single ridge are compared qualitatively but in a systematic way with corresponding results from kinetic Monte Carlo (KMC) simulations. As a first step towards a quantitative mapping of KMC to a thin-film type model, we present a novel numerical approach to the extraction of a binding potential from a microscopic density functional theory (DFT).

In the third part, we discuss phenomena related to the propagation of instabilities of liquid structures. We first apply a marginal stability analysis to the spreading of dewetting instabilities into linearly unstable flat films of small film height and to the propagation of Plateau-Rayleigh instabilities of ridges on substrates. We then introduce a model for dip-coating employing a partially wetting liquid, which exhibits spinodal dewetting for small film heights. Here, we investigate a particular solution type corresponding to deposition of a periodic array of liquid ridges at and parallel to the meniscus. These time-periodic solutions are investigated in terms of a theoretical analysis relying on the aforementioned phenomenon of front propagation and additionally through path continuation of time-periodic solutions.

In the final part, we present two different coarse graining procedures for the description of different phenomena occurring for driven droplets. For the modeling of coarsening in a large ensemble of sliding droplets as observed in large scale simulations of a thin-film model, we formulate an augmented Smoluchowski coagulation equation for the time evolution of the droplet size distribution. This equation relies on information obtained from numerical continuation of individual sliding droplets and is able to quantitatively reproduce the time evolution of the number of droplets. The second considered system is a droplet of partially wetting liquid on a rotating cylinder. Depending on the rotation speed, the droplet is either pinned on the lower part of the cylinder due to gravity or depinned and co-rotating with the cylinder, though at its own speed. Starting from a thin-film model, we formulate an ordinary differential equation for the position of the droplet. This order parameter equation is valid in the limit of a small influence of gravity on the deformation of the droplet and shows remarkably good agreement with results from continuation and numerical time simulation of the thin-film model.

Contents

Kurzzusammenfassung	v
Abstract	vii
Contents	xi
1 Introduction	1
1.1 Capillarity and Wettability	1
1.2 Levels of Description and Methods	2
1.3 Outline of the Thesis	3
2 Onsager's Variational Principle	5
2.1 Introduction of Onsager's Variational Principle	5
2.1.1 Lagrangian Formalism and Rayleigh's Dissipation Function	5
2.1.2 Onsager's Variational Principle and Gradient Dynamics	7
2.2 Coarse Graining Based on Onsager's Variational Principle	8
2.2.1 Equivalence to a Projection Approach	8
2.2.2 Quasistatic Approximations	9
2.3 Onsager's Variational Principle in Soft Matter and Pattern Formation	10
2.3.1 Particle Diffusion and DDFT	10
2.3.2 Conserved and Non-Conserved Order Parameter Equations	12
2.4 Variational Derivation of Amplitude Equations	13
2.4.1 Swift-Hohenberg Equation	13
2.4.2 Conserved Swift-Hohenberg Equation	14
2.5 Conclusion	16
3 The Thin-Film Equation	19
3.1 Stokes Flow of a Viscous Liquid on a Solid Substrate	19
3.1.1 Stokes Equations from a Variational Principle	19
3.1.2 Viscous Liquid with a Liquid-Gas Interface on a Solid Substrate	20
3.2 Long-Wave Reduction and the Thin-Film Equation	23
3.2.1 Monge Parametrization of the Liquid-Gas Interface	23
3.2.2 Long-Wave Approximation	24
3.2.3 Generalizations of the Thin-Film Equation	25

4	Instabilities of Liquid Ridges on Heterogeneous Substrates - Thin-Film Modeling and Comparison to KMC	29
4.1	Introduction and Experiments	29
4.2	Thin-Film Modeling	30
4.2.1	Model Binding Potential	30
4.2.2	Numerical Methods	31
4.2.3	Steady State Solutions	32
4.2.4	Transversal Stability of a Single Ridge	34
4.2.5	Transversal Stability of Two Adjacent Ridges	38
4.2.6	Coarsening and Transversal Instabilities	40
4.3	Comparison of Kinetic Monte Carlo Modeling and Thin-Film Modeling	44
4.3.1	KMC Modeling	44
4.3.2	Plateau-Rayleigh Instabilities in the KMC Model - Comparison to Thin-Film Modeling	45
4.4	Towards a Mapping of KMC to Effective Interface Models	49
4.4.1	Thermodynamics of a Liquid Film on a Solid Substrate – The Binding Potential	49
4.4.2	Lattice Gas DFT	50
4.4.3	NEB Approach to the Calculation of Binding Potentials	52
4.4.4	Outlook: Mapping of Mean Field Dynamics to Effective Interface Dynamics	54
4.5	Conclusion	55
5	Propagation of Instabilities	57
5.1	Pulled Fronts in Free Surface Liquids	57
5.1.1	Pulled Patterning Fronts	57
5.1.2	Marginal Stability Analysis for Flat Linearly Unstable Liquid Films	59
5.1.3	Propagating Spinodal Dewetting Fronts Without Gravity	60
5.1.4	Propagating Plateau-Rayleigh Instabilities	66
5.2	Controlled Dewetting Patterns in a Dip-Coating Geometry	69
5.2.1	Steady State Solutions and the Landau–Levich Transition	69
5.2.2	Space-Time Periodic Solutions – Phase Diagram and Analysis	72
5.2.3	Numerical Continuation of Time-Periodic Solutions	74
5.2.4	2D Simulations	77
5.3	Conclusion	78

6	Statistical and Analytical Coarse Graining	79
6.1	Statistical Description of Sliding Drop Ensembles	79
6.1.1	Statistical Results from NTS and Connection to Bifurcations of Single Drops	80
6.1.2	Statistical Model	84
6.2	Order Parameter Equation For a Drop of Partially Wetting Liquid on a Rotating Cylinder	88
6.2.1	Model Equation	88
6.2.2	First Derivation of the Order Parameter Equation	90
6.2.3	Second Derivation of the Order Parameter Equation	93
6.2.4	Results of the Order Parameter Equation and Outlook	94
6.3	Conclusion	96
7	Summary and Conclusion	97
	List of Publications	99
	Bibliography	101

1 Introduction

Liquid structures which exhibit a free surface, e.g., a liquid-gas interface, are ubiquitous not only in nature and technology but also in our daily lives. One important subclass of these structures are liquids on solid surfaces.¹ Equally common are instabilities of such liquids: On a daily basis, we experience the breakup of rivulets flowing in the kitchen sink or intricate patterns resulting from the rupture and retraction of liquids (*dewetting*) which were cast intentionally or unintentionally on a solid surface. A deeper understanding of such instabilities might not only gratify our curiosity, but is also crucial for their control in technological systems. For instance, in the process of coating surfaces, dewetting is typically not desirable, while in other circumstances surfaces are treated specifically for the purpose of being repelling to water or other liquids. Furthermore, the control of the motion of liquid droplets on surfaces is important in a technological context, e.g., in microfluidic devices.

1.1 Capillarity and Wettability

The present thesis is concerned with liquids that are in good approximation free of inertia. Physically speaking, we are considering liquids and systems, for which the so-called *Reynolds number* $Re = \frac{uL}{\nu} \ll 1$. Here, u and L are characteristic velocity and length scales and ν is the kinematic viscosity of the liquid [LL91]. In a free surface geometry on a solid substrate, the dynamics and the statics of these liquids are dominated by energetic quantities. The energy which is directly related to the geometry of the free surface is the interfacial energy of the liquid-gas interface. The interfacial energy per area of the interface is called *surface tension*. Effects of surface tension of the liquid-gas interface are often referred to as phenomena of *capillarity* [dGBWQ04]. The minimization of the surface energy of a free surface reduces, for a constant surface tension, to a minimization of the surface area. The tendency of free surface liquids to perform such a minimization is the basic idea behind important classic theories for the shape, motion and instabilities of the liquids. One example is the classical theory by J. A. F. Plateau [Pla73] and by Lord Rayleigh [Str78] for the breakup of liquid jets into droplets. When a liquid is in contact with a solid and especially for the case where a three phase (solid-liquid-gas) contact line is present, it is not the liquid-gas interfacial energy that is minimized but the combination of liquid-gas, solid-liquid and solid-gas interfacial energies. This brings us to the concept of *wettability*. By a simple geometrical argument, one finds that the *equilibrium contact angle* θ_{eq} resulting from a minimization of the aforementioned energies is given by the famous *Young-Dupré* law [Doi13]:

$$\gamma_{\text{lg}} \cos(\theta_{\text{eq}}) = \gamma_{\text{sg}} - \gamma_{\text{sl}}, \quad (1.1)$$

where γ_{lg} , γ_{sg} and γ_{sl} are the liquid-gas, solid-gas and solid-liquid surface tensions, respectively. Typically, a liquid that exhibits an equilibrium contact angle $0^\circ < \theta_{\text{eq}} < 180^\circ$ is denoted as

¹In the following, we will adopt a more technical nomenclature, and will often not talk of solid surfaces but rather of *substrates*.

partially wetting (cf. FIG. 1.1). The remaining extreme cases are *completely wetting* ($\theta_{\text{eq}} = 0^\circ$) and *non-wetting* liquids ($\theta_{\text{eq}} = 180^\circ$). In this thesis, we are concerned with the case of partially wetting liquids exhibiting a small equilibrium contact angle.

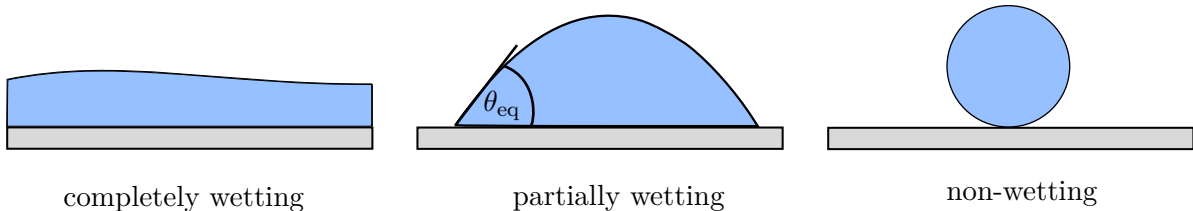


Figure 1.1: Sketch of different wetting scenarios.

1.2 Levels of Description and Methods

In this thesis, several different levels of description are employed to model liquids on substrates. A variety of methods accounts for different scales involved in the considered phenomena. We now shortly review important approaches that are typically used in the modeling of such liquid structures. A part of these approaches is also discussed in the present thesis as will be clarified in the outline in §1.3.

The most detailed level of description employed in soft matter modeling is formed by particle based numerical simulations like atomistic or coarse-grained molecular dynamics (MD) simulations [KN17, SW09, KLRD06, TMTT13, IT07, KPB02], and kinetic Monte Carlo (KMC) simulations [LMW⁺12, RRGB03, SHR05, CSA17b]. There are different reasons why the modeling of liquids on substrates on the level of particles might be of interest: On the one hand, as we will shortly discuss in §3.2.3, a purely hydrodynamic treatment of mesoscopic or macroscopic amounts of liquids that exhibit a moving three-phase contact line is problematic. Here, particle-based simulations give further insight into the processes on the microscopic scale that are relevant at the contact line (cf. [QWL⁺09]). On the other hand, the entirety of the liquid structure of interest might be on a sufficiently small scale motivating a comparison of continuum modeling to results from particle-based simulations. This is the case, e.g., for the modeling of the experiments described in [WC12, WDW⁺11] which are the motivation for the work outlined in Chap. 4.

The averaged features of stochastic particle-based models can be captured by density functional theory (DFT) for the equilibrium case [HTA17, Eva79] and also, as developed in the two recent decades, for dynamically evolving systems close to equilibrium (DDFT) [CSA17a, AR04, MT99]. These are thermodynamic theories which rely on the formulation of a Helmholtz free energy or grand potential, which is a functional of the local density of particles.

Based on a thermodynamic model, the wetting behavior of liquids on solid substrates can be described by the so-called *binding potential*, which corresponds to an excess energy associated with the local adsorption (or film height) on the substrate. Such binding potentials are particularly important for the description of the contact line region and can be extracted from microscopic theories [TMTT13] and, in particular, from DFT [HTA17].

Once a binding potential is found, the statics and dynamics of liquid structures that are sufficiently shallow can be modeled based on an *effective interface Hamiltonian* [HTA15, MBKP14], which combines interfacial energies of the liquid-gas interface and wetting energies (encoded in

the binding potential) and is typically a functional of a height function describing the liquid-gas interface in a Monge representation. The statics of liquid structures can be calculated by a (constrained-) minimization of the effective interface Hamiltonian, while their dynamics can be modeled as a gradient dynamics on the latter.

A special case of gradient dynamics on an effective interface Hamiltonian is the so-called *thin-film equation* [ODB97, Mit93, CM09, Thi07, Thi10]. This equation is derived from macroscopic hydrodynamics and can be supplemented by the aforementioned binding potential. The fundamental assumption for the derivation of the thin-film equation is that the height of the liquid on the substrate varies only slowly and a *long-wave approximation* (also often referred to as *lubrication approximation*) can be employed. In this case and for sufficiently low Reynolds numbers, the solving of the thin-film equation represents an alternative to full scale hydrodynamic simulations, where Stokes equations have to be solved in combination with a free boundary problem resulting from the modeling of the liquid-gas interface. Variants of the thin-film equation, which is a partial differential equation (PDE) describing the time evolution of the local height of the liquid on the substrate, constitute the major part of the models discussed in the present thesis. Although we are able to model dynamics and instabilities of liquids on a macroscopic scale by numerical time simulations (NTS) of the thin-film equation, further coarse-grained models are still desirable. These can be statistical models, like a Smoluchowski-type equation for ensembles of droplets or order parameter equations for the motion and deformation of single droplets.

Since the majority of the models treated in this thesis are nonlinear PDEs, a numerical approach is inevitable. The general numerical approach we chose is twofold. On the one hand, we conduct numerical simulations of the time evolution, where we employ the generic finite element framework DUNE PDE-Lab [BHM10, BBD⁺08b, BBD⁺08a]. On the other hand, much information about the systems under consideration can be obtained by the investigation of the steady state solutions and their bifurcations. Therefore, we also employ numerical path continuation, which is an efficient tool to track solutions and bifurcations in parameter space [DWC⁺14, EGU⁺18]. Here we use the software package AUTO-07p [DOO12, DKK91a, DKK91b]. Results obtained by numerical continuation can then also be used for further semi-analytical approaches and statistical modeling.

1.3 Outline of the Thesis

In Chap. 2, we are concerned with *Onsager's variational principle* as a general theoretical concept which allows for the formulation of a variety of dynamical equations in the overdamped limit. Its usefulness in the context of soft matter has been recently pointed out and reviewed in [Doi11, Doi12]. It can be seen as an extension of variational principles based on energies in the static case to the dynamical case through the consideration of energy dissipation. In particular, we discuss the use of Onsager's variational principle for coarse graining (cf. [Doi15]) and the formulation of general model equations in pattern formation theory based on the principle.

In Chap. 3, we first elaborate how the hydrodynamic equations of a two-phase fluid on a solid substrate can be formulated based on Onsager's variational principle. We then outline a derivation of the thin-film equation which inherits a variational structure from the hydrodynamic equations and is thus a gradient system. Furthermore, generalizations of the thin-film equation are introduced, which are of importance in the subsequent parts of the thesis.

In Chap. 4, the thin-film equation is employed to investigate Plateau-Rayleigh instabilities of liquid ridges on chemically prepatterned substrates. Motivating experiments [WDW⁺11, WC12] exhibit ridges which are on a very small scale (~ 100 nm height) and we therefore compare results from thin-film modeling with kinetic Monte Carlo simulations in a qualitative, yet systematic way. As a first step towards the quantitative mapping of KMC simulations to gradient dynamics on an interface Hamiltonian, we then present a novel numerical method for the extraction of a binding potential from a mean field DFT relevant for the statistically averaged KMC model.

In the subsequent chapter, we analyze a specific mode of growth of instabilities in liquids on solid substrates, namely the propagation of instability fronts. These are discussed in the framework of a so-called *marginal stability analysis* of *pulled fronts*, a concept which is well established in pattern formation theory. Additionally, we discuss time-periodic solutions that can be found in a dip-coating geometry with simple liquids and a destabilizing binding potential. Here, one boundary of the parameter space region where time-periodic solutions, corresponding to line deposition at and parallel to the meniscus, emerge can be related to results from the investigation of pulled instability fronts.

In the final chapter, we discuss two different coarse graining approaches for the description of driven liquids. In the first part of the chapter, we formulate a statistical model for the coarsening of sliding droplets. The model relies on information obtained from the numerical continuation of individual droplets. In the second part, we derive a simple order parameter equation describing the pinning and depinning of a liquid droplet on a rotating cylinder. In this context, we once again return to Onsager's variational principle and its benefits for compact derivations of reduced dynamical equations.

2 Onsager's Variational Principle

Pioneered by P. de Fermat with his famous principle in geometrical optics (*Fermat's principle* [LL66a]), the use of *variational* or *extremal principles* is widespread in theoretical physics [Bas07]. Well known extremal principles in a static (or equilibrium) context are, e.g., the *Rayleigh-Ritz principle* [Rit09] employed in quantum mechanics and the *Gibbs-Bogoliubov principle* in equilibrium thermodynamics [HTA14]. The most prominent example for a variational principle in a time-dependent context is the *principle of least action* which is intimately related to the Lagrangian formulation of classical mechanics [LL66b].

In this chapter, we discuss *Onsager's variational principle* for dissipative systems which arises in overdamped classical mechanics but also in the description of thermodynamic order parameters close to equilibrium, as is demonstrated in [Ons31a, Ons31b]. We first show how the principle is obtained in classical mechanics [Doi15, Gla05], then discuss a more general formulation as well as its relation to *gradient dynamics* and finally focus on coarse graining of dynamical equations based on the variational principle: As in the case of, e.g., the Rayleigh-Ritz principle, Onsager's variational principle can be conveniently used to obtain approximations through the formulation of parametrized ansatz functions. This has been recently pointed out in [Doi15] and previously also in [Gla05].

In the formulation of the variational formalism (§2.1.2-§2.2.2), for reasons of clarity, a discrete, finite set of order parameters is considered (as also in, e.g., [Doi11]). Applications of the principle are then shown for spatially extended systems. In the first part (§2.1-§2.2) of the present chapter, we mainly reproduce and sometimes elaborate ideas presented in [Doi16, Doi15, Doi12, Doi13, Gla05], an application of the coarse graining procedure is then shown for two prototype pattern-forming systems in §2.4.

2.1 Introduction of Onsager's Variational Principle

2.1.1 Lagrangian Formalism and Rayleigh's Dissipation Function

We start with a short review of the Lagrangian formulation for a mechanical system with constraints and under the influence of friction [Gol80]. More specifically, we consider a N -particle system subject to conservative forces \mathbf{F}_i , constraint forces \mathbf{F}_i^c and friction forces (with friction coefficients γ_i) such that Newton's equations of motion for the positions $\{\mathbf{r}_i \in \mathbb{R}^3, i = 1 \dots N\}$ read:

$$m_i \ddot{\mathbf{r}}_i + \gamma_i \dot{\mathbf{r}}_i = \mathbf{F}_i + \mathbf{F}_i^c, \quad i = 1 \dots N. \quad (2.1)$$

We now introduce generalized coordinates $\{q_j, j = 1, \dots, M \leq 3N\}$ in accordance with the constraints on the system, i.e., which parametrize, in the space spanned by the physical particle positions $\{\mathbf{r}_i\}$, a submanifold on which the constraints on the system are fulfilled.

We proceed to project Newton's equations (2.1) onto an infinitesimal displacement of the system tangential to the constraint manifold (often termed *virtual displacement*):

$$\sum_{i=1}^N (m_i \ddot{\mathbf{r}}_i + \gamma_i \dot{\mathbf{r}}_i - \mathbf{F}_i - \mathbf{F}_i^c) \cdot \delta \mathbf{r}_i = 0, \text{ where } \delta \mathbf{r}_i = \sum_{j=1}^M \frac{\partial \mathbf{r}_i}{\partial q_j} \delta q_j. \quad (2.2)$$

Physically speaking, *d'Alembert's principle* now states that the overall work done by the constraint forces along such displacement vanishes identically:

$$\sum_{i=1}^N \mathbf{F}_i^c \cdot \delta \mathbf{r}_i = 0. \quad (2.3)$$

Making use of the identity $\frac{\partial \mathbf{r}_i}{\partial q_j} = \frac{\partial \dot{\mathbf{r}}_i}{\partial \dot{q}_j}$, it can be seen by some straightforward calculation (cf. [Gol80]) that

$$\sum_{j=1}^M \left(\frac{d}{dt} \frac{\partial \mathcal{L}}{\partial \dot{q}_j} - \frac{\partial \mathcal{L}}{\partial q_j} + \frac{\partial \mathcal{D}}{\partial \dot{q}_j} \right) \delta q_j = 0, \quad (2.4)$$

where we introduced the *Lagrangian*

$$\mathcal{L} := K - V = \sum_{i=1}^N \frac{1}{2} m_i \dot{\mathbf{r}}_i^2 - V, \text{ with } \mathbf{F}_i = -\nabla_i V, \quad (2.5)$$

with the kinetic energy K and the potential V as well as the *Rayleigh dissipation function* [Str94]

$$\mathcal{D} := \sum_{i=1}^N \frac{1}{2} \gamma_i \dot{\mathbf{r}}_i^2 = \sum_{j=1}^M \frac{1}{2} \tilde{\gamma}_j(\{q_i\}) \dot{q}_j^2. \quad (2.6)$$

Finally, for the case of *holonomic constraints*, i.e., if each variation δq_i is independent from the others, from (2.4) the *Lagrangian equations of motion* including friction forces are obtained:

$$\frac{d}{dt} \frac{\partial \mathcal{L}}{\partial \dot{q}_j} - \frac{\partial \mathcal{L}}{\partial q_j} + \frac{\partial \mathcal{D}}{\partial \dot{q}_j} = 0, \text{ for } j = 1, \dots, M. \quad (2.7)$$

Some remarks are in order concerning the introduction of the Rayleigh dissipation function to incorporate terms stemming from friction into the Lagrangian formalism:

While the Lagrangian equations of motion without dissipative forces are associated with a variational (extremum) principle, namely *Hamilton's principle of least action*, this is in general no longer the case for the set of equations (2.7). However, as will be discussed next, a different variational principle arises for the case of overdamped systems. Furthermore, as for the conservative Lagrangian equations, the extended Lagrangian formulation allows for a convenient way to rewrite the equations of motion for a given equivalent set of generalized coordinates, i.e., for all sets of coordinates q_i which can be varied independently and fully describe the system in accordance to the constraints, the equations of motion have the form (2.7). This property of the Lagrangian formulation, which persists even when an extremum principle is missing proves very useful for practical calculations as is discussed for mechanical systems in [Min15].

In the case of overdamped systems, i.e., for $\frac{m_i}{\gamma_i} \ll 1$, the contribution stemming from the kinetic energy of the system can be neglected and equations (2.7) reduce to

$$\frac{\partial V}{\partial q_j} + \frac{\partial \mathcal{D}}{\partial \dot{q}_j} = 0, \text{ for } j = 1, \dots, M. \quad (2.8)$$

By introducing the function

$$\mathcal{R} = \frac{d}{dt}V + D = \sum_{j=1}^M \frac{\partial V}{\partial q_j} \dot{q}_j + \sum_j \frac{1}{2} \tilde{\gamma}_j(\{q_i\}) \dot{q}_j^2, \quad (2.9)$$

these equations can be reformulated as (cf. [Gla05])

$$\frac{\partial \mathcal{R}}{\partial \dot{q}_j} = 0, \text{ for } j = 1, \dots, M, \quad (2.10)$$

which is a special case of Onsager's variational principle which we will now discuss in general.

2.1.2 Onsager's Variational Principle and Gradient Dynamics

Consider a set of variables $\mathbf{X} = (X_1, \dots, X_N)$ describing a nonequilibrium system such that their time evolution can be written as¹ [Doi13]:

$$\dot{X}_i = -\xi_{ij}^{-1}(\mathbf{X}) \frac{\partial E}{\partial X_j}, \text{ for } i = 1, \dots, N, \quad (2.11)$$

where E is the energy of the system, $\boldsymbol{\xi} = (\xi_{ij})_{i,j=1,\dots,N}$ is the dissipation matrix², which in general depends on \mathbf{X} , and $\boldsymbol{\xi}^{-1}$ is the inverse of $\boldsymbol{\xi}$. We now require the dissipation matrix $\boldsymbol{\xi}$ and thus also its inverse to be *symmetric* and *positive definite* for all values of \mathbf{X} :

$$\xi_{ij} y_i y_j > 0, \text{ for all } \mathbf{y} \in \mathbb{R}^N, \text{ and } \xi_{ij} = \xi_{ji}, \quad i, j = 1, \dots, N. \quad (2.12)$$

With the definition of the Rayleighian

$$\mathcal{R} := \frac{\partial E}{\partial X_i} \dot{X}_i + \frac{1}{2} \xi_{ij} \dot{X}_i \dot{X}_j =: \frac{d}{dt}E + \mathcal{D} \quad (2.13)$$

where \mathcal{D} is the dissipation function, the evolution equation (2.11) can then be recast in the variational form

$$\frac{\partial \mathcal{R}}{\partial \dot{X}_i} = 0, \text{ for } i = 1, \dots, N, \quad (2.14)$$

since

$$\frac{\partial}{\partial \dot{X}_i} \left(\frac{\partial E}{\partial X_\nu} \dot{X}_\nu + \frac{1}{2} \xi_{\mu\nu} \dot{X}_\mu \dot{X}_\nu \right) = \frac{\partial E}{\partial X_i} + \frac{1}{2} (\xi_{\mu i} \dot{X}_\mu + \xi_{i\nu} \dot{X}_\nu) = \frac{\partial E}{\partial X_i} + (\xi_{\mu i} \dot{X}_\mu). \quad (2.15)$$

¹ In the following, we use Einstein's sum convention, i.e., we sum over all indices appearing twice in one expression.

² We assume the dissipation matrix to be invertible. If this is not the case, we can diagonalize the matrix and consider the dynamics of the complement of its kernel.

The time evolution of nonequilibrium state variables of the form (2.5) with the condition (2.12) was shown by L. Onsager to be highly relevant for nonequilibrium thermodynamics. In the context of his seminal work [Ons31a, Ons31b], the symmetry of the matrix $\boldsymbol{\xi}$ is known under the term of *Onsager reciprocal relations*. In [Ons31a, Ons31b], L. Onsager also points out the fact stated above that the positive definiteness and symmetry of $\boldsymbol{\xi}$ implies a variational principle. Not only in the context of classical mechanics and of nonequilibrium thermodynamics, governing equations can often be written in the form (2.5),(2.12), but also for hydrodynamic systems in the highly viscous limit. The formulation of hydrodynamic model equations based on Stokes equation will be subject of Chap. 3. The relevance of the variational principle for the formulation of model equations in soft matter physics in general was recently emphasized in [Doi11], where various examples are given, part of which will also be shown in the present chapter.

From a geometric point of view, the dissipation matrix $\boldsymbol{\xi}$ can be interpreted as a metric tensor associated with the symmetric bilinear form [Gla05]

$$\langle \mathbf{Y}, \mathbf{Z} \rangle_{\boldsymbol{\xi}(\mathbf{X})} := \xi_{ij}(\mathbf{X}) Y_i Z_j. \quad (2.16)$$

The right hand side of equation (2.11) is then the negative gradient of the energy E induced by the metric tensor:

$$\dot{X}_i = -(\nabla_{\boldsymbol{\xi}} E)_i = -\xi_{ij}^{-1}(\mathbf{X}) \frac{\partial E}{\partial X_j}. \quad (2.17)$$

Equation (2.11) is therefore a gradient dynamics on the energy E with respect to a gradient corresponding to a, in general, non-euclidean geometry specified by the dissipation function. As it is in general the case for gradient dynamics, the energy E is always decreasing in time until a fixed point of the system (i.e., an equilibrium) is reached.

2.2 Coarse Graining Based on Onsager's Variational Principle

2.2.1 Equivalence to a Projection Approach

We will now discuss the formulation of reduced dynamical equations based on the variational principle (2.14). The efficiency of the variational principle for coarse graining is outlined in detail in [Doi15], its relation to a *Galerkin-type reduction* is shown in [Gla05]. Here, we first show the general Galerkin-type reduction, following [Gla05] and then discuss the coarse graining procedure based on a perturbed energy function as a possible guide to identifying good approximating coarse-grained variables.

The use of variational principles for the calculation of approximations is a common concept in theoretical physics. One prominent example is the use of the *Rayleigh-Ritz variational principle* for the approximate calculation of eigenfunctions and eigenvalues of Schrödinger's equation. The basic approach is typically to formulate parametrized ansatz functions and then perform variations only with respect to the small set of parameters. For the dynamical system (2.14) a corresponding approach is to use the following ansatz:

$$\mathbf{X}(t) = \mathbf{X}_0(\mathbf{q}(t)), \text{ where } \mathbf{X}(t) \in \mathbb{R}^N \text{ and } \mathbf{q}(t) \in \mathbb{R}^M, M < N, \quad (2.18)$$

i.e., to formulate a parametrized ansatz for the dynamical solution, where the time dependence is assigned exclusively to the parameters (or coarse-grained variables). The time evolution of

the coarse-grained variables \mathbf{q} is then obtained through the variational principle by evaluation of

$$\frac{\partial \mathcal{R}_0}{\partial \dot{q}_i} = 0, \text{ for } i = 1, \dots, M, \text{ where } \mathcal{R}_0(\mathbf{q}, \dot{\mathbf{q}}) := \mathcal{R}\left(\mathbf{X}_0(\mathbf{q}), \frac{d}{dt}\mathbf{X}_0(\mathbf{q})\right). \quad (2.19)$$

The variation with respect to \dot{q}_i in equation (2.19) is in fact a projection of the original set of equations (2.14) evaluated at $(\mathbf{X}, \dot{\mathbf{X}}) = (\mathbf{X}_0, \dot{\mathbf{X}}_0)$ onto a direction tangential to the reduced manifold specified by $\frac{\partial \mathbf{X}_0}{\partial q_i}$:

$$\frac{\partial \mathcal{R}_0}{\partial \dot{q}_i} = \frac{\partial X_{0j}}{\partial q_i} \frac{\partial \mathcal{R}}{\partial \dot{X}_j} \Big|_{(\mathbf{X}_0, \dot{\mathbf{X}}_0)} = 0. \quad (2.20)$$

In terms of the equivalent gradient systems formulation, the reduction amounts to [Gla05]

$$\dot{q}_j \left\langle \frac{\partial \mathbf{X}_0}{\partial q_i}, \frac{\partial \mathbf{X}_0}{\partial q_j} \right\rangle_{\xi(\mathbf{X}_0)} = - \frac{\partial X_{0j}}{\partial q_i} \frac{\partial E}{\partial X_j} \Big|_{\mathbf{X}_0} = - \left\langle \frac{\partial \mathbf{X}_0}{\partial q_i}, \nabla_{\xi} E \Big|_{\mathbf{X}_0} \right\rangle_{\xi(\mathbf{X}_0)} \quad (2.21)$$

$$\Leftrightarrow \dot{\mathbf{q}} = -\nabla_{\zeta} E(\mathbf{X}_0(\mathbf{q})). \quad (2.22)$$

Here, $\zeta = \zeta(\mathbf{q})$ is the so-called *induced metric tensor* on the restricted submanifold specified by $\mathbf{X}_0(\mathbf{q})$ and reads

$$\zeta_{ij} = \left\langle \frac{\partial \mathbf{X}_0}{\partial q_i}, \frac{\partial \mathbf{X}_0}{\partial q_j} \right\rangle_{\xi(\mathbf{X}_0)} = \xi_{\mu\nu} \frac{\partial X_{0\mu}}{\partial q_i} \frac{\partial X_{0\nu}}{\partial q_j}. \quad (2.23)$$

Through (2.21), we recognize that performing the variation of the Rayleighian \mathcal{R} with respect to the reduced variable q_i is equivalent to inserting the ansatz (2.18) into (2.11) and then, subsequently, projecting the resulting equation onto the mode $\frac{\partial \mathbf{X}_0}{\partial q_i}$ with respect to the metric $\xi(\mathbf{X}_0)$. Furthermore, the resulting reduced equations are obviously still a gradient system, where now the gradient of the energy is evaluated according to the metric $\zeta(\mathbf{q})$ induced by the restriction to the submanifold.

2.2.2 Quasistatic Approximations

While it is now shown that the coarse graining through a reduced variation is a convenient way to perform a Galerkin-type approximation [Gla05], an open question remains how to choose a good parametrized ansatz (2.11). The basic assumption behind the ansatz (2.11) is the existence of a slow manifold [Hak04], such that the system exhibits a separation of timescales, where it relaxes quickly onto the slow manifold and then slowly follows the latter approximately until it reaches a steady state [Gla05]. We now outline the special case (which will however be relevant in §6.2.3) where the overall energy can be written as

$$E = E_0 + \varepsilon E_1, \text{ where } \varepsilon \ll 1, \quad (2.24)$$

where a continuous family of minima $\mathbf{X}_0(\mathbf{q})$ of the energy E_0 is known and εE_1 is treated as a perturbation.³ We consider the ansatz

$$\mathbf{X}(t) = \mathbf{X}_0(\mathbf{q}(\tau)) + \varepsilon \mathbf{X}_1(\tau), \text{ where } \tau = \varepsilon t, \quad (2.25)$$

³ Note that the relevant quantity for the perturbation is the gradient of E_1 and not the absolute value, thus we also assume that ∇E_1 is of the same order of magnitude as ∇E_0 .

accounting for the fact stated above that we assume the system to move on a slow timescale τ on the submanifold given by the steady solution family of the unperturbed system and allowing for small correction terms $\varepsilon \mathbf{X}_1$. After introducing this ansatz in the Rayleighian (2.13), we get

$$\mathcal{R} = \frac{1}{2} \varepsilon^2 \xi_{\mu\nu}(\mathbf{X}_0) \frac{\partial X_{0\mu}}{\partial q_i} \frac{\partial X_{0\nu}}{\partial q_j} \dot{q}_i \dot{q}_j + \varepsilon \underbrace{\frac{\partial E_0}{\partial X_i} \Big|_{\mathbf{X}_0}}_{=0} \dot{X}_i + \varepsilon^2 \underbrace{\frac{\partial^2 E_0}{\partial X_i \partial X_j} \Big|_{\mathbf{X}_0}}_{\frac{\partial}{\partial q_\mu} \left(\frac{\partial E_0}{\partial X_i} \Big|_{\mathbf{X}_0} \right) = 0} \frac{\partial X_{0j}}{\partial q_\mu} \dot{q}_\mu X_{1i} + \quad (2.26)$$

$$+ \varepsilon^2 \frac{\partial E_1}{\partial X_i} \Big|_{\mathbf{X}_0} \frac{X_{0i}}{\partial q_j} \dot{q}_j + \text{h.o.t.}, \quad (2.27)$$

where the time derivatives are taken with respect to τ . With the variational principle $\frac{\partial R_0}{\partial \dot{q}_i} = 0$, where R_0 is the truncated leading order Rayleighian, we obtain

$$\dot{\mathbf{q}} = -\nabla_\zeta E_1(\mathbf{q}) \quad (2.28)$$

which is valid consistently in leading order and independent of the perturbation \mathbf{X}_1 .

2.3 Onsager's Variational Principle in Soft Matter and Pattern Formation

As explained in the introduction to the present chapter, up to this point we have introduced the concept of the variational principle (2.14) for discrete, finite dimensional systems. However, the variational principle can also be fruitfully employed to formulate and approximate evolution equations for spatially extended systems, which are of great interest in soft matter systems and in the theoretical description of pattern formation in general. Obviously, extended systems exhibit subtleties concerning i.e. boundary conditions, these will be discussed for each system individually whenever they arise.

2.3.1 Particle Diffusion and DDFT

To start with a concrete physical example, following [Doi16, Doi11], we consider a system of colloidal particles with local nondimensional number density $\varrho(\mathbf{x}, t)$ undergoing overdamped Brownian motion subjected to an external potential V_{ext} in a nondimensional Volume $\Omega \subset \mathbb{R}^n, n \in \{1, 2, 3\}$ with boundary $\partial\Omega$. The energy minimized over time in this system for the case of low densities ϱ (and thus negligible particle interactions) is the free energy \mathcal{F}_{id} stemming solely from entropic contributions and the external potential [MT99]:

$$\mathcal{F}_{\text{id}}[\varrho] = \int_{\Omega} k_{\text{B}} T \varrho(\mathbf{x}, t) (\ln(\varrho(\mathbf{x}, t)) - 1) + \varrho(\mathbf{x}, t) V_{\text{ext}}(\mathbf{x}, t) \, \text{d}\mathbf{x}, \quad (2.29)$$

with the Boltzmann constant k_{B} and the temperature T of the system. In order to formulate the equation of motion in the form of the variational principle (2.14), we have to find a convenient “velocity-type” variable. The most straightforward choice would be to consider $\dot{\varrho}$, however, when defining the locally averaged particle velocity $\mathbf{v}(\mathbf{x}, t)$ via

$$\dot{\varrho} = -\nabla \cdot (\varrho \mathbf{v}), \quad (2.30)$$

we obtain a physically intuitive expression for the dissipation function of the system:

$$\mathcal{D} = \frac{1}{2} \int_{\Omega} \xi(\varrho) \mathbf{v}^2 \, d\mathbf{x} , \quad (2.31)$$

where $\xi(\varrho)$ is a per volume friction coefficient dependent on the local density $\varrho(\mathbf{x}, t)$. Note that (2.30) implies mass conservation of the system. By virtue of Green's identity [BSMM12], the rate of change of a general free energy functional \mathcal{F} due to its dependence on ϱ reads:

$$\frac{d}{dt} \mathcal{F} = \int_{\Omega} \frac{\delta \mathcal{F}[\varrho]}{\delta \varrho(\mathbf{x}, t)} \dot{\varrho}(\mathbf{x}, t) \, d\mathbf{x} = - \int_{\Omega} \nabla \cdot (\varrho \mathbf{v}) \frac{\delta \mathcal{F}}{\delta \varrho} \, d\mathbf{x} = \int_{\Omega} \varrho \mathbf{v} \cdot \nabla \frac{\delta \mathcal{F}}{\delta \varrho} \, d\mathbf{x} - \underbrace{\int_{\partial \Omega} \frac{\delta \mathcal{F}}{\delta \varrho} \varrho \mathbf{v} \cdot d\mathbf{S}}_{=0} . \quad (2.32)$$

In (2.32), we assume vanishing particle fluxes $\varrho \mathbf{v}$ on the boundary of our volume Ω . With the Rayleighian $\mathcal{R} = \mathcal{D} + \frac{d}{dt} \mathcal{F}$, we obtain⁴

$$\frac{\delta \mathcal{R}}{\delta \mathbf{v}} = \mathbf{0} \Rightarrow \mathbf{v} = - \frac{\varrho}{\xi} \nabla \frac{\delta \mathcal{F}}{\delta \varrho} \quad (2.33)$$

For $\mathcal{F}[\varrho] = \mathcal{F}_{\text{entr}}[\varrho]$, a vanishing external potential ($V_{\text{ext}} = 0$) and $\xi(\varrho) = \gamma \varrho$, with γ being the friction coefficient of a single particle, we finally end up with the well known diffusion equation:

$$\dot{\varrho} = D \Delta \varrho, \quad \text{with } D = \frac{k_{\text{B}} T}{\gamma} . \quad (2.34)$$

Note that the diffusion constant is defined consistently with the well-known Einstein relation [Ein05], when we consider a colloidal suspension of spherical particles of radius R in a liquid of viscosity η , where $\gamma = 6\pi\eta R$. When retaining the same functional form of the dissipation function but extending the free energy functional \mathcal{F} based on equilibrium density functional theory (DFT) to include particle interaction terms (so-called *excess free energy* contributions),

$$\mathcal{F}[\varrho] = \mathcal{F}_{\text{id}}[\varrho] + \mathcal{F}_{\text{ex}}[\varrho], \quad (2.35)$$

with (2.33), the evolution equation for the density ϱ takes the form of the well established dynamical density functional theory (DDFT) of fluids [MT00, MT99, AE04]:

$$\dot{\varrho}(\mathbf{x}, t) = \nabla \cdot \left(\frac{\varrho(\mathbf{x}, t)}{\gamma} \nabla \frac{\delta \mathcal{F}[\varrho]}{\delta \varrho(\mathbf{x}, t)} \right) . \quad (2.36)$$

If the interaction of the particles is sufficiently local and without external potential, the overall free energy functional $\mathcal{F} = \mathcal{F}_{\text{id}} + \mathcal{F}_{\text{ex}}$ takes the form

$$\mathcal{F} = \int_{\Omega} \frac{\sigma}{2} (\nabla \varrho)^2 + f(\varrho) \, d\mathbf{x} , \quad (2.37)$$

which is well known from Cahn-Hilliard theory of phase separation [CH58, Cah59]. Here, the first summand in the integral corresponds to an interfacial free energy density, whereas the second summand is a local free energy density.

⁴ Here and in the following, we use the shorthand notation $\frac{\delta G[\mathbf{u}]}{\delta \mathbf{u}(\mathbf{x})} := \left(\frac{\delta G[\mathbf{u}]}{\delta u_1(\mathbf{x})}, \dots, \frac{\delta G[\mathbf{u}]}{\delta u_n(\mathbf{x})} \right)^T$ for a functional $G[\mathbf{u}]$ dependent on a n -dimensional vector of continuous variables $\mathbf{u}(\mathbf{x})$.

2.3.2 Conserved and Non-Conserved Order Parameter Equations

The basic model equation in DDFt (2.36) is a special example of an order parameter equation, which exhibits mass conservation.⁵ A more general form of such equations for a set of N scalar order parameter fields $\mathbf{u}(\mathbf{x}, t) \in \mathbb{R}^N$, $\mathbf{x} \in \Omega \subset \mathbb{R}^n$, $n \in \{1, 2, 3\}$ which are locally conserved reads [WTG⁺15]⁶

$$\dot{\mathbf{u}}(\mathbf{x}, t) = \nabla \cdot \left(\mathbf{Q}(\mathbf{u}) \nabla \frac{\delta \mathcal{F}}{\delta \mathbf{u}} \right), \text{ where } \mathbf{Q}(\mathbf{u}) \in \mathbb{R}^{N \times N} \quad (2.38)$$

The matrix \mathbf{Q} is in general a nonlinear function of the order parameters \mathbf{u} but has to be always positive definite and symmetric in order to allow for a formulation of (2.38) in terms of Onsager's variational principle. The free energy functional \mathcal{F} may depend on higher-order derivatives than in the case of (2.37), an example is the Swift-Hohenberg free energy functional which will be discussed in the next section.

While the variational principle (2.33) for the colloidal particle diffusion and DDFt is formulated in terms of the physically intuitive local mean velocity, the natural variables for the formulation of the Rayleighian associated with (2.38) are the fluxes defined via

$$\dot{\mathbf{u}}(\mathbf{x}, t) = -\nabla \cdot \mathbf{J}, \text{ i.e., } \dot{u}_i(\mathbf{x}, t) = -\nabla \cdot (\mathbf{J}_{u_i}), \quad i = 1, \dots, N \quad (2.39)$$

The Rayleighian and variational principle corresponding to (2.38) in terms of these fluxes are given by

$$\mathcal{R} = \mathcal{D} + \frac{d}{dt} \mathcal{F} = \frac{1}{2} \int_{\Omega} \langle \mathbf{J}, \mathbf{Q}^{-1}(\mathbf{u}) \mathbf{J} \rangle \, d\mathbf{x} + \int_{\Omega} \left\langle \nabla \frac{\delta \mathcal{F}}{\delta \mathbf{u}}, \mathbf{J} \right\rangle \, d\mathbf{x}, \quad \frac{\delta \mathcal{R}}{\delta \mathbf{J}} = 0, \quad (2.40)$$

where in this case $\langle \cdot, \cdot \rangle$ denotes the combined (or successive) inner product in the space of order parameters and in the n -dimensional position space.⁷

A less involved non-conserved gradient-type order parameter equation commonly encountered for spatially extended systems reads:

$$\dot{\mathbf{u}}(\mathbf{x}, t) = -\mathbf{Q}(\mathbf{u}) \frac{\delta \mathcal{F}[\mathbf{u}]}{\delta \mathbf{u}(\mathbf{x}, t)}. \quad (2.41)$$

Here, the equivalent variational principle is simply formulated in terms of the variable $\dot{\mathbf{u}}$, given a symmetric and positive definite matrix \mathbf{Q} :

$$\mathcal{R} = \mathcal{D} + \frac{d}{dt} \mathcal{F} = \frac{1}{2} \int_{\Omega} \dot{\mathbf{u}}^T \mathbf{Q}^{-1}(\mathbf{u}) \dot{\mathbf{u}} \, d\mathbf{x} + \int_{\Omega} \frac{\delta \mathcal{F}}{\delta \mathbf{u}} \dot{\mathbf{u}} \, d\mathbf{x}, \quad \frac{\delta \mathcal{R}}{\delta \dot{\mathbf{u}}} = 0. \quad (2.42)$$

For a single order parameter, a constant matrix \mathbf{Q} and a free energy functional \mathcal{F} of the type (2.37), this results in the well known Allen-Cahn equation or real Ginzburg-Landau equation [AC79]. In practice, also a combination of conserved and non-conserved order parameter equations occurs, e.g., in the modeling of evaporative thin liquid films [Thi10].

⁵ For example, in the case of (2.36), $\frac{d}{dt} \left(\int_{\Omega} \varrho(\mathbf{x}, t) \, d\mathbf{x} \right) = 0$, for $\mathbf{v} = 0$ on $\partial\Omega$.

⁶ Here, the divergence and Nabla operators act component-wise, i.e., on each order-parameter component separately. In index notation, (2.38) reads: $\dot{u}_i = \partial_{x_\nu} (Q_{ij} \partial_{x_\nu} \frac{\delta \mathcal{F}}{\delta u_j})$.

⁷ For example, $\langle \nabla \frac{\delta \mathcal{F}}{\delta \mathbf{u}}, \mathbf{J} \rangle = \mathbf{J}_{u_i} \cdot \nabla \frac{\delta \mathcal{F}}{\delta u_i}$.

2.4 Variational Derivation of Amplitude Equations

A well-established coarse graining procedure for pattern forming systems which exhibit the formation of stripes or more involved structures is the derivation of so-called *amplitude equations* which approximate the spatio-temporal evolution of the structures close to the corresponding instability threshold [vHHvS94]. Typically, the derivation involves a multiscale expansion near the threshold which gives successively the leading order solution in terms of harmonic modes and then the spatiotemporal evolution of amplitudes of the latter through the evaluation of *solvability conditions* [Pis06]. Here, we show an alternative derivation of the amplitude equations for both the standard and the conserved *Swift-Hohenberg equation* [SH77, MC00] based on the coarse graining outlined in §2.2. As the solvability conditions amount to projections of the superordinate equations, in the light of §2.2.1 it is not surprising that the resulting equations are equivalent in both approaches.

2.4.1 Swift-Hohenberg Equation

The classical Swift-Hohenberg equation is a prototype equation for pattern formation close to a steady short-scale instability [CH93] which was first derived in [SH77]. In one spatial dimension, it is given by

$$\partial_t u = \varepsilon u - (\partial_x^2 + q_c^2)u - u^3, \quad (2.43)$$

where ε is the bifurcation parameter for the stripe-forming instability and q_c is the wave number of the stripes at onset. In fact (2.43) is of type (2.41) or (2.42), respectively, with $\mathbf{Q}(\mathbf{u}) \equiv 1$ and a free energy functional given by

$$\mathcal{F} = \frac{1}{2} \int \left[(\partial_x^2 + q_c^2) u \right]^2 - \varepsilon u^2 + \frac{1}{2} u^4 \, dx. \quad (2.44)$$

We will now derive reduced amplitude equations for the Swift-Hohenberg equation (2.43) by calculation of reduced functionals \mathcal{D} and \mathcal{F} . Following the scaling presented in [vHHvS94], we perform the following modulated harmonic mode ansatz close to the instability threshold $\varepsilon = 0$ (i.e. $0 < \varepsilon \ll 1$):

$$u_{\text{hm}}(x, X, T) = \varepsilon^{1/2} A(X, T) e^{iq_c x} + c.c., \quad T := \varepsilon t, \quad X := \varepsilon^{1/2} x \quad (2.45)$$

More precisely, we insert (2.45) in the free energy functional (2.44) and obtain:

$$\begin{aligned} \mathcal{F}[u_{\text{hm}}] = & \varepsilon^{-1/2} \frac{1}{2} \int \left[\varepsilon^2 \left(i2q_c \partial_X A(X, T) e^{iq_c x} + c.c. \right)^2 - \varepsilon^2 \left(A(X, T) e^{iq_c x} + c.c. \right)^2 \right] dX \\ & + \varepsilon^{-1/2} \frac{1}{2} \int \varepsilon^2 \frac{1}{2} \left(A(X, T) e^{iq_c x} + c.c. \right)^4 dX + \text{h.o.t.} \end{aligned} \quad (2.46)$$

The free energy functional is now approximated by means of a *slowly varying amplitude approximation* [CG09]. Thereby, we drop all terms of the form

$$\int g(X) e^{\pm i n q_c x} dX \approx 0, \quad \text{where } n \geq 1. \quad (2.47)$$

Thus, the free energy functional $\mathcal{F}[u_{\text{hm}}]$ reduces to

$$\mathcal{F}[u_{\text{hm}}] \approx \varepsilon^{3/2} \frac{1}{2} \int 8q_c^2 (\partial_X A \partial_X A^*) - 2|A|^2 + 3|A|^4 dX. \quad (2.48)$$

In a similar manner, the dissipation functional \mathcal{D} can be approximated when the plane-wave ansatz 2.45 is inserted:

$$\mathcal{D}[u_{\text{hm}}] = \int (\partial_t u_{\text{hm}})^2 dx = \frac{1}{2} \varepsilon^{5/2} \int (\partial_T A(X, T) e^{iq_c x} + c.c.)^2 dX \quad (2.49)$$

$$\approx \varepsilon^{5/2} \int |\partial_T A(X, T)|^2 dX . \quad (2.50)$$

Generally speaking (also with respect to the straightforward generalization to 2 and 3 dimensions), the products of harmonic modes where the wave vectors add up to zero are retained in the slowly varying amplitude approximation shown above. We emphasize that the asymptotic approximation is done with the equations resulting from the variational principle in mind. We are now in the position to derive the dynamical equation for the amplitudes directly from the variational principle. Our reduced variables are henceforth $(A, \partial_T A)$ and $(A^*, \partial_T A^*)$. For both, the variational principle should hold independently. Instead of writing down the variation of the reduced Rayleighian, we directly employ the equivalent form, which is valid consistently in leading order in ε :

$$\frac{\delta \mathcal{D}}{\delta(\partial_T A)} + \varepsilon \frac{\delta \mathcal{F}}{\delta A} = 0 \quad (2.51)$$

$$\frac{\delta \mathcal{D}}{\delta(\partial_T A^*)} + \varepsilon \frac{\delta \mathcal{F}}{\delta A^*} = 0. \quad (2.52)$$

Here, the factor ε in the second summand of (2.51) and (2.52) stems from the introduction of the timescale $T = \varepsilon t$. Finally, we identify (2.52) as the well known amplitude equation for the spatio-temporal evolution of $A(X, T)$ (cf. [vHHvS94]):

$$\partial_T A = 4q_c^2 \partial_{XX} A + A - 3|A|^2 A. \quad (2.53)$$

Note that by performing the approximations shown for the free energy functional \mathcal{F} and for the dissipation integral \mathcal{D} , we can formally approximate the Rayleighian functional \mathcal{R} in one single consistent order in ε , higher order terms would result in higher order contributions to (2.51) and (2.52).

2.4.2 Conserved Swift-Hohenberg Equation

Following [MC00], we consider the mass-conserving equation, which is known as the phase-field crystal (PFC) equation [ELW⁺12] or the conserved Swift-Hohenberg equation [TAR⁺13]:

$$\partial_t u = -\partial_x J = \partial_x^2 \left(\frac{\delta \mathcal{F}}{\delta u} \right) = -\partial_x^2 \left(\varepsilon r u - (q_c^2 + \partial_x^2)^2 u + s u^2 + u^3 \right), \quad (2.54)$$

where ε is a smallness parameter as in the previous section and (r, s) are parameters of order $\mathcal{O}(1)$. The free energy functional \mathcal{F} corresponding to (2.54) is given by

$$\mathcal{F} = \frac{1}{2} \int [(\partial_x^2 + q_c^2) u]^2 - \varepsilon r u^2 + \frac{2s}{3} u^3 + \frac{1}{2} u^4 dx . \quad (2.55)$$

This is the same energy functional as (2.44), except for the cubic contribution parametrized by the factor s and the factor r which has been introduced for better comparability with results from [MC00]. (2.54) can be written in the variational form (2.38) when the corresponding

Rayleighian \mathcal{R} is constructed from the free energy (2.55) and from the following dissipation functional resulting from a mobility $\mathbf{Q} = 1$:

$$\mathcal{D} = \frac{1}{2} \int J^2 dx = \frac{1}{2} \int \left(\int^x \partial_t u(x', t) dx' \right)^2 dx. \quad (2.56)$$

As for the case of the non-conserved Swift-Hohenberg equation (2.43), we perform a multiscale ansatz based on harmonic modes with the critical wave number q_c . In order to account for the mass conservation, the ansatz is now more involved, and reads [MC00]:

$$u_{\text{hmc}}(x, X, T) = \varepsilon^{1/2} A(X, T) e^{iq_c x} + \varepsilon C(X, T) e^{2iq_c x} + c.c. + \varepsilon B(X, T), \quad (2.57)$$

where $A(X, T), C(X, T) \in \mathbb{C}$, $B(X, T) \in \mathbb{R}$.

The large time and length scales are given by $(X, T) = (\varepsilon^{1/2} x, \varepsilon t)$. This ansatz can be inserted in the free energy functional (2.55) which is then truncated at order $\mathcal{O}(\varepsilon^{3/2})$. We furthermore employ again the slowly-varying amplitude approximation (2.47) and therefore only retain contributions, for which the harmonic modes combine to a constant factor. The truncated free energy is given by

$$\begin{aligned} \mathcal{F}[u_{\text{hmc}}] = \varepsilon^{3/2} \int & -r |A|^2 + 4q_c^2 |\partial_X A|^2 + \frac{1}{2} q_c^4 B^2 + 9q_c^4 |C|^2 + \\ & + \frac{3}{2} |A|^4 + 2s |A|^2 B + s(A^2 C^* + A^{*2} C) dX \end{aligned} \quad (2.58)$$

Note that the free energy functional can be written in one single consistent order $\mathcal{O}(\varepsilon^{3/2})$. In order to deduce the dynamics of the order parameters (A, B, C) , we proceed to insert the ansatz (2.57) in the dissipation functional (2.56). The dissipation functional is truncated at order $\mathcal{O}(\varepsilon^{5/2})$:

$$\mathcal{D}[u_{\text{hmc}}] = \frac{\varepsilon^{-1/2}}{2} \int \left[\int^x \left(\varepsilon^{3/2} \partial_T A(X', T) e^{iq_c x'} + \varepsilon^2 \partial_T C(X', T) e^{2iq_c x'} + c.c. \right. \right. \quad (2.59)$$

$$\left. \left. + \varepsilon^2 \partial_T B(X', T) \right) dx' \right]^2 dX \quad (2.60)$$

$$= \frac{\varepsilon^{-1/2}}{2} \int \left[\varepsilon^{3/2} \partial_T A(X, T) \frac{1}{iq_c} e^{iq_c x} + c.c. + \varepsilon^{3/2} \int^X \partial_T B(X', T) dX' \right]^2 dX + \text{h.o.t.} \quad (2.61)$$

$$= \varepsilon^{5/2} \int -\frac{1}{q_c^2} |\partial_T A(X, T)|^2 + \frac{1}{2} \left(\int^X dX' \partial_T B(X', T) \right)^2 dX + \text{h.o.t.} \quad (2.62)$$

In our approximation of the dissipation functional, we used the following iterable identity obtained through integration by parts:

$$\int^x g(X') e^{inq_c x'} dx' = g(X) \frac{1}{inq_c} e^{inq_c x} - \varepsilon^{1/2} \int^x \partial_{X'} g(X') \frac{1}{inq_c} e^{inq_c x'} dx'. \quad (2.63)$$

Note that the truncated dissipation functional does not contain any contributions of the order parameter $C(X, T)$. As before, we can now directly deduce the dynamical equations from the

variational principle. However, since the contributions of $C(X, T)$ to \mathcal{D} are only of order $\mathcal{O}(\varepsilon^3)$, in our approximation

$$\frac{\delta \mathcal{D}}{\delta(\partial_T C)} + \varepsilon \frac{\delta \mathcal{F}}{\delta C} = \frac{\delta \mathcal{D}}{\delta(\partial_T C^*)} + \varepsilon \frac{\delta \mathcal{F}}{\delta C^*} = 0 \quad (2.64)$$

$$\Rightarrow \frac{\delta \mathcal{F}}{\delta C} = \frac{\delta \mathcal{F}}{\delta C^*} = 0. \quad (2.65)$$

From equation (2.65), we obtain

$$9q_c^4 C + sA^2 = 0 \Leftrightarrow C = -\frac{sA^2}{9q_c^4}, \quad (2.66)$$

which we can insert in the truncated free energy functional (2.58) to end up with a reduced free energy functional independent of $C(X, T)$:

$$\mathcal{F}[u_{\text{hmc}}] = \varepsilon^{3/2} \int -r|A|^2 + 4q_c^2 |\partial_X A|^2 + \frac{1}{2}q_c^4 B^2 + 2s|A|^2 B + \frac{1}{2} \left(3 - \frac{2s^2}{9q_c^4} \right) |A|^4 \, dX. \quad (2.67)$$

We can then finally deduce the leading order dynamical equations for $A(X, T)$ and $B(X, T)$ from the variational principle:

$$\frac{\delta \mathcal{D}}{\delta(\partial_T A^*)} + \varepsilon \frac{\delta \mathcal{F}}{\delta A^*} = \frac{\delta \mathcal{D}}{\delta(\partial_T B^*)} + \varepsilon \frac{\delta \mathcal{F}}{\delta B^*} = 0 \quad (2.68)$$

$$\Rightarrow \partial_T A = -q_c^2 \frac{\delta \mathcal{F}}{\delta A^*} = q_c^2 \left(rA + 4q_c^2 \partial_{XX} A - \left(3 - 2\frac{s^2}{9q_c^4} \right) |A|^2 A - 2sAB \right) \quad (2.69)$$

$$\partial_T B = \partial_{XX} \frac{\delta \mathcal{F}}{\delta B} = \partial_{XX} \left(q_c^4 B + 2s|A|^2 \right). \quad (2.70)$$

These equations are in agreement with the corresponding results obtained in [MC00].

2.5 Conclusion

In the present chapter, we have introduced Onsager's variational principle, as recently discussed by M. Doi et al. and K. Glasner et al.. One main focus of the presentation has been the use of the variational principle for the derivation of coarse-grained equations. Here, as it has been previously done in [Gla05], we have shown that the coarse graining by a variational principle restricted to a lower dimensional parameter set of parametrized ansatz functions is equivalent to a projection procedure. This equivalence will also be shown explicitly in §6.2.3 for a model system in the context of hydrodynamics. For now, we have illustrated the aforementioned equivalence by the derivation of amplitude equations for both the standard and the conserved Swift-Hohenberg equation, leading to the same results as those obtained by a projection method (cf. [vHHvS94, MC00]).

Given this equivalence, it is of course an interesting question whether the variational principle has specific advantages over the commonly used methods for the case where one deals with equations which can be written in terms of Onsager's variational principle. One obvious advantage is that the structure of the underlying equation remains clear: One explicitly

calculates approximate energy and dissipation functions (or functionals) and obtains the coarse-grained equations as a variational principle. As compared to common projection techniques this might even offer the opportunity to approximate the dissipation and the energy by different ansatz functions parametrized by the same parameters, based on different standards concerning the quality of the approximations.

The second advantage of the variational procedure is that given one is in the position to calculate the coarse-grained Rayleighian, the derivation is more compact than an equivalent derivation by projection. However it is not always straightforward to write down the coarse-grained Rayleighian as a function of the coarse-grained variables only. Finally, we have to emphasize that the coarse graining by the variational principle as presented in the present chapter requires the a priori choice of adequate ansatz functions and is not an adequate means for an order by order asymptotic approximation of the initial equations.

3 The Thin-Film Equation

In this chapter, we discuss the formulation of model equations for viscous liquid films on substrates in terms of variational principles. In the first part, we introduce the Stokes equations and boundary conditions for the solid-liquid and the liquid-gas interface through the variation of a corresponding Rayleighian (cf. [QWS06, XQ17]). In the second part of the chapter, we reduce the system of equations and demonstrate that asymptotically, for a *long-wave* or *thin-film geometry*, the full hydrodynamic Rayleighian can be reduced to a Cahn-Hilliard-type Rayleighian. Then, the latter is a functional of the local film height (and corresponding fluxes). The resulting reduced equation is the well known *thin-film equation*.¹ Finally, we introduce variants and generalizations of the thin-film equation which are employed in this thesis.

3.1 Stokes Flow of a Viscous Liquid on a Solid Substrate

3.1.1 Stokes Equations from a Variational Principle

The rate of dissipation of energy in an incompressible viscous liquid with dynamic viscosity η is given by [LL91]:

$$\frac{d}{dt}E = -\frac{\eta}{2} \int d\mathbf{x} \left(\frac{\partial u_i}{\partial x_j} + \frac{\partial u_j}{\partial x_i} \right)^2. \quad (3.1)$$

In the over-damped limit, the constituting equations for the flow of the liquid can be written in terms of an Onsager type variational principle [Doi13, QWS06]. The corresponding Rayleighian $\mathcal{R}_{\text{Stokes}}$ consists solely of a Rayleigh dissipation function $\mathcal{D} = -\frac{1}{2} \frac{d}{dt}E$ and a constraint term imposing the condition

$$\frac{\partial u_i}{\partial x_i} = 0 \quad (3.2)$$

for the incompressibility of the liquid through a local (space-dependent) Lagrangian multiplier $p(\mathbf{x})$:

$$\mathcal{R}_{\text{Stokes}} = \frac{\eta}{4} \int d\mathbf{x} \left(\frac{\partial u_i}{\partial x_j} + \frac{\partial u_j}{\partial x_i} \right)^2 - \int d\mathbf{x} p(\mathbf{x}) \frac{\partial u_i}{\partial x_i}. \quad (3.3)$$

The variation of $\mathcal{R}_{\text{Stokes}}$ with respect to the components of the velocity field and to the Lagrangian multiplier reads:

$$\delta \mathcal{R}_{\text{Stokes}} = - \int d\mathbf{x} \eta \frac{\partial}{\partial x_j} \left(\frac{\partial u_j}{\partial x_i} + \frac{\partial u_i}{\partial x_j} \right) \delta u_i + \int d\mathbf{x} \frac{\partial p}{\partial x_i} \delta u_i - \int d\mathbf{x} \frac{\partial u_i}{\partial x_i} \delta p \stackrel{!}{=} 0, \quad (3.4)$$

¹ For similar derivations of the thin-film equation based on Onsager's variational principle, cf., e.g., [XTQ15, XDD16].

where Green's theorem, neglecting boundary terms, and the symmetry of the energy dissipation functional was used. The variation with respect to each component of the velocity field and to the Lagrangian multiplier must vanish independently, which results in the well-known Stokes equations for incompressible fluids:

$$\eta \nabla^2 \mathbf{u} = \nabla p, \quad \nabla \cdot \mathbf{u} = 0. \quad (3.5)$$

The Lagrangian multiplier p is identified as the pressure field in the liquid.

3.1.2 Viscous Liquid with a Liquid-Gas Interface on a Solid Substrate

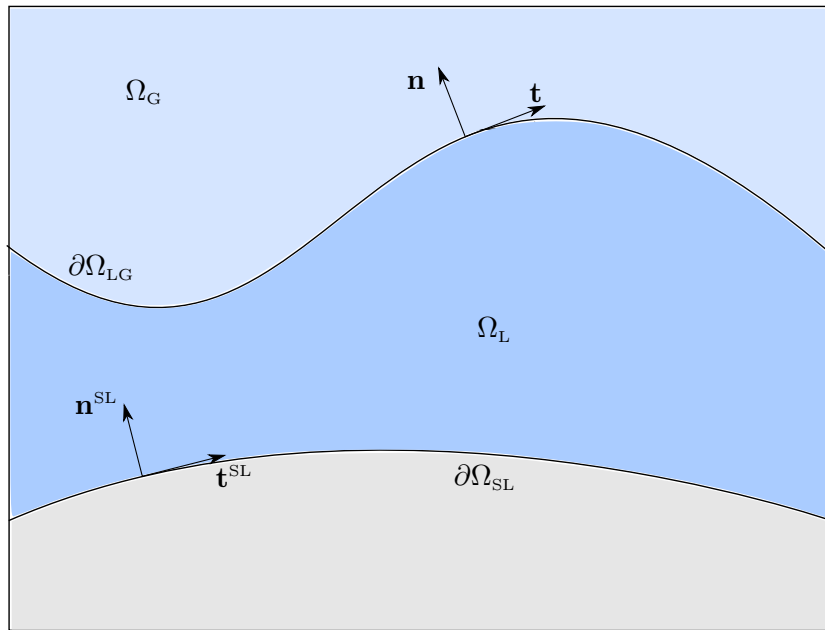


Figure 3.1: Sketch of a two-phase flow on a curved solid substrate with definitions of the normal and tangential vectors as well as the different volumes and interfaces necessary for the formulation of the governing equations.

In the previous subsection, we have discussed how the Stokes equations can be written in terms of a variational principle. Next, we consider a two-phase fluid (i.e., liquid and gaseous phase) on a solid substrate. It is assumed that the flow in both phases is given by the Stokes equation, the two phases are immiscible and the velocity field is continuous at the interface of the two fluids. A sketch of the considered geometry with respective definitions is shown in FIG. 3.1. Note that the solid-liquid interface is not necessarily flat. While the solid-liquid interface is assumed to be static, the liquid-gas interface may move. In order to relate the interface motion to the flow field, we formulate the so-called *kinematic boundary condition*, which essentially defines the interface. Given the velocity \mathbf{v}_{LG} of the liquid-gas interface, the kinematic boundary condition states

$$(\mathbf{u} - \mathbf{v}_{LG}) \cdot \mathbf{n} = 0 \quad \text{on } \partial\Omega_{LG}, \quad (3.6)$$

with \mathbf{n} denoting the normal vector on the liquid-gas interface $\partial\Omega_{\text{LG}}$. The no-penetration boundary condition

$$\mathbf{u} \cdot \mathbf{n}^{\text{SL}} = 0 \quad \text{on } \partial\Omega_{\text{SL}} \quad (3.7)$$

at the solid-liquid interface can be seen as a special case of a kinematic boundary condition for an immobile boundary. In (3.7), \mathbf{n}^{SL} is normal to the solid-liquid interface $\partial\Omega_{\text{SL}}$.

We now formulate a Rayleighian, such that the variational principle of the latter gives the full remaining set of bulk and interface² equations describing the system in the overdamped limit. The Rayleighian consists of the following contributions:

1. Viscous energy dissipation in the liquid and the gaseous phase³:

$$\mathcal{R}_{\text{diss}} = \frac{\eta_{\text{L}}}{4} \int_{\Omega_{\text{L}}} d\mathbf{x} \left(\frac{\partial u_i}{\partial x_j} + \frac{\partial u_j}{\partial x_i} \right)^2 + \frac{\eta_{\text{G}}}{4} \int_{\Omega_{\text{G}}} d\mathbf{x} \left(\frac{\partial u_i}{\partial x_j} + \frac{\partial u_j}{\partial x_i} \right)^2. \quad (3.8)$$

2. Constraint terms enforcing the incompressibility condition in both phases:

$$\mathcal{R}_{\text{constr.}} = - \int_{\Omega_{\text{L}}} d\mathbf{x} p_{\text{L}}(\mathbf{x}) \frac{\partial u_i}{\partial x_i} - \int_{\Omega_{\text{G}}} d\mathbf{x} p_{\text{G}}(\mathbf{x}) \frac{\partial u_i}{\partial x_i}. \quad (3.9)$$

3. Rate of change of energy associated with the liquid-gas interface $\partial\Omega_{\text{LG}}$ (cf. [Tom00]):

$$\mathcal{R}_{\text{LG}} = - \int_{\partial\Omega_{\text{LG}}} dS \sigma u_i n_i \frac{\partial n_j}{\partial x_j}, \quad (3.10)$$

where σ is the interfacial tension of the liquid-gas interface.

4. Dissipation due to slipping of the liquid at the solid-liquid interface (see [QWS06] for details):

$$\mathcal{R}_{\text{slip}} = \int_{\partial\Omega_{\text{SL}}} dS \frac{\eta_{\text{L}}}{2l_s} (\mathbf{t}_i^{\text{SL}} u_i)^2, \quad (3.11)$$

where \mathbf{t} is a normalized vector tangential to $\partial\Omega_{\text{SL}}$.

We proceed by performing the variation of the full Rayleighian

$$\mathcal{R}_{\text{SLG}} = \mathcal{R}_{\text{diss}} + \mathcal{R}_{\text{constr.}} + \mathcal{R}_{\text{LG}} + \mathcal{R}_{\text{slip}} \quad (3.12)$$

²The equations on the interfaces are also referred to as boundary conditions.

³Here and in the following, the indices L and G are used to denote the liquid and gaseous phase, respectively. In principle, two different velocity fields \mathbf{u}^{G} , \mathbf{u}^{L} have to be introduced, however we omit the indices for these fields, since it is always specified by the domains which velocity is meant. On the interfaces both fields are equal by virtue of the continuity condition.

with respect to the flow field \mathbf{u} in Ω_L , Ω_G as well as on $\partial\Omega_{SL}$, $\partial\Omega_{LG}$ and with respect to the pressure fields p_G , p_L . Unlike for the case of the bulk Stokes equations in §3.1.1, boundary terms arising when Green's theorem is employed are not neglected⁴:

$$\begin{aligned} \delta\mathcal{R}_{\text{diss}} + \delta\mathcal{R}_{\text{constr.}} &= \sum_{k \in \{L, G\}} \left(-\eta_k \int_{\Omega_k} \nabla^2 u_i \delta u_i + \frac{\partial p_k}{\partial x_i} \delta u_i - \delta p_k \frac{\partial u_i}{\partial x_i} \right) \\ &+ \int_{\partial\Omega_{LG}} dS \eta_L n_j \left(\frac{\partial u_i}{\partial x_j} + \frac{\partial u_j}{\partial x_i} \right) \delta u_i - \int_{\partial\Omega_{LG}} dS \eta_G n_j \left(\frac{\partial u_i}{\partial x_j} + \frac{\partial u_j}{\partial x_i} \right) \delta u_i \\ &- \int_{\partial\Omega_{LG}} dS p_L n_i \delta u_i + \int_{\partial\Omega_{LG}} dS p_G n_i \delta u_i + \int_{\partial\Omega_{SL}} dS \eta_L n_j^{\text{SL}} \left(\frac{\partial u_i}{\partial x_j} + \frac{\partial u_j}{\partial x_i} \right) \delta u_i, \end{aligned} \quad (3.13)$$

$$\delta\mathcal{R}_{LG} + \delta\mathcal{R}_{\text{slip}} = - \int_{\partial\Omega_{LG}} dS \sigma \frac{\partial n_j}{\partial x_j} n_i \delta u_i + \int_{\partial\Omega_{SL}} dS \frac{\eta_L}{l_s} t_j^{\text{SL}} u_j t_i^{\text{SL}} \delta u_i, \quad (3.14)$$

Requiring all the variations with respect to the components of the velocity field and the pressure to vanish independently in the bulk domains and on the interfaces results in the following set of equations:

1. *Incompressible Stokes equations* in the bulk for both the gaseous and the liquid phase:

$$\eta_{L,G} \nabla^2 \mathbf{u} = \nabla p_{L,G}, \quad \nabla \cdot \mathbf{u} = 0 \quad \text{in } \Omega_{G,L}. \quad (3.15)$$

2. *Stress-free boundary conditions* at the liquid-gas interface (including surface tension effects):

$$\boldsymbol{\tau}_L \cdot \mathbf{n} - \boldsymbol{\tau}_G \cdot \mathbf{n} = (\sigma \nabla \cdot \mathbf{n}) \mathbf{n} \quad \text{on } \partial\Omega_{LG}. \quad (3.16)$$

3. *Navier Slip boundary condition* at the solid-liquid interface [QWS06]:

$$\frac{\eta_L}{l_s} \mathbf{t}^{\text{SL}} \cdot \mathbf{u} = -\eta_L (\mathbf{t}^{\text{SL}} \cdot \nabla (\mathbf{n}^{\text{SL}} \cdot \mathbf{u}) + \mathbf{n}^{\text{SL}} \cdot \nabla (\mathbf{t}^{\text{SL}} \cdot \mathbf{u})), \quad \text{on } \partial\Omega_{SL}. \quad (3.17)$$

In (3.16), the stress tensors [LL91] in the liquid and the gaseous phase were introduced:

$$(\boldsymbol{\tau}_{G,L})_{ij} := -p_{G,L} \delta_{ij} + \eta_{G,L} \left(\frac{\partial u_i}{\partial x_j} + \frac{\partial u_j}{\partial x_i} \right). \quad (3.18)$$

The boundary condition (3.17) is obtained through a projection of the corresponding boundary terms onto the tangential direction \mathbf{t}^{SL} . The set of equations (3.15)-(3.17) which is entirely encoded in the Rayleighian (3.12) form together with (3.6), (3.7) and the continuity condition on $\partial\Omega_{LG}$ the full set of equations necessary to describe the two-phase viscous Stokes flow on a solid substrate [ODB97, Köp11].

⁴ The boundary terms from the variation of (3.9) at the solid-liquid interface vanish by virtue of (3.7)

3.2 Long-Wave Reduction and the Thin-Film Equation

3.2.1 Monge Parametrization of the Liquid-Gas Interface

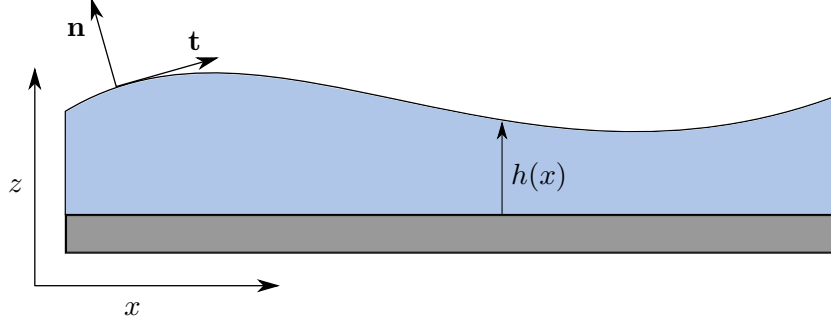


Figure 3.2: Sketch of a liquid film on a flat solid substrate in two dimensions. The free liquid-gas interface is fully described by a height function $h(x)$.

We now focus on a particular geometry for the problem discussed in the previous section, where the solid liquid interface is flat and the solid-gas interface can be described by a height function $h(x)$ (cf. FIG. 3.2). In the following, the system is considered in 2D, the generalization to 3D is straightforward. The unit vectors \mathbf{n} , \mathbf{t} normal and tangential to the liquid-gas interface can be expressed through the height function $h(x)$, where $x \in [0, L]$ as

$$\mathbf{n} = \frac{1}{\sqrt{1 + (\partial_x h)^2}} (-\partial_x h, 1)^T, \quad \mathbf{t} = \frac{1}{\sqrt{1 + (\partial_x h)^2}} (1, \partial_x h)^T. \quad (3.19)$$

The normal velocity of the interface $v_n = \mathbf{v}_{\text{LG}} \cdot \mathbf{n}$ is given by [XTQ15]

$$v_n = \frac{1}{\sqrt{1 + (\partial_x h)^2}} \partial_t h \quad (3.20)$$

and the kinematic boundary condition can be expressed as

$$\partial_t h = u_z - u_x \partial_x h. \quad (3.21)$$

Furthermore, we now assume that both pressure and viscous dissipation can be neglected in the gaseous phase. The Rayleighian (3.12) reduces to

$$\begin{aligned} \mathcal{R}_{\text{SLG}} = & \frac{1}{4} \int_0^L dx \int_0^{h(x)} dz \eta_L \left(\frac{\partial u_i}{\partial x_j} + \frac{\partial u_j}{\partial x_i} \right)^2 + \int_0^L dx \sigma (-\nabla \cdot \mathbf{n}) (u_z - \partial_x h u_x) \Big|_{z=h} \\ & - \int_0^L dx \int_0^{h(x)} dz p_L \nabla \cdot \mathbf{u} + \int_0^L dx \frac{\eta_L}{2l_s} u_x^2 \Big|_{z=0}. \end{aligned} \quad (3.22)$$

3.2.2 Long-Wave Approximation

The equations resulting from the variation of the Rayleighian (3.22) can be further reduced by employing the so-called *long-wave* or *lubrication approximation* [ODB97]. Here, a nondimensionalization is performed and assuming that typical lengthscales in direction longitudinal (here x -direction) are much larger than typical lengthscales orthogonal to the substrate (z -direction) a smallness parameter ε is introduced. The employed scaling is given by (cf. [Köp11, ODB97]):

$$\begin{aligned} \varepsilon &= \frac{h_0}{l_0}, \quad z = h_0 \tilde{z}, \quad x = l_0 \tilde{x} = \frac{h_0}{\varepsilon} \tilde{x}, \quad h = h_0 \tilde{h}, \quad L = l_0 \tilde{L}, \quad u_z = \frac{h_0}{t_0} \tilde{u}_z, \\ u_x &= \frac{l_0}{t_0} \tilde{u}_x = \frac{h_0}{\varepsilon t_0} \tilde{u}_x, \quad p = \frac{\eta_L}{t_0 \varepsilon^2} \tilde{p}, \quad l_s = h_0 \tilde{l}_s, \quad \mathcal{R}_{\text{SLG}} = \frac{\eta_L h_0^2}{t_0^2 \varepsilon^3} \tilde{\mathcal{R}}_{\text{SLG}}, \quad \text{Ca} = \varepsilon^{-3} \frac{l_0 \eta_L}{t_0 \sigma}. \end{aligned} \quad (3.23)$$

The non-dimensionalized Rayleighian (3.22) is truncated at leading order in the smallness parameter ε and reads after dropping the tildes:

$$\begin{aligned} \mathcal{R}_{\text{LW}} &= \frac{1}{2} \int_0^L dx \int_0^{h(x)} dz \left(\frac{\partial u_x}{\partial z} \right)^2 - \int_0^L dx \text{Ca}^{-1} (u_z - \partial_x h u_x) \partial_{xx} h \Big|_{z=h} \\ &\quad - \int_0^L dx \int_0^{h(x)} dz p_L \nabla \cdot \mathbf{u} + \int_0^L dx \frac{u_x^2}{2l_s} \Big|_{z=0} \end{aligned} \quad (3.24)$$

Note that no velocity variable (neither in the bulk nor on the interfaces) was eliminated completely. The variational principle applied to (3.25) gives the following set of equations [ODB97]:

$$\frac{\partial^2 u_x}{\partial z^2} = \frac{\partial p_L}{\partial x}, \quad \frac{\partial p_L}{\partial z} = 0, \quad \frac{\partial u_x}{\partial z} = 0 \Big|_{z=h}, \quad p_L = -\text{Ca}^{-1} \partial_{xx} h \Big|_{z=h}, \quad \frac{\partial u_x}{\partial z} = \frac{u_x}{l_s} \Big|_{z=0}, \quad \nabla \cdot \mathbf{u} = 0. \quad (3.25)$$

These equations can be integrated⁵ by taking advantage of (3.7) which results in the following velocity:

$$u_x(z) = \partial_x \left(-\text{Ca}^{-1} \partial_{xx} h \right) \left(\frac{z^2}{2} - hz - l_s h \right). \quad (3.26)$$

From the incompressibility condition and the kinematic boundary condition (3.21), we obtain

$$\partial_t h = -\partial_x J_x, \quad \text{where} \quad (3.27)$$

$$J_x := \int_0^h dz u_x \quad (3.28)$$

which describes in combination with the result (3.26) the motion of the interface as a PDE for the local height h . However, by inserting (3.26) into (3.25), the inherited variational structure

⁵ Cf. [ODB97] for details.

of the equation of motion for the interface can be highlighted directly: By straightforward integration, it is seen that

$$\frac{1}{2} \int_0^L dx \int_0^{h(x)} dz \left(\frac{\partial u_x}{\partial z} \right)^2 + \int_0^L dx \frac{u_x^2}{2l_s} \Big|_{z=0} = \frac{1}{2} \left(\partial_x \left(-\text{Ca}^{-1} \partial_{xx} h \right) \right)^2 \left(\frac{h^3}{3} + l_s h^2 \right) \quad (3.29)$$

$$= \frac{1}{2} \int_0^L dx J_x^2 \left(\frac{h^3}{3} + l_s h^2 \right)^{-1}. \quad (3.30)$$

Thus, the Rayleighian (3.25) can be rewritten in the form

$$\mathcal{R}_{\text{LW}} = \frac{1}{2} \int_0^L dx J_x^2 \left(\frac{h^3}{3} + l_s h^2 \right)^{-1} + \int_0^L dx \partial_x J_x \text{Ca}^{-1} \partial_{xx} h, \quad (3.31)$$

where we make use of the identity $\partial_x J_x = -u_z(x, z=h) + \partial_x h u_x$, which follows directly from the incompressibility condition. Finally, when defining the mobility function $M(h)$ and the interfacial energy functional $\mathcal{F}[h]$ according to

$$M(h) := \frac{h^3}{3} + l_s h^2, \quad \mathcal{F}[h] = \mathcal{F}_{\text{cap}}[h] := \int_0^L dx \frac{\text{Ca}^{-1}}{2} (\partial_x h)^2, \quad (3.32)$$

it is seen that the evolution equation for the film height as given by the variational principle formulated in terms of the flux J_x in combination with (3.27) belongs to the previously discussed class of conserved order parameter equations (2.38):

$$\mathcal{R}_{\text{LW}} = \frac{1}{2} \int_0^L dx \frac{J_x^2}{M(h)} - \int_0^L dx \partial_x J_x \frac{\delta \mathcal{F}}{\delta h}, \quad \frac{\delta \mathcal{R}_{\text{LW}}}{\delta J_x} = 0, \quad \partial_t h = -\partial_x J_x. \quad (3.33)$$

The resulting *thin-film equation* for the local film height is readily generalized to two dimensional substrates and then reads

$$\partial_t h = \nabla \cdot \left(M(h) \nabla \frac{\delta \mathcal{F}}{\delta h} \right). \quad (3.34)$$

The gradient dynamics structure of (3.34) is, as already emphasized, directly inherited from the variational principle underlying the Stokes equation with its boundary conditions.

3.2.3 Generalizations of the Thin-Film Equation

In the previous subsection, the thin-film equation (3.34) has been derived from a long-wave approximation of Stokes flow on a substrate including surface tension of the liquid-gas interface only. We did neither consider other energetic contributions nor the presence of a three phase contact line (liquid-solid-gas). A three phase contact line corresponds to a region where $h \rightarrow 0$. One observes that if the flux at the contact line is non-vanishing, i.e., whenever the contact line is moving, the dissipation integral in the Rayleighian (3.33) diverges in the case of a no-slip model ($l_s = 0$). This corresponds to the well known *moving contact line singularity*, which was first pointed out in [HS71].

As an alternative to the inclusion of slip, a well-established approach to eliminate the contact line singularity is the inclusion of energetic contributions stemming from the interaction of the liquid with the solid as well as from the interaction of the solid-liquid and the liquid-gas interface. This interaction energy $f(h)$ depends on the local height of the liquid film and is termed *binding-, wetting- or disjoining potential*. Its concept will be discussed in more detail in §4.4. The thin-film equation is augmented through the inclusion of a wetting potential in the energy functional \mathcal{F} :

$$\mathcal{F}[h] = \int_{\Omega} dx \frac{1}{2} (\nabla h)^2 + f(h) \quad (3.35)$$

$$\Rightarrow \partial_t h = \nabla \cdot \left(M(h) \nabla \left(-\nabla^2 h + f'(h) \right) \right). \quad (3.36)$$

In the context of a regularization of the moving contact line singularity, the wetting potential can be chosen such that it exhibits a stable minimum at a small film height (typically in the range of a few nanometers) which is then a lower bound to the film height everywhere in the system if additionally $f(h) \rightarrow \infty$ for $h \rightarrow 0$. In other words, regions which are considered as non-wetted macroscopically are in this modeling approach covered by an ultrathin *adsorption layer* (or *precursor film*). As thus, mathematically, h never vanishes, no singularity arises at the henceforth apparent contact line. A common expression for a non-dimensional wetting potential which gives rise to an adsorption layer reads [Pis01]:

$$f(h) = -\frac{1}{2h^2} + \frac{1}{5h^5}. \quad (3.37)$$

Note that the non-dimensional form of 3.37 implies a particular choice of the time and length-scales (for details, cf. [Köp11]). This wetting potential will be employed throughout this thesis. A further generalization of the thin-film equation is obtained by including gravitational effects. The thin-film equation for a liquid on a plate oriented in x -direction which is inclined by an angle ⁶ α with respect to the plane perpendicular to the gravitational force of magnitude g (cf. FIG. 3.3 a)) is given by

$$\partial_t h(\mathbf{r}, t) = \nabla \cdot \left[M(h) \nabla \left(-\nabla^2 h + f'(h) \right) + \chi(h) \right], \quad (3.38)$$

$$\text{where } \chi(h) = g \frac{h^3}{3} (\nabla h + \boldsymbol{\alpha}), \quad \boldsymbol{\alpha} = (\alpha, 0)^T, \quad M(h) = \frac{h^3}{3}. \quad (3.39)$$

This equation was derived in [PP00] in combination with a specific binding potential and subsequently employed in, e.g., [TNB⁺02, TVN⁺01b] for the modeling of sliding liquid drops on inclined substrates. Model equations of type (3.38) supplemented by boundary conditions modeling a *dip-coating* geometry are also discussed in [WZC⁺16, TGT14, GTLT14] and will be employed in Chap. 5. As discussed in [EWGT16], (3.38) can be formally written in the gradient dynamics form (3.34). However, in this case, the functional \mathcal{F} reads:

$$\mathcal{F}[h] = \mathcal{F}_{\text{incl}}[h] = \int_{\Omega} \frac{1}{2} (\nabla h)^2 + f(h) + \frac{1}{2} gh^2 + gh\alpha x \, dx \quad (3.40)$$

where, in contrast to the previously discussed functionals, the integrand in $\mathcal{F}_{\text{incl}}$ depends explicitly on the space variable x . Finally, in the derivation of the thin-film equation in §3.2.2,

⁶ The angle α corresponds to the rescaled system, whereas the physical inclination is $\tilde{\alpha} = \varepsilon\alpha$

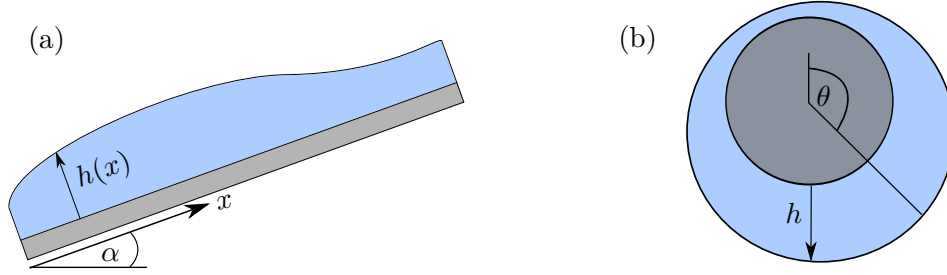


Figure 3.3: (a) Sketch of a liquid film on a flat solid substrate which is inclined w.r.t. the plane orthogonal to gravity by an angle α . (b) Sketch of a cylinder coated by a liquid. The surface of the cylinder is parametrized by the angle θ .

we only considered a flat substrate. For the flow of viscous liquid films on a cylindrical surface, a long wave approximation can be performed for film heights that are small in comparison to the radius R of the cylinder and the following scaled equation is obtained (for the 1D case):

$$\partial_t h = \partial_\theta \left(h^3 \partial_\theta \left[-\partial_{\theta\theta} h - h + \text{Bo} \cos(\theta) + f'(h) \right] \right). \quad (3.41)$$

In (3.41), the local height h is a function of the angle θ (cf. FIG. 3.3 b)). The effect of gravitation is also included and parametrized by the so called *Bond number* $\text{Bo} = (R^3 \rho g) / (h_0 \sigma)$, which quantizes the ratio of the influences of gravity and surface tension. Here, ρ is the density of the liquid, σ its surface tension and h_0 is a typical height scale (for details concerning the scaling employed in (3.41), cf. [Thi11]). The energy functional corresponding to (3.41) reads:

$$\mathcal{F}_{\text{Cyl}}[h] = \int_0^{2\pi} \frac{1}{2} \left[(\partial_\theta h)^2 - h^2 \right] + f(h) + \text{Bo} \cos(\theta) h \, d\theta. \quad (3.42)$$

The general lubrication approximation for liquids on cylindrical substrates is introduced in [Mof77, Puk77]. In the present form, i.e., with the inclusion of a binding potential f , (3.41) was first introduced in [Thi11]. The non-flat geometry is accounted for in the long-wave approximation through the quadratic second summand in (3.42). Recently, in [vTH18], a new long-wave theory for liquids on a cylinder has been derived in the framework of Onsager's variational principle by inclusion of higher order curvature corrections in the energy functional. In Chap. 6, we will employ (3.41) with an additional advection term for the description of a droplet of partially wetting liquid on a rotating cylinder.

4 Instabilities of Liquid Ridges on Heterogeneous Substrates - Thin-Film Modeling and Comparison to KMC

4.1 Introduction and Experiments

The *Plateau-Rayleigh* instability, which is a transversal instability of elongated (liquid) structures leading to the formation of droplets, is a well known phenomenon in fluid dynamics [dGBWQ04] occurring for, e.g., liquid jets, filaments, and similar systems.

In recent experiments, a Plateau-Rayleigh type instability turned out to be important for structured depositions of organic molecules on prepatterned substrates [WDW⁺11, WC12]. The goal of the experiments was to coat gold-stripe-prepatterned regions of the substrate in a regular manner. More specifically, in [WDW⁺11], the authors consider the deposition of DtCDQA (an organic molecule relevant for light emission applications such as OLEDs) on SiO₂ substrates partially covered with Au lines of varying width. At an average coverage height of the entire substrate of 50 nm, they observe three different morphological structures on the stripe-prepatterned substrate: As a desirable morphology from a application-oriented point of view, regular molecule ridges on top of Au prepattern can be found. However, droplets of DtCDQA on the bare SiO₂ are also observed. Finally, for large amounts of molecules on a single prepattern stripe, bulges are formed, corresponding to droplets which are situated mainly on the bare substrate and are distorted by the underlying prepattern stripe (cf. FIG. 4.1). The authors of [WDW⁺11] infer the shape of the droplets and ridge cross sections from AFM measurement of height and width of the respective structures and come to the conclusion that the structures are of spherical cap type. Furthermore, in [WDW⁺11], W. Wang et al. conclude from the shape of the structures that the molecules behave liquid-like on the substrate. The contact angles are measured by AFM and values between 10° and approximately 20° are obtained.

Given the assumptions of the liquid-like behavior and the small contact angles, a modeling of the dynamics of the structures on the prepatterned substrate by a thin-film equation is reasonable.¹ In the following, we present results from the modeling by a thin-film equation and discuss the comparison with, and the mapping of simulations obtained from a particle-based kinetic Monte Carlo algorithm.

¹ Cf. [HLH⁺15, Hon13] for previous work on thin-film modeling of ridge instabilities motivated by the experiments in [WDW⁺11, WC12]. The focus in [HLH⁺15, Hon13] is on the instability of a ridge on a single prepattern stripe and different transport mechanisms during the instability. The thin-film model employed in the mentioned literature is very similar to the one investigated in the present chapter.

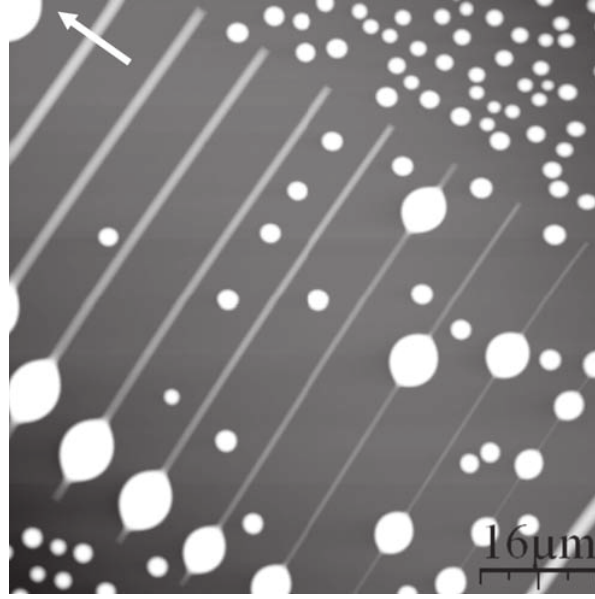


Figure 4.1: AFM picture of structures formed on prepatterned substrate with varying width of the Au-strips on the SiO_2 substrate. One observes droplets on the bare substrate, as well as bulges on the prepattern stripes. The wavelength of the bulges increases with increasing width of the prepattern stripes. Picture reproduced with permission from [WDW⁺11], © WILEY-VCH Verlag GmbH & Co. KGaA.

4.2 Thin-Film Modeling

4.2.1 Model Binding Potential

In order to model a substrate which is chemically patterned, we introduce a binding potential which is spatially modulated and has the general form [TBH⁺17, MRD08, HLH⁺15]

$$f_{\text{pre}}(h, \mathbf{x}) = f_{\text{hom}}(h) \cdot [1 + \rho g(\mathbf{x})], \quad (4.1)$$

where the parameter ρ fixes the strength of the prepattern and f_{hom} is given by (3.37). For two locations $\mathbf{x}_{1,2}$ on the substrate, $g(\mathbf{x}_1) < g(\mathbf{x}_2)$ implies that according to the model binding potential, at \mathbf{x}_1 , the substrate is locally *more* wettable than at \mathbf{x}_2 .² Motivated by the experimental setup in [WDW⁺11, WC12], we focus on prepattern geometries which are translationally invariant in one spatial dimension (stripe geometry). In particular, the general form of the modulation function g employed in the following reads:

$$g(\mathbf{x}) = g(x) = \frac{1}{2} \sum_{j=1}^{2n} (-1)^j \tanh\left(\frac{x - x_j}{l_s}\right), \quad (4.2)$$

where the steepness of the transitions between more and less wettable domains occurring at the positions $\{x_j\}$ is given by the parameter l_s which we fix to $l_s = 3.0$ in the present chapter. A plot of the modulation function g for the exemplary case of two prepattern stripes is shown in

² the relation of the binding potential to the apparent equilibrium contact angle is discussed in §4.2.3

FIG. 4.2. The model equations employed for the thin-film modeling in the present chapter are then given by (3.36) with the binding potential (4.1):

$$\partial_t h = \nabla \cdot \left(M(h) \nabla \left(-\nabla^2 h + f'_{\text{pre}}(h, x) \right) \right) \quad \text{with} \quad M(h) := \frac{h^3}{3}. \quad (4.3)$$

Note that we choose the mobility function $M(h)$ as obtained for the no-slip case (cf. §3.2.2).

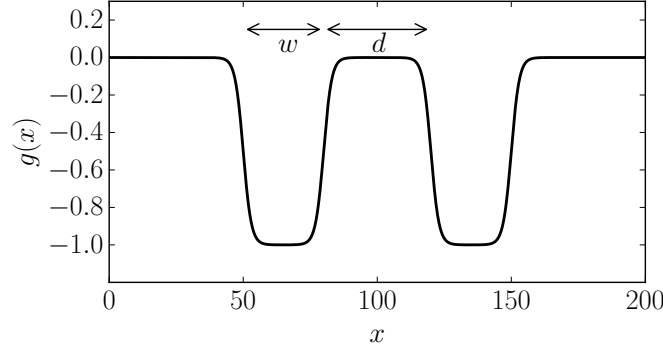


Figure 4.2: Plot of the modulation function g given by (4.2) for the case of two stripes with individual width w and distance d from each other.

4.2.2 Numerical Methods

We shortly outline the numerical methods employed for thin-film type equations in the present and the subsequent chapters. In order to investigate the nonlinear PDE model equations, we conduct *numerical time simulations* (NTS) and, for the calculation of steady states, *numerical path continuation*.

The NTS are performed building on the generic finite element framework DUNE PDELab [BHM10, BBD⁺08b, BBD⁺08a], employing bilinear ansatz functions on a rectangular grid. For the time-stepping, we use an implicit second order Runge-Kutta algorithm [Ale77]. In order to implement the equations in question in the finite element framework employing bilinear ansatz functions, they have to be written in a *weak formulation* such that no derivative of second order or higher appears for the fields and test functions. In order to achieve this, we have to introduce a splitting of the thin-film type equations. For example, for the thin-film equation (3.36) on a domain Ω , the following splitting is employed (cf. [Wil16]):

$$\partial_t h = -\nabla \cdot (M(h) \nabla w); \quad w = \nabla^2 h - f'(h), \quad (4.4)$$

resulting after integration by parts in the following weak formulation with an arbitrary test function φ :

$$0 = \int_{\Omega} \varphi \partial_t h \, dx - \int_{\Omega} M(h) \nabla w \cdot \nabla \varphi \, dx + \int_{\partial\Omega} \varphi M(h) \nabla w \cdot \mathbf{dS} \quad (4.5)$$

$$0 = \int_{\Omega} (-w - f'(h)) \varphi - \nabla h \cdot \nabla \varphi \, dx + \int_{\partial\Omega} \varphi \nabla \cdot \mathbf{dS}. \quad (4.6)$$

Note that the gradient dynamics structure of the thin-film equation suggests a natural splitting and weak formulation. Boundary conditions can be implemented in the boundary integrals in (4.5) and (4.6). For so called *no-flux boundary conditions* ($\nabla h \cdot \mathbf{dS} = \nabla w \cdot \mathbf{dS} = 0$), the boundary integrals vanish. For more details on the employed finite element method, we refer to [Wil16].

In contrast to the NTS discussed above, numerical continuation of steady state solutions allows for the calculation of stable *and* unstable steady state solutions of the considered evolution equations. Here, solution branches are followed in parameter space, employing specific algorithms like, e.g., *pseudo-arclength continuation* that are able to track solution families along *folds*, e.g., saddle-node bifurcations. For details on continuation techniques, we refer to [DKK91a, DKK91b]. In the present thesis, we employ the software AUTO-07p [DOO12] which allows for the implementation of 1D steady state equations of PDEs as boundary value problems (BVPs). Here, the spatial discretization is adaptive. Furthermore, the software allows for the detection of local bifurcations, branch switching and two-parameter continuation of, e.g., fold points. In addition, for ODEs, also the continuation of time-periodic solutions is possible. For tutorials on the continuation of equations from soft matter theory with AUTO-07p, we refer to [TKG14].³

4.2.3 Steady State Solutions

First, we are interested in steady state solutions h_0 of (4.3) for one spatial dimension of the substrate (on a domain $\Omega = [0, L]$). Obviously, these solutions are also steady states in 2D, when they are continued in the second spatial direction (here y -direction). Their stability in the 2D case will be the topic of the next subsection.

We consider (4.3) with periodic boundary conditions on a domain $[0, L]$. The steady state equation obtained by setting $\partial_t h \equiv 0$ can be integrated once with a vanishing integration constant due to the boundary conditions. Upon the second integration, we obtain a constant that we denote as the *chemical potential* μ [PP00, Pis04]:

$$-\partial_{xx}h + f'_{\text{pre}}(h, x) = \mu. \quad (4.7)$$

This latter constant is directly related to the mass in the system, in fact (4.7) is also obtained through the requirement that the energy functional \mathcal{F} given by (3.35) with $f = f_{\text{pre}}$ is minimized under the constraint that a certain mean mass $m = \frac{1}{L} \int_0^L dx h(x)$ is contained in the system:

$$\frac{\delta \mathcal{F}}{\delta h} - \mu \frac{\delta}{\delta h} \left(\int_0^L dx h - m \right) = 0 \Leftrightarrow (4.7). \quad (4.8)$$

In this sense, μ is a Lagrangian multiplier for a mass constraint.

In FIG. 4.3, we show bifurcation diagrams for droplets (or ridges) on homogeneous substrates (i.e., $\rho = 0$) for fixed mean mass: Starting from a flat film solution, the domain size L is increased (FIG. 4.3 (a)). The droplet solution branch bifurcates subcritically at a domain size

³ Part of the continuation codes employed in the present thesis were adapted based on codes made available in the context of [TKG14].

$L_{\text{crit}} = 2\pi/\sqrt{f''(m)}$, where m is the flat film height (or equivalently the mean mass). As a solution measure, the following quantity is employed:

$$\mathcal{N}[h, \partial_x h] = \sqrt{\frac{1}{L} \int_0^L dx h^2 + (\partial_x h)^2}. \quad (4.9)$$

The droplet solution corresponding to the uppermost branch (cf. solution II in FIG. 4.3 (b)) shall be shortly discussed in more detail (cf. [GW03]): At the boundaries of the domain, the solution is approximately given by a flat film of height h_a defined by

$$\mu = f'(h_a). \quad (4.10)$$

The value of h_a corresponds to the finite domain adsorption layer height, for $L \rightarrow \infty$ follows $\mu \rightarrow 0$, and given (4.10) one obtains h_a as the minimum of the binding potential in this limit.

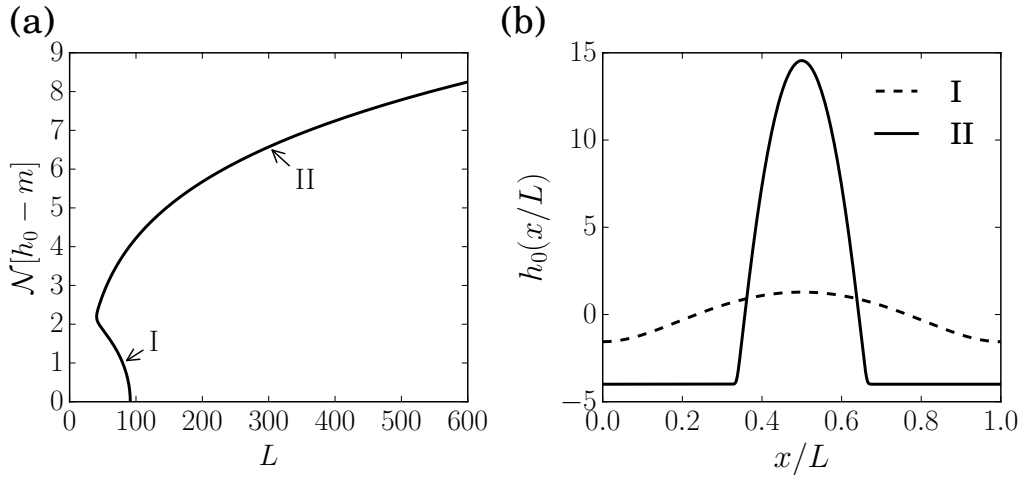


Figure 4.3: (a) Bifurcation diagram showing the norm of the solutions vs. the length of the domain with fixed average mass. The droplet solution type II shown in (b) emerges subcritically from the flat film (cf. [TVN01a]).

In the core region of the droplet, the height becomes significant enough for the contribution of the binding potential to be neglected. The steady state equation then reduces to

$$\mu = -\partial_{xx}h \Leftrightarrow h = \frac{-\mu x^2}{2} + C \quad (4.11)$$

and a parabola type solution is obtained. In the intermediate region, the approximate steady state equation reads [GW03]

$$0 = -\partial_{xx}h + f(h) \quad (4.12)$$

and the equilibrium apparent contact angle is obtained as

$$\theta_{\text{eq}} = \sqrt{2|f(h_a)|}. \quad (4.13)$$

Apart from solutions consisting of a single droplet of a given mass, which are stable in 1D, as implied by the periodic boundary conditions, equidistant arrays of droplets can also be obtained as (unstable) steady state solutions for sufficiently large system sizes L . For heterogeneous substrates, a larger set of stable and unstable solutions can be obtained. In §4.2.5, we discuss an exemplary non-trivial case of a heterogeneous substrate with two adjacent prepattern patches, where the distance d does not correspond to the halflength $L/2$ of the domain.

4.2.4 Transversal Stability of a Single Ridge

When considering a single liquid ridge on a chemically and topographically homogeneous substrate, one finds that this structure is always unstable with respect to a Plateau-Rayleigh type instability [MOR⁺07]. A system, where a single ridge is placed on a prepattern stripe has been recently studied in terms of a transversal stability analysis in the framework of the thin-film equation [TBBB03, MRD08, HLH⁺15]. In this subsection, we mainly reproduce numerically some general results found in [MRD08] for our specific choice (4.1) of the binding potential and formulate a heuristic derivation of the general results based on a different argumentation, similar to the one employed in [MOR⁺07].

The NTS shown in this and the two subsequent subsections are performed on a domain $A = [0, L] \times [0, L_y]$ with periodic boundary conditions and a finite element discretization on a rectangular grid with $dx = dy = 1.0$. In FIG. 4.4, we show snapshots of a NTS of a bulge forming transversal instability occurring for a ridge on a single prepattern stripe. For the 2D case, the mean mass is given by $m = \frac{1}{L_y L} \int_A dx h(x)$, all parameters can be found in the caption of FIG. 4.4. The simulation is initialized by a parabola cap of appropriate mass on top of a homogeneous film which is approximately of the adsorption layer height and small random noise. Before the transversal instability sets in, the ridge first quickly relaxes to a almost longitudinally homogeneous ridge, where the cross-section is given by the solution $h_0(x)$ of the 1D version of the steady state equation (4.7).

In order to quantify the linear growth of modulations of the ridge (specified by the 1D steady state solution h_0) in longitudinal (y -direction), the following ansatz can be inserted into equation (4.3) [TBBB03, MRD08, HLH⁺15]:

$$h(\mathbf{x}, t) = h_0(x) + \varepsilon h_1(x) e^{iky + \beta(k)t}. \quad (4.14)$$

Upon linearization in the smallness parameter ε , the following leading order eigenvalue problem is obtained [MRD08, HLH⁺15]:

$$\beta(k)h_1 = \mathfrak{L}[h_0, k]h_1, \text{ where} \quad (4.15)$$

$$\begin{aligned} \mathfrak{L}[h_0, k]h_1 = & M(h_0)(\partial_{xx} - k^2) \left((-\partial_{xx} + k^2) h_1 + f''_{\text{pre}}(h_0)h_1 \right) + \\ & (\partial_x M(h_0))\partial_x \left((-\partial_{xx} + k^2) h_1 + f''_{\text{pre}}(h_0)h_1 \right). \end{aligned} \quad (4.16)$$

The eigenvalue problem (4.16) can be solved numerically employing continuation techniques (cf. [Hon13] for a detailed description) in order to obtain the *dispersion relation* $\beta(k)$ for the growth of modulations in transversal direction. The two largest eigenmodes of the operator \mathfrak{L} are shown in FIG. 4.5 (a). For $k = 0$, i.e., effectively in the 1D case, the eigenvalues of both modes converge to $\beta(k = 0) = 0$. In the limiting case of $k = 0$ and $\rho = 0$, the modes correspond to *Goldstone modes* [GW03] as induced by two different symmetries of (3.36): The dominant

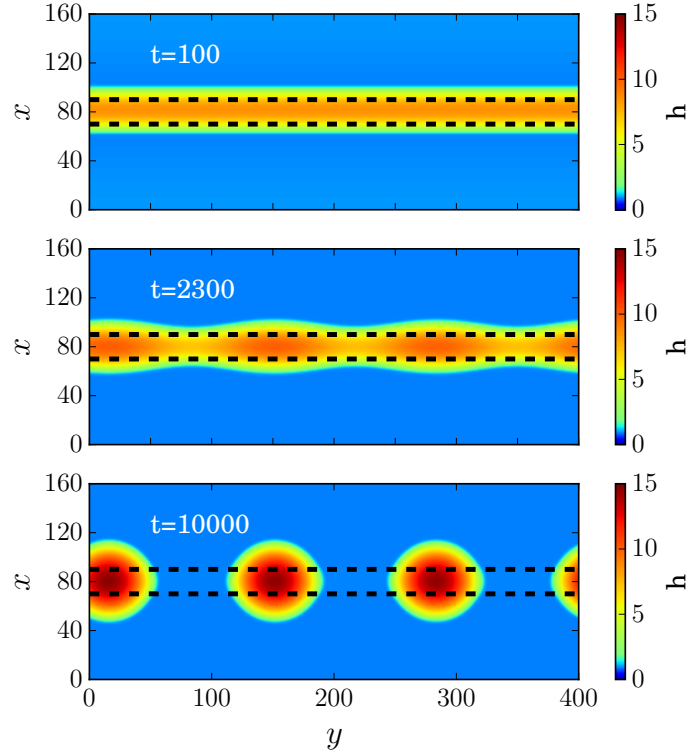


Figure 4.4: Snapshots of a NTS of (4.3) on a domain of $L = 160, L_y = 400$ with $w/L = 0.125$, $m = 2.25$ and $\rho = 0.2$. As also in the experimental picture FIG. 4.1, the bulges formed due to the instability are deformed by reason of the underlying prepattern.

mode corresponds to the translational symmetry in 1D and reads $h_1^t(k = 0, \rho = 0) = \partial_x h_0$. The second mode results from another symmetry of (3.36), specifically the one with respect to mass change and corresponds to $h_1^\mu(k = 0, \rho = 0) = \partial_\mu h_0$.

The dispersion relations for both dominant modes are shown in FIG. 4.5 (b). The mode h_1^μ leads to a periodic redistribution of mass along the ridge in 2D. The mode h_1^t is often referred to as the *zigzag mode* [TBBB03, HLH⁺15]. While the mode h_1^t is always stable, h_1^μ is in general unstable for sufficiently small wavenumbers k and is only stabilized for certain values of ρ , depending on the mass of the ridge and the prepattern geometry. In [MOR⁺07] it is shown for the thin-film equation, that h_1^μ is in fact always unstable for the case $\rho = 0$. The instability due to this mode will be termed *Plateau-Rayleigh instability* in the following. In FIG. 4.5, it can be clearly seen that for the prepattern geometry employed in the respective calculations, the Plateau-Rayleigh instability is suppressed due to the prepattern above a certain value of ρ . In the following, we analyze the stability diagram of ridges on a single prepattern stripe in the parameter space spanned by the mass in the system and the strength ρ of the prepattern. In doing so, we reproduce a general result obtained in [MRD08] by using a different, more heuristic reasoning (which is similar to the one outlined in [MOR⁺07] for the case of homogeneous substrates).

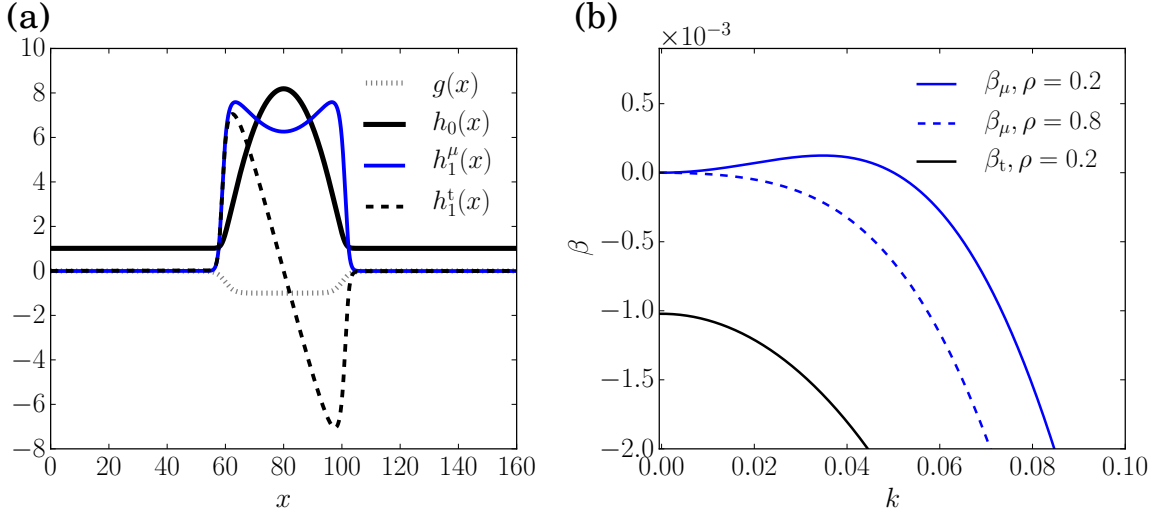


Figure 4.5: (a) Stationary solution of (4.3) and the two dominant eigenmodes of the linear operator in (4.16) for $\rho = 0.2$ and $k = 0.005$. (b) Dispersion relation for the two dominant modes at $\rho = 0.2$, $w/L = 0.25$, $L = 160$. Note that the eigenvalue β_t corresponding to h_1^t is always negative while h_1^μ is unstable for small enough wavenumbers k . The dispersion relation of the mode h_1^μ is shown for $\rho = 0.2$ and $\rho = 0.8$, respectively. For the latter case, the eigenvalue is non-positive and thus a stabilization due to the prepattern is found (cf. [HLH⁺15, TBH⁺17]).

Since (4.3) is a gradient system, its energy functional \mathcal{F} is strictly decreasing in time. We consider now the energy increment $\delta\mathcal{F}$ resulting from a small mass-conserving deviation $\varepsilon\tilde{h}$ from the stationary solution h_0 :

$$\delta\mathcal{F} = \underbrace{\varepsilon \int_A \frac{\delta\mathcal{F}}{\delta h} \Big|_{h_0} \tilde{h} \, dx}_{=0} + \underbrace{\frac{1}{2}\varepsilon^2 \int_A f''_{\text{pre}}(h_0, x) \tilde{h}^2 + (\nabla\tilde{h})^2 \, dx}_{:= \frac{\delta^2\mathcal{F}}{\delta h^2} : \tilde{h} : \tilde{h}} + \text{h.o.t.}, \quad (4.17)$$

where the first summand vanishes due to the stationarity of \mathcal{F} at $h = h_0$ and the mass conservation constraint on the perturbation \tilde{h} . A necessary condition for the linear stability is therefore that for all perturbations \tilde{h} , the remaining two leading order summands given by the bilinear form $\frac{\delta^2\mathcal{F}}{\delta h^2} : \tilde{h} : \tilde{h}$ in (4.17) are positive (cf. [MOR⁺07]):

$$\frac{\delta^2\mathcal{F}}{\delta h^2} : \tilde{h} : \tilde{h} > 0. \quad (4.18)$$

We consider now a scaled perturbation of the form $\tilde{h}_m = \frac{1}{A} \partial_m h_0 e^{iky} (= \frac{1}{A} \frac{\partial \mu}{\partial m} \partial_\mu h_0 e^{iky})$ and assume that this perturbation is the first to become unstable. Furthermore, we focus on the limit $k \rightarrow 0$.⁴ The leading order energy perturbation then reduces to

$$\frac{\delta^2 \mathcal{F}}{\delta h^2} : \tilde{h}_m : \tilde{h}_m = \frac{1}{L} \int_0^L dx f_{\text{pre}}''(h_0, x) (\partial_m h_0)^2 + (\nabla \partial_m h_0)^2 \stackrel{(4.7)}{=} \frac{\partial \mu}{\partial m} \frac{1}{L} \int_0^L dx \partial_m h_0 = \frac{\partial \mu}{\partial m}. \quad (4.19)$$

Therefore, following this reasoning, the stability threshold is obtained as the set of values of m and ρ where

$$\frac{\partial \mu}{\partial m} = 0. \quad (4.20)$$

This result is also obtained from a perturbation analysis of the eigenvalue equation (4.16) in [MRD08]. The derivation shown here is more heuristic but highlights the concept that the stability limit is encoded in the energy functional.

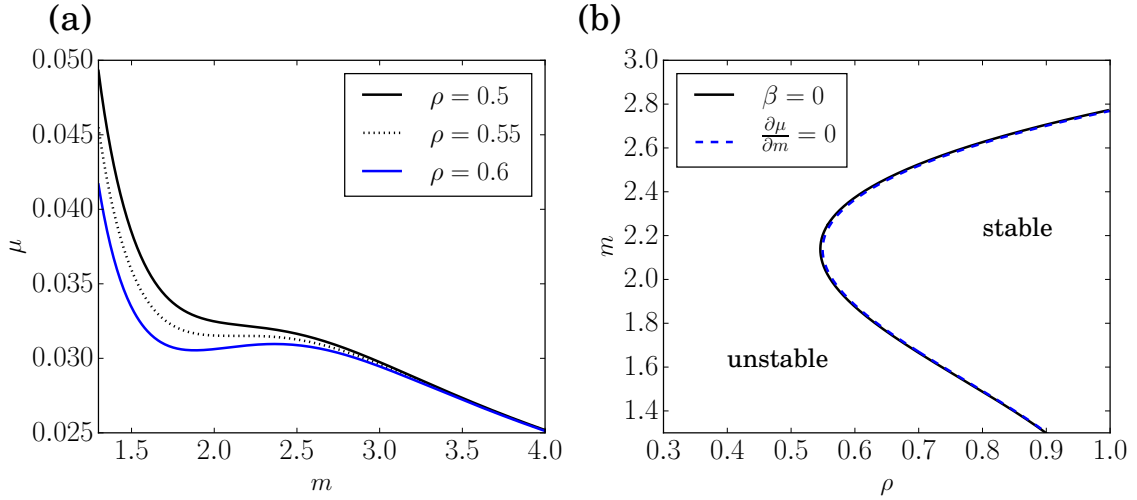


Figure 4.6: (a) Chemical potential μ vs. mean mass m for a single drop solution in 1D for different values of the prepattern strength ρ , obtained by numerical continuation. A transition from a monotonous dependence of μ on m to a non-monotonous dependence (cf. [MRD08]) can be seen around $\rho \approx 0.55$. For sufficiently high values of ρ , a set of m for which $\partial_m \mu > 0$ is found and delimited by two local extrema corresponding to the limit of the transversal stability region according to (4.20). (b) Stability diagram for a single drop with prepattern width $w = 0.25L$ and $L = 160$. The stability limit, as calculated by a two-parameter continuation of the onset of instability obtained from (4.16), is in excellent agreement with the stability limit calculated according to (4.20).

⁴ For this case, the perturbation is not mass conserved, however it is instructive as a limiting case.

In FIG. 4.6 (a), we show the transition of the function $\mu(m)$ for different values of ρ exhibiting a mathematical structure similar to a second order phase transition. Two *pinned* volumes emerge above a certain critical value of ρ and delimit the stable region of the ridge. In comparison to the stability limit obtained from the heuristic argumentation, we show the numerically calculated stability limit from the continuation (cf. FIG. 4.5 (b)). The stability limit obtained from the condition (4.20) can be conveniently calculated by a *fold continuation*. It should be emphasized that the criterion (4.20) only necessitates an investigation of the energetics of 1D stationary solutions. The underlying assumptions are that the mass mode h_m is the first to become unstable and the instability is long-wave (i.e., the onset is at $k = 0$).

We now proceed with an investigation of the stability of a structure on a more involved prepattern.

4.2.5 Transversal Stability of Two Adjacent Ridges

In general, on a homogeneous substrate (with periodic boundary conditions), no stationary two-droplet configurations can be found where the distance of the droplets is not equal to the half of the domain size. However, for a chemically prepatterned substrate, such solutions can be obtained and an example is given in FIG. 4.7. Analogously to the case of a single ridge, we now analyze the stability of two such adjacent prepattern stripes. Once again, the ansatz (4.14) is inserted in (4.3) where now h_0 is the stationary two-droplet solution (cf. FIG. 4.7 (a)). In FIG. 4.7, we show the resulting dominant eigenmodes and their corresponding dispersion relation for this system.

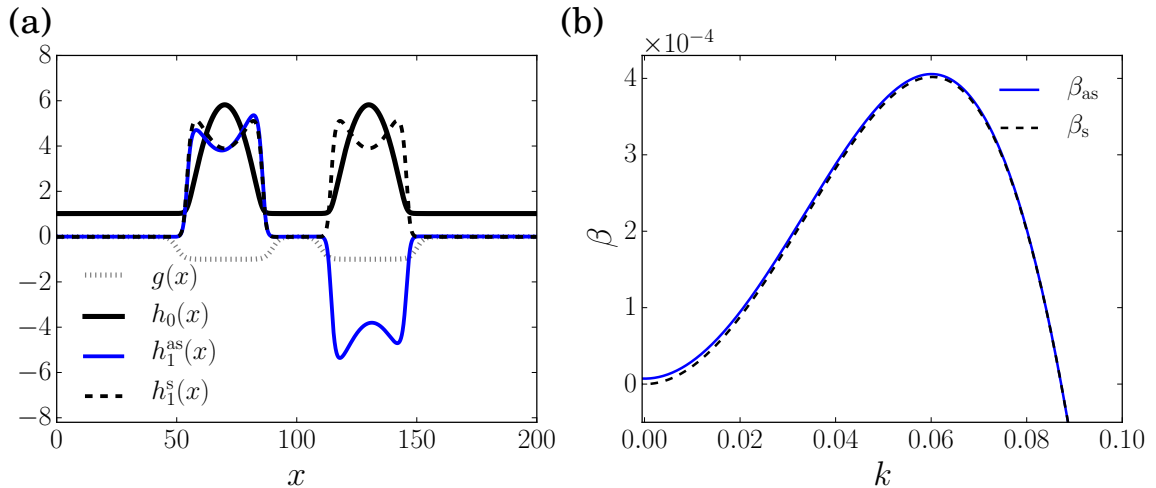


Figure 4.7: (a) Stationary solution of (4.3) for two prepattern stripes and the two dominant eigenmodes of the linear operator in (4.16) for $\rho = 0.2$, $k = 0.005$, $w/L = 0.2$, $d/L = 0.1$, $L = 200$. (b) Dispersion relation for the two dominant modes at $\rho = 0.2$. The eigenvalue β_{as} corresponding to h_1^{as} does not vanish in the limit $k \rightarrow 0$ (cf. [TBH⁺17]).

The first mode h_1^s corresponds to a simultaneous mass redistribution within both ridges along the y -direction and is analogous to the mode h_1^u for the case of a single ridge. Accordingly, this mode is not mass-conserving for $k = 0$ and its eigenvalue converges to zero in this limit. The second unstable mode h_1^{as} corresponds to an antisymmetric mass transfer along and between the ridges. For $k = 0$, the eigenvalue of this mode has a finite value, accounting for the fact that the stationary solution h_0 is unstable in 1D w.r.t. mass transfer from one droplet to the other due to the weak interaction of the two droplets (or ridges) through the adsorption layer. However, for the dominant values of k , both modes have almost identical eigenvalues. Therefore, in direct numerical simulations, depending on the initial noise, a growth of either one of the modes or a combination of both can be found (cf. FIG. 4.8). A stabilization of the mass exchanging mode h_1^{as} in 1D for two droplets is discussed through a detailed numerical bifurcation analysis in [BKTB02]. Note also the slight asymmetry of the extrema of the mode h_1^{as} , in contrast to the extrema of the eigenfunction h_1^s , which can also be attributed to the weak interaction of the ridges. If the mode h_1^{as} would correspond precisely to the half-inverted mode h_1^s , a separate growth of instability of one single ridge would be conceivable (corresponding to a growth of $h_1^s \pm h_1^{as}$). Due to the asymmetry present in each half-space, this is not possible for the weakly interacting ridges.

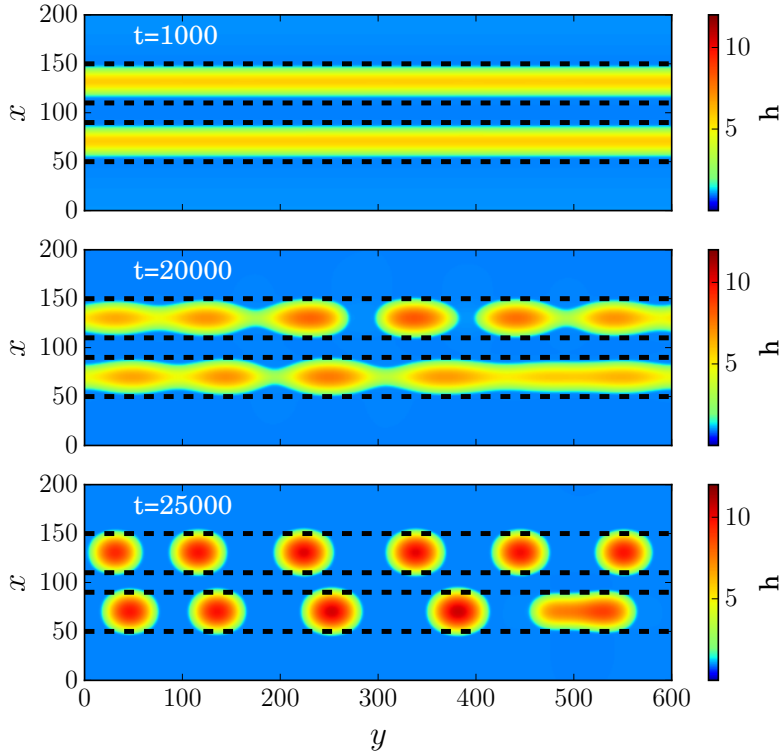


Figure 4.8: Snapshots of a NTS of (4.3) for two prepattern stripes of individual width $w/L = 0.2$ and with $\rho = 0.2$, $d/L = 0.1$, $L = 200$. Both ridges break up simultaneously and a growth of a combination of the two unstable modes h_1^{as} can be inferred (cf. [TBH⁺17]).

4.2.6 Coarsening and Transversal Instabilities

As shown in detail in [GW03], the coarsening of droplets (or ridges) on a homogeneous substrate occurs due to two main mechanisms: mass transfer through the adsorption layer and coarsening through coalescence of neighboring droplets, which are attracted due to the fluxes through the adsorption layer. While the latter mechanism can be suppressed through heterogeneities on the substrate, which result in pinning forces, the coarsening through diffusion on the other hand can play an important role for the stability of liquid structures on prepatterned substrates. An experimental example is shown in FIG. 4.9, where in the aforementioned deposition experiments [WDW⁺11], two different spacings between prepattern stripes of different width are investigated. Independent of the width of the stripes, roughly the same amount of molecules are deposited, such that the ridge formed on the narrow stripe is transversally unstable. According to [WDW⁺11], for the case of the smaller distance between the stripes, diffusion from the narrow to the wider stripes is fast enough to prevent the transversal instability on the narrow ones. For a greater distance, the diffusion is less significant and the transversal instability sets in. While this phenomenon possibly occurs during the deposition process, we investigate the described mechanism without condensation terms.

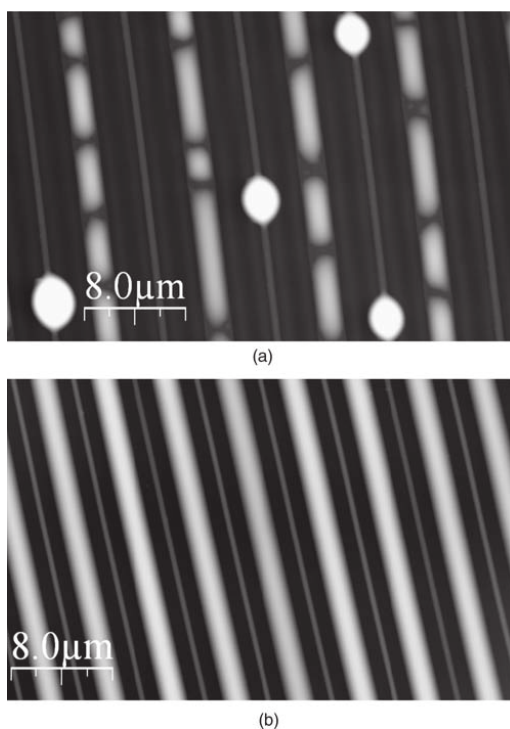


Figure 4.9: AFM pictures of structures formed in the deposition experiments [WDW⁺11] for two different spacings of the prepattern stripes of different width. For large distances, the diffusion is too slow to inhibit the transversal instability (cf. (a)), whereas for small distances (cf. (b)) the diffusion removes enough mass from the narrow prepattern stripe to stabilize it. Picture reproduced with permission from [WDW⁺11], © WILEY- VCH Verlag GmbH & Co. KGaA.

In FIG. 4.10, we show the time evolution of the mass over adsorption layer of a ridge on a prepattern stripe of width $w_1 = 40$, which is growing due to diffusion of mass from an adjacent ridge on a prepattern stripe of width $w_2 = 25$ for three different distances of the ridges. The simulations are performed with periodic boundary conditions and a transversal length $L = w_1 + w_2 + 2d$ in such a way that a periodic array of prepattern stripes with a single distance is simulated, the prepattern strength is $\rho = 0.93$. As expected, the coarsening rate increases for smaller distances. As a consequence, we also find in 2D simulations for small distances of the prepattern stripes (cf. FIG. 4.11) a sufficiently fast coarsening for the suppression of the Plateau-Rayleigh instability of the ridge on the narrow prepattern stripe. In contrast, for sufficiently large distances (cf. FIG. 4.12) and for approximately the same initial mass of both ridges, due to the slower coarsening, the instability sets in.⁵

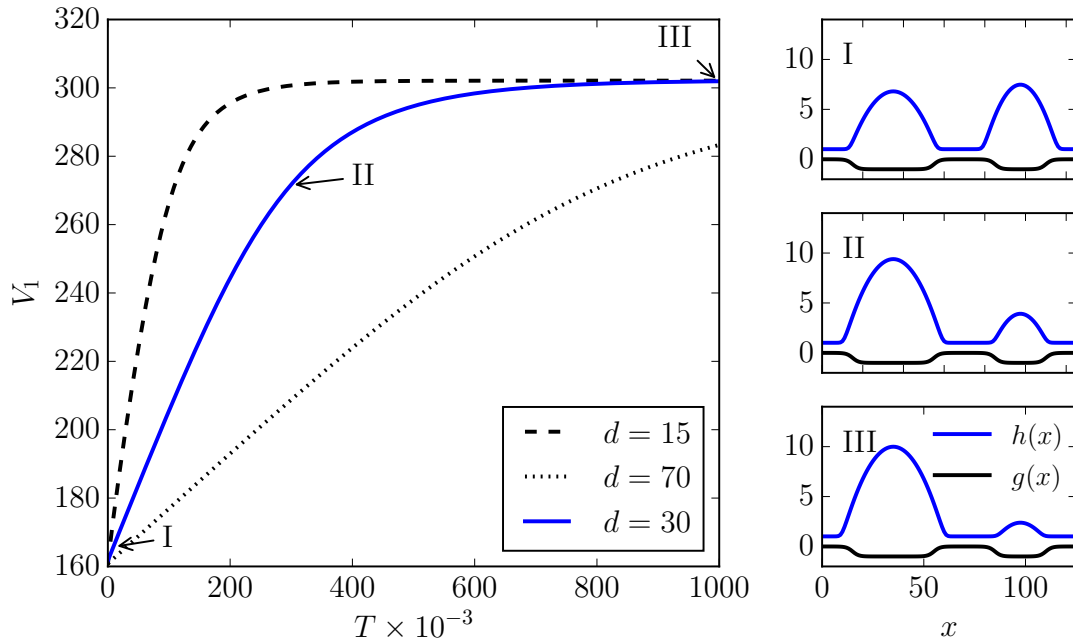


Figure 4.10: Time evolution of the mass of the ridge on a stripe of width $w_1 = 40$ adjacent to a ridge of initially the same mass with a width of $w_2 = 25$ shown for three different distances of the prepattern stripes ($d = 15, 30, 70$) and $\rho = 0.93$. For $d = 30$, snapshots of the NTS in 1D are shown together with the prepattern function. The coarsening rate increases significantly with decreasing distance of the ridges.

⁵ Obviously, this phenomenon heavily depends on the initial noise, in the NTS shown in FIG. 4.11 and FIG. 4.12, respectively, the noise amplitude on the initial parabola caps is chosen as $\Delta h_{\text{noise}} = 0.2$. However, the qualitative and systematic effect of the distance on the coarsening rate is robust.

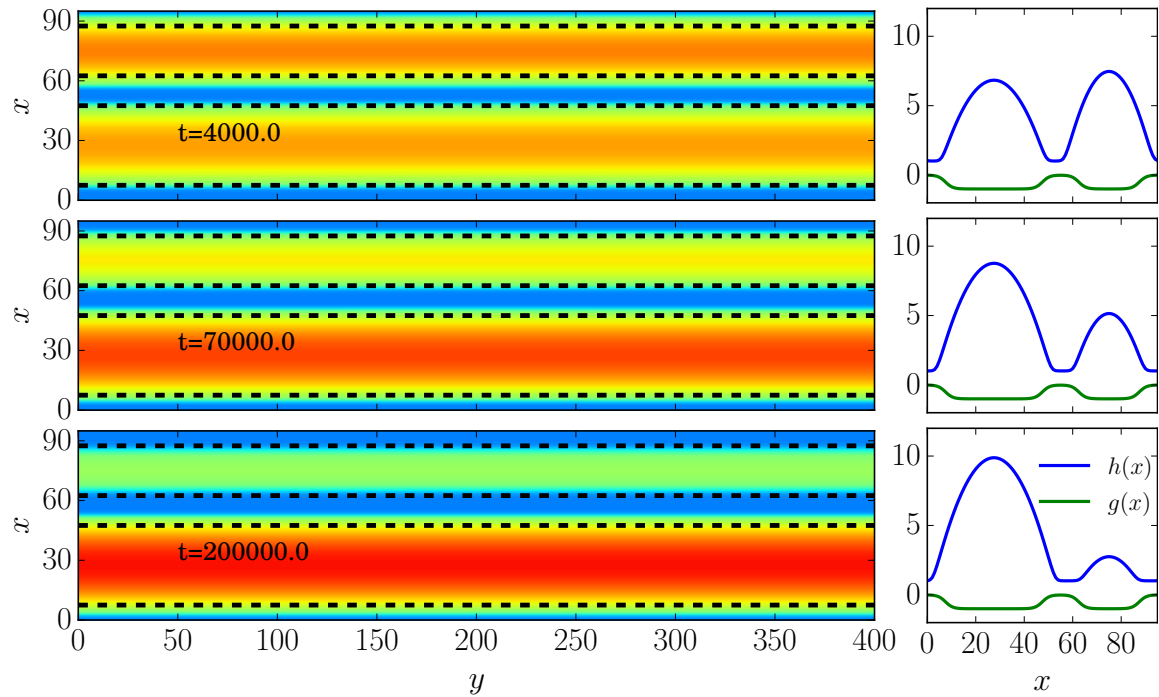


Figure 4.11: Snapshots of a 2D NTS of two ridges on prepattern stripes of widths $w_1 = 40$ and $w_2 = 25$ in a distance $d = 15$ on a domain with $L = w_1 + w_2 + 2d$ and $L_y=400$. For each snapshot, we show the full 2D field and additionally a cross section of the height field with the corresponding prepattern function $g(x)$ at $y = L_y/2$. In this simulation, the coarsening outruns the transversal instability and no formation of bulges is observed.

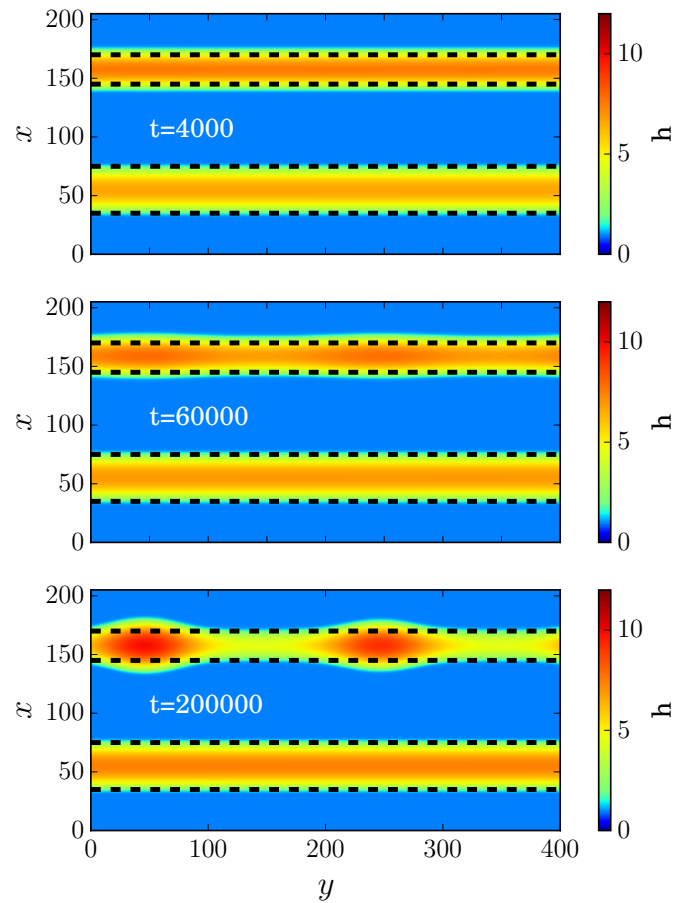


Figure 4.12: Snapshots of a 2D NTS with the same prepattern widths as in FIG. 4.11 but with a distance $d = 70$ on a domain with $L = w_1 + w_2 + 2d$ and $L_y = 400$. The coarsening towards the ridge on the broader prepattern stripe occurs on a larger timescale and the transversal instability on the ridge on the narrow stripe sets in. Note that the diffusion continues in spite of the transversal instability.

4.3 Comparison of Kinetic Monte Carlo Modeling and Thin-Film Modeling⁶

Subject of this section is a systematic comparison of simulations of Plateau-Rayleigh instabilities based on a kinetic Monte Carlo (KMC) algorithm and results obtained for the already introduced thin-film equation.⁷ The presentation in this section mostly follows along the lines of [TBH⁺17]. In the subsequent section, approaches for the quantitative mapping are discussed.

4.3.1 KMC Modeling

Experimentally, the behavior of the organic molecules in [WC12, WDW⁺11] is interpreted as liquid-like. However, due to the small scales of the structure in question, a modeling of the deposition process and subsequent relaxation (e.g., instabilities of ridges) of the molecules by an approach which is less coarse-grained than the thin-film equation is of interest. Two commonly encountered microscopic modeling approaches for molecules on substrates are *molecular dynamics* (MD) simulations [KLRD06] and KMC simulations (cf. [CSA17b]). Here, we focus on KMC simulations, which have successfully been employed in the modeling of the experimental systems in question [LMW⁺12].

The KMC model considered in this work is based on a lattice gas Hamiltonian which gives the energy associated with an occupation of the three dimensional lattice. In particular, the Hamiltonian for a system of a single particle type on a substrate with prepattern regions reads:

$$H = -\epsilon_{pp} \frac{1}{2} \sum_{\mathbf{i}, \mathbf{j}} f(r_{\mathbf{ij}}) p_{\mathbf{i}} p_{\mathbf{j}} - \epsilon_{pg} \frac{1}{2} \sum_{\mathbf{i}, \mathbf{j}} h(r_{\mathbf{ij}}) p_{\mathbf{i}} g_{\mathbf{j}} - \epsilon_{ps} \frac{1}{2} \sum_{\mathbf{i}, \mathbf{j}} h(r_{\mathbf{ij}}) p_{\mathbf{i}} s_{\mathbf{j}}. \quad (4.21)$$

The binary values of $p_{\mathbf{i}}, g_{\mathbf{i}}, s_{\mathbf{i}} \in \{0, 1\}$ indicate whether the lattice site $\mathbf{i} = (i_x, i_y, i_z)$ is occupied by a particle ($(p_{\mathbf{i}}, s_{\mathbf{i}}, g_{\mathbf{i}}) = (1, 0, 0)$), corresponds to a part of the substrate without prepattern ($(p_{\mathbf{i}}, s_{\mathbf{i}}, g_{\mathbf{i}}) = (0, 1, 0)$), corresponds to a prepatterned part ($(p_{\mathbf{i}}, s_{\mathbf{i}}, g_{\mathbf{i}}) = (0, 1, 0)$) or, finally, is empty ($(p_{\mathbf{i}}, s_{\mathbf{i}}, g_{\mathbf{i}}) = (0, 0, 0)$). Obviously, the occupation of a lattice site by a particle or by the substrate is mutually exclusive. The pair interaction energies for different occupations of interacting sites are given by $\epsilon_{pp}, \epsilon_{pg}$ and ϵ_{ps} . The interaction length between substrate and particles and of the particle-particle interaction is specified by the function $f = h$. The value $r_{\mathbf{ij}}$ is the distance between the lattice sites specified by \mathbf{i} and \mathbf{j} , respectively. For simulations shown in the present section, interactions up to the third nearest neighbor (common corner) are considered:

$r_{\mathbf{ij}}/a$	0.0	1.0	$\sqrt{2}$	$\sqrt{3}$	$> \sqrt{3}$
$f(r_{\mathbf{ij}})$	0.0	1.0	1.0	0.5	0.0

While the occupation of the lattice sites by the substrate is kept constant for obvious reasons, the occupation state of the remaining lattice sites by particles is simulated dynamically based on the so-called *Kawasaki dynamics* [Kaw72]: At each time step Δt of the KMC algorithm,

⁶ The work presented in this section is a collaboration with Oleg Buller. The KMC simulations have been conducted by O. Buller, whereas the NTS and analysis of the thin-film model has been carried out by W.T.. The systematic comparison has been elaborated in close cooperation and the work was jointly published in [TBH⁺17].

⁷ In contrast to the results in the previous section, we use a slightly different prepattern function than (4.2):

$$g(x) = 1.0 + \sum_{j=1}^{2n} (-1)^j \tanh((x - x_j)/l_s).$$

each particle does a random trial move onto one of the nearest neighbour sites. If this site is empty, the move is evaluated according to the so-called Metropolis criterion [MRR⁺53]. The Hamiltonian for the configuration given the move is effectuated is compared to the previous value of the Hamiltonian. If the move decreases the energy, it is accepted. If the energy increases by ΔH , the move is accepted with a probability given by [MRR⁺53]

$$P_{\text{Metropolis}} = e^{-\Delta H/k_{\text{B}}T}. \quad (4.22)$$

An important property of Kawasaki dynamics is the conservation of the number of particles in each time step. From a thermodynamic point of view, at equilibrium, this corresponds to the *canonical ensemble*, in contrast to the *grand canonical ensemble*, where the chemical potential fixes only the mean of the stochastically varying particle number.

4.3.2 Plateau-Rayleigh Instabilities in the KMC Model - Comparison to Thin-Film Modeling

As already mentioned, the instability of ridges on stripe-prepatterned substrates as observed in the KMC model shall be compared systematically with corresponding results for the thin-film model. As initial conditions for the NTS of the thin-film model, we use 1D profiles continued in the second dimension of the substrate and subjected to small random noise. However, the choice of appropriate initial conditions for the KMC model is less obvious.

We pursue the following procedure: First, a density profile of a droplet on a 2D lattice (1D substrate) is calculated by averaging over 2000 realizations of occupation fields after relaxation to a droplet. An example of a resulting density field is shown in FIG. 4.13. Then, along the longitudinal direction, for each "slice" of the ridge, i.e., for $y = 0, \dots, L_{y-1}$, we generate an individual particle configuration by assigning the appropriate fixed number of particles to the lattice in accordance with the probabilities given by the density field. For this purpose, we employ the following algorithm: We iterate randomly over all lattice sites which are not occupied by the substrate. Whenever the lattice site is empty, a particle is placed on it with a probability corresponding to the density $p = \rho(x, z)$ at the site. In contrast, whenever the site is already filled with a particle, this particle is *removed* with the complementary probability $p = 1 - \rho$. This procedure is iterated until the desired number of particles is placed on the grid. The transversal instability of the ridge is now observed in direct simulations according to the

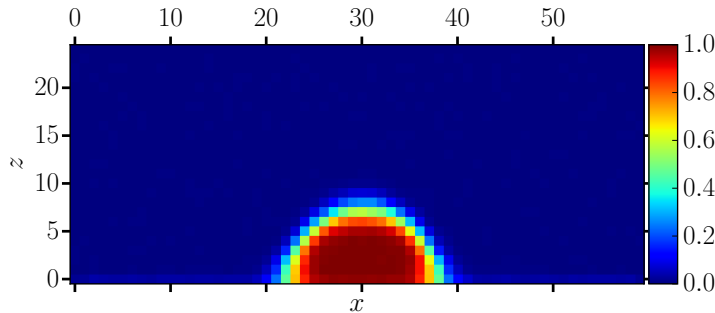


Figure 4.13: Density field obtained by averaging over 2000 realization of particles forming a droplet after relaxation in the KMC simulations. This density field is employed to generate initial conditions for the ridge. Figure reproduced from [TBH⁺17].

KMC algorithm described in §4.3.1 and can be compared to results from thin-film modeling. The different parameter sets employed for the KMC simulations shown in the following are

set	$\epsilon_{pp}/k_B T$	$\epsilon_{ps}/k_B T$	$\epsilon_{pg}/k_B T$
P1	1.0000	0.5000	0.7000
P2	0.6250	0.3125	0.4375

In order to obtain a measure for the time evolution of the instability, we calculate the absolute values of the Fourier modes of the fields integrated in x -direction. More precisely, for the KMC model, we consider ⁸

$$|\mathcal{FT}[m_y](k_y, t)| = \left| \sum_{n_y=0}^{L_y-1} m_y(n_y, t) e^{-2\pi i \frac{n_y k_y}{L_y}} \right|, \quad m_y(n_y, t) = \sum_{n_x, n_z} P(n_x, n_y, n_z), \quad (4.23)$$

whereas for the thin-film model, the analogous quantity reads

$$|\mathcal{FT}[m_y](k_y, t)| = \left| \int m_y(y, t) e^{-2\pi i \frac{k_y y}{L_y}} dy \right|, \quad m_y(y, t) = \int h(x, y, t) dx. \quad (4.24)$$

These quantities can be seen as measures for the mass redistribution along the longitudinal direction due to the Plateau-Rayleigh instability. The time evolution of $|\mathcal{FT}[m_y]|$ for the three first modes ($k_y = 1, 2, 3$) is shown for the KMC and the thin-film model in FIG. 4.14, combined with snapshots of the corresponding simulation. Although the time evolution for the KMC model is obviously noisy, a clearly exponential growth of the dominant mode can be identified for both models. In particular, the exponential regime reaches well beyond the stage of the breakup which would be considered as nonlinear by inspection of the snapshots (cf. FIG. 4.14 (b), (d)).

This extended regime of exponential growth allows for a convenient measurement of the growth rate of the instability in the KMC model and thus for a partial extraction of the dispersion relation from the simulations. To do so, we restrict the longitudinal size L_y of the simulation domain and measure the quantity $|\mathcal{FT}[m_y]|$ for the dominant mode. The growth rate β is then obtained by an exponential fit (i.e., with a fit function $f(t) = ae^{\beta t}$). For each wavenumber k_y , all simulations are averaged that have a fit error below 3%. In this way, an averaged growth rate $\langle \beta \rangle(k_y)$ is obtained. In FIG. 4.15 results for the averaged dispersion relation for the two parameter sets P1 and P1 and for prepattern stripe widths $w = 10$ and $w = 14$ are shown for the KMC model in comparison to dispersion relations for two different prepattern stripe widths in the thin-film model (cf. [TBH⁺17]). In the thin-film and the KMC model, a smaller width of the prepattern stripe results in larger maxima of the dispersion relation which are found at higher wavenumbers. This is in qualitative agreement with the experimental findings shown in FIG. 4.1.

For the KMC model, higher temperatures (parameter set P2) equally result in larger growth rates of the transversal instability. Due to the nondimensional form of the thin-film equation (4.3) a change of temperature is not investigated explicitly. However, the following reasoning shows the qualitative consistency: A higher temperature manifests itself in a decreased value of the viscosity η . Considering the scaling used in §3.2.2 one finds that the physical growth rate is inversely proportional to the viscosity, and thus increases with the temperature.

⁸ Here, $P(n_x, n_y, n_z)$ denotes the occupation state.

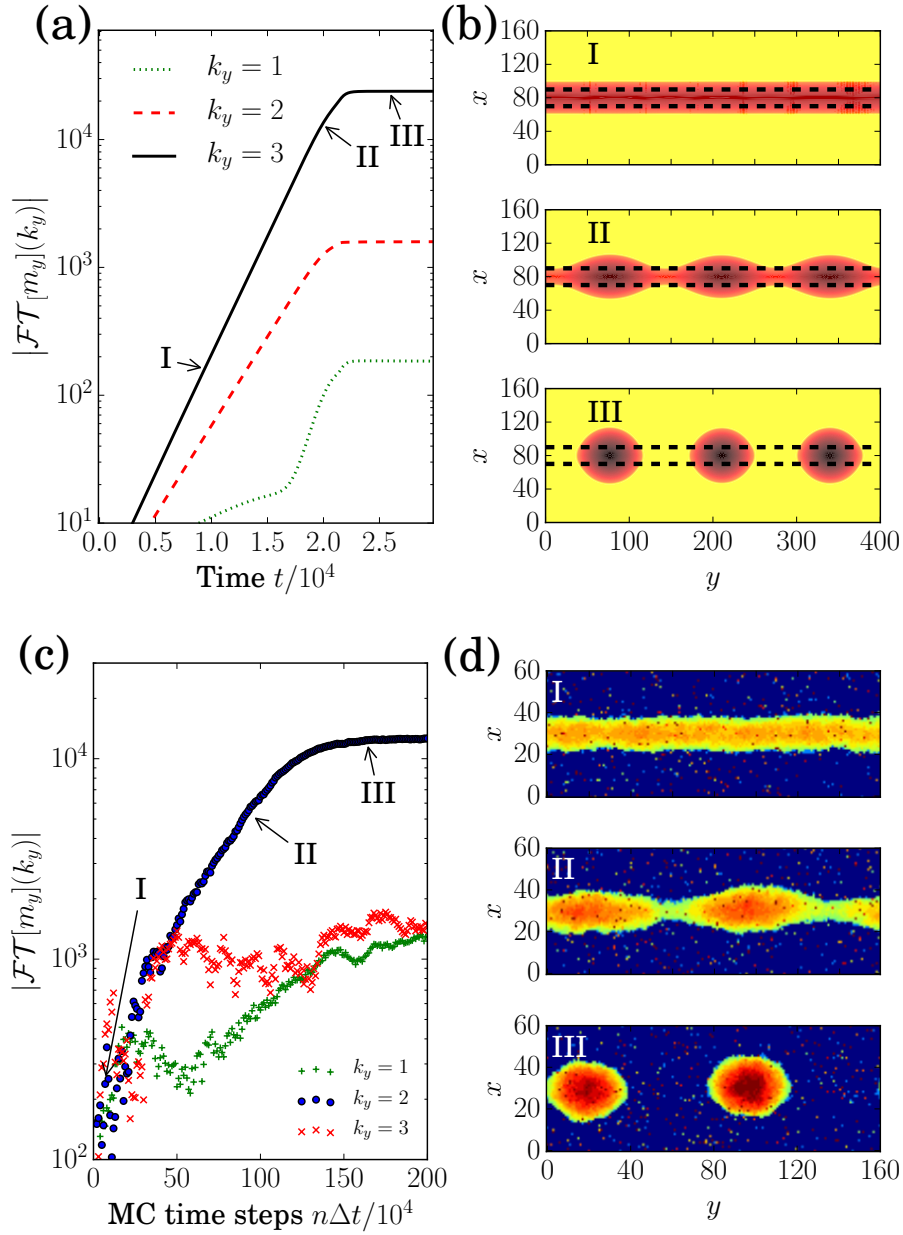


Figure 4.14: (a), (c): Time evolution of the first three Fourier modes for the transversal instability of a single ridge on a prepattern stripe as obtained by simulations of the thin-film equation and by KMC modeling, respectively. (b), (d): Corresponding snapshots, illustrating the unexpected extend of the exponential growth regime for the dominant mode in both modeling approaches. Figure reproduced from [TBH⁺17].

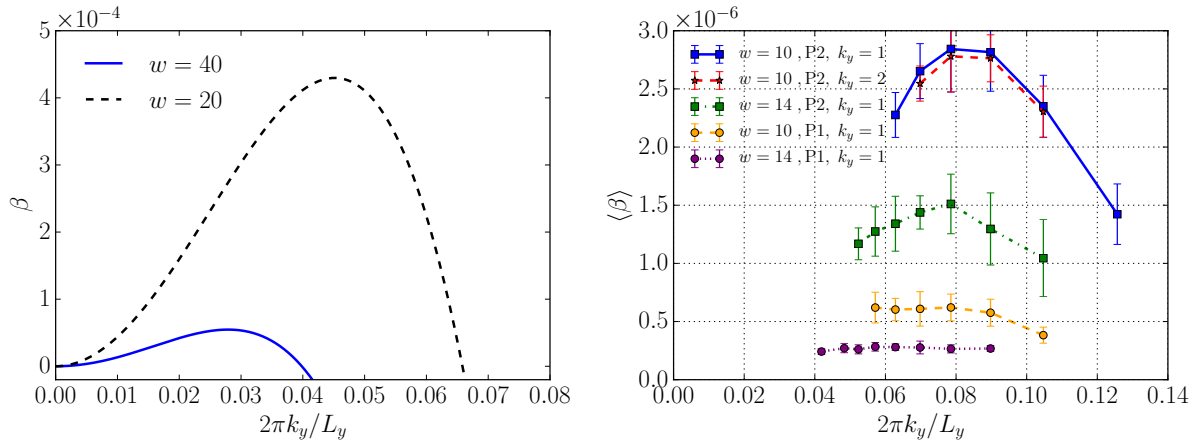


Figure 4.15: Qualitative comparison of dispersion relations for the transversal Plateau-Rayleigh type instability of ridges in the framework of the thin-film equation (left) and KMC modeling (right) for two different stripe geometries. For the KMC model, the measured dispersion relations are shown for the two different parameter sets P1 and P2, which basically correspond to different temperatures of the system. (Cf. [TBH⁺17])

4.4 Towards a Mapping of KMC to Effective Interface Models

The reduction of a stochastic KMC model to a deterministic effective interface model (similar to the thin-film equation) necessitates two fundamental steps. First, the stochastic model has to be mapped to a deterministic model for the average density field.

Subsequently, a dimensional reduction of the mean field model has to be performed in order to obtain for a $N = 1, 2$ dimensional substrate a model for the local effective interface height of the liquid film from a theory for the density on the $(N + 1)$ -dimensional domain. This coarse graining steps can first be attempted for static solutions in a statistical sense but a similar coarse graining for the dynamical evolution of the mean interface building on the results for the static solutions is finally desirable. In the present section, we first discuss a novel numerical approach for the dynamical coarse graining of density dependent energy functional which encode static solutions of the density field and demonstrate it on a simple *density functional theory* (DFT) relevant for the mean field description of the KMC model. Here, our presentation follows along the lines of [BTA⁺17]. Additionally, we shortly discuss a possible direction for the mapping of a mean field dynamical equation to a dimensionally reduced effective interface model based on numerical results from the reduction of the energy functional.

4.4.1 Thermodynamics of a Liquid Film on a Solid Substrate – The Binding Potential

In order to introduce the general concepts of the binding potential and of the *effective interface Hamiltonian*, we first consider a general thermodynamic model for the density of a single particle type in a fixed two-dimensional domain A . The generally nonhomogeneous equilibrium density field $\varrho(\mathbf{x})$ is obtained in the canonical ensemble by minimization of a *Helmholtz free energy* $\mathcal{F}_H[\varrho]$ with a mass constraint implemented by a Lagrangian multiplier μ . With respect to the density field, the equilibrium state is given by a minimum of the thermodynamic grand potential [HTA14]

$$\Omega_{2D} = \mathcal{F}_H - \mu \int_A d\mathbf{x} \varrho(\mathbf{x}). \quad (4.25)$$

Even without interaction with a solid wall, for adequate Helmholtz free energies \mathcal{F}_H , below a critical temperature T_c , it is energetically favorable for the system to form domains of low density ϱ_g (gas phase) and high density ϱ_l (liquid phase) as compared to a single phase of homogeneous average density in the whole domain. The value of the chemical potential for this case of phase separation is denoted by $\mu = \mu_{\text{coex}}$. More specifically, we now consider a rectangular domain $A = [0, L_x] \times [0, L_z]$ and introduce a solid wall to the system at $z = 0$ with interaction energies such that the wall is (partially) wetting i.e., a liquid film or droplet is formed in contact with the wall. In order to describe the system energetically based solely on the shape of the liquid-gas interface along the wall, it is convenient to define two energetic quantities based on one dimensional density profiles with or without the solid wall. Since the overall chemical potential is fixed at $\mu \approx \mu_{\text{coex}}$, for sufficiently large domains A , all 1D profiles have to be considered at this particular value of the chemical potential.

To quantify the energetic contribution of the liquid-gas interface itself, we define the liquid-gas *surface tension* γ_{lg} as:

$$\gamma_{\text{lg}} = \Omega[\varrho^{\text{lg}}] - \Omega[\varrho^{\text{g}}], \quad (4.26)$$

where $\Omega[\varrho^{\text{lg}}]$ is the effective 1D grand potential of a 1D density profile with a liquid-gas interface. Accordingly, $\Omega[\varrho^{\text{g}}]$ is the 1D grand potential⁹ of a constant density profile with density ϱ_{g} . Considering now a system with a solid wall interacting with the particles, a pure liquid phase in contact with the wall described by the density field ϱ^{sl} approaching ϱ_1 for large enough values of z is deformed close to the wall. The energy associated with this deformation can be quantified by the solid liquid surface tension γ_{sl} . Finally, for a density profile $\varrho^{\text{slg}}[h]$ exhibiting a liquid-gas interface at a given effective distance h from the wall, an *excess grand potential* contribution due to the finite value of h is given by the so called binding potential or effective interface potential $g(h)$ [BTA⁺17, HTA15]:

$$g(h) = \Omega[\varrho^{\text{slg}}[h]] - \Omega[\varrho^{\text{sl}}] - \gamma_{\text{lg}}, \quad (4.27)$$

and approaches zero as $h \rightarrow \infty$. Note that the effective distance of the liquid-gas interface from the wall can be described more generally by the so-called adsorption Γ which is related to an effective film height by:

$$\Gamma := \int_0^{L_z} \varrho^{\text{slg}}(x) - \varrho_{\text{g}} \, dz =: (\varrho_1 - \varrho_{\text{g}})h. \quad (4.28)$$

After defining these energetic quantities based on 1D density profiles, the minimization of the grand potential in the domain A can now approximately be reduced to a minimization of the following *effective interface Hamiltonian* \mathcal{F}_{IH} with respect to the height function $h(x)$ [BTA⁺17, HTA15]:

$$\mathcal{F}_{\text{IH}}[h] = \int g(h) + \xi \gamma_{\text{lg}} \, dx, \quad (4.29)$$

where $\xi = \sqrt{1 + (\partial_x h)^2} \approx 1 + (\partial_x h)^2/2$ is the interface metric which can be approximated by the latter expression for a long wave geometry (cf. §3.2.2). While the surface tension γ_{lg} can be readily extracted (numerically) from 1D equilibrium density profiles, the calculation of the binding potential g is not straightforward. It necessitates the calculation of density profiles with a specified adsorption. In general, such profiles are nonequilibrium states in 1D. However, the adsorption constraint can not be enforced by a Lagrangian multiplier, since this would alter the chemical potential which has to be kept at $\mu = \mu_{\text{coex}}$ to ensure that the density profiles approach ϱ_{g} for $z \rightarrow \infty$.

In the following subsections, we first introduce a simple lattice gas DFT which can be employed for the mean field description of the KMC model described in §4.3.1. Subsequently, we exemplarily demonstrate on this DFT a novel numerical approach to the calculation of the binding potential based on the *nudged elastic band algorithm*.

4.4.2 Lattice Gas DFT

The equilibrium mean field density corresponding to KMC models such as the one introduced and employed in §4.3 can be described for sufficiently large systems (i.e., particle numbers) by thermodynamic mean field theories. We formulate a modified version of the Hamiltonian

⁹ Here, $\Omega[\varrho^{\text{g}}] = \Omega[\varrho^{\text{l}}]$, since we consider the system at coexistence

(4.21) with arbitrary particle-particle interactions via ϵ_{ij} and including interaction with a homogeneous substrate through the wall potential V_i :

$$H = -\frac{1}{2} \sum_{i,j} \epsilon_{ij} p_i p_j + \sum_i V_i p_i. \quad (4.30)$$

One of the simplest mean field approximations of the grand potential corresponding to (4.30) can be derived based on the *Gibbs-Bogoliubov inequality* [HTA14] and reads

$$\Omega_{2D}[\{\varrho_i\}] = k_B T \sum_{i,j} [\varrho_i \ln(\varrho_i) + (1 - \varrho_i) \ln(1 - \varrho_i)] - \frac{1}{2} \sum_i \sum_j \epsilon_{ij} \varrho_i \varrho_j + \sum_i \varrho_i (V_i - \mu). \quad (4.31)$$

Here, ϵ_{ij} and V_i are directly inherited from the KMC Hamiltonian (4.30). In FIG. 4.16, a solution of an iterative minimization of the lattice DFT grand potential is shown¹⁰. The solution corresponds to a droplet formed at the wall, while the inset shows a 1D density profile at a fixed position on the wall.

In the following, for the calculation of the binding potential in a finite domain, we employ an effective 1D version of (4.31) with nearest neighbor particle-particle interaction as well as an effective self-interaction of the particles, stemming from the mapping of the 2D grand potential:

$$\Omega[\{\varrho_i\}] = k_B T \sum_{i=1}^{L_z} [\varrho_i \ln(\varrho_i) + (1 - \varrho_i) \ln(1 - \varrho_i)] - \frac{1}{2} \sum_{i=1}^{L_z} \sum_{j=1}^{L_z} \epsilon_{ij} \varrho_i \varrho_j + \sum_{i=1}^{L_z} \varrho_i (V_i - \mu). \quad (4.32)$$

The wall potential is set as

$$V_i = -\epsilon_\omega i^{-3} \quad \text{for } i \geq 1, \quad (4.33)$$

i.e., it is algebraically decaying throughout the whole domain and at ($i = 0$) it is formally set to $V_0 = \infty$ which accounts for the solid wall. In the following, we adopt the notation $\boldsymbol{\varrho} = \{\varrho_i\}$ for a discrete density profile specified by the densities ϱ_i on all lattice sites $i = 1, \dots, L_z$.

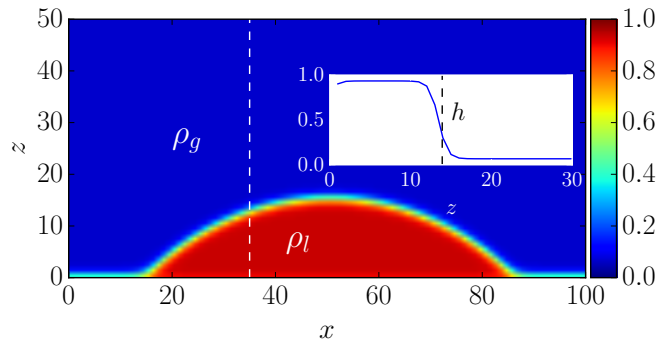


Figure 4.16: Equilibrium of the 2D lattice DFT (4.31) corresponding to a droplet of liquid density ρ_l in contact with the wall. As an inset, we show a density profile obtained from a cross section of the droplet. (Cf. [BTA⁺17])

¹⁰ See [HTA14] for details on the minimization algorithm.

4.4.3 NEB Approach to the Calculation of Binding Potentials¹¹

For the DFT grand potential (4.32), a numerical method for the calculation of the binding potential is outlined in [HTA15, HTA17]. This method is based on an iterative Picard optimization with the introduction of a self consistent fictitious potential enforcing a constraint on the adsorption $\Gamma = \sum_{i=1}^{L_z} (\varrho_i - \varrho_g)$ without altering the chemical potential, i.e., such that the calculated profiles approach ϱ_g far away from the wall. Furthermore, in [HTA15], this method is used to calculate fit functions with corresponding fit parameters and finally to successfully compare profiles calculated from an effective interface Hamiltonian (4.29) with density fields of corresponding droplets obtained as minima of the 2D lattice gas DFT.

We now present a novel approach to the calculation of the binding potential which we then substantiate by comparing its results to the results obtained from the aforementioned fictitious potential approach.

The method is based on the so-called *nudged elastic band* (NEB) algorithm which was also previously employed in [Lut08] for the calculation of energy barriers for droplet nucleation from an oversaturated gas phase. In the case of droplet nucleation, a constraint on the mass of the droplet similar to the adsorption constraint has to be satisfied without altering the chemical potential (cf. [Lut08, AE11]). The NEB algorithm is a double-ended chain of states method [HJJ02, HJ00] which can be used to calculate saddle points and steepest descent paths on a free energy landscape. The basic idea is to fix two end points on the free energy landscape and then initialize an adequate number of intermediate points.

Upon an independent minimization of each intermediate point, the chain of points would obviously collapse to minima of the free energy. The idea of the NEB algorithm is to inhibit the optimization process from having this effect by introducing artificial elastic forces between the points of the chain, parallel to the latter. Let us specify the algorithm as implemented for our specific problem: In our case, obviously the grand potential function $\Omega[\varrho]$ at coexistence ($\mu = \mu_{\text{coex}}$) acts as the free energy landscape. The chain of points which is subject to optimization is a sequence of density profiles $\varrho^I = \{\varrho_i^I\}$, $I = 1 \dots P$. Adequate end points for our purpose are a homogeneous density field ϱ^g at the bulk gas phase and a profile ϱ^{wl} of the liquid phase in contact with the wall which can be calculated as a minimum of Ω and corresponds to the maximal adsorption in our finite system:

$$\varrho^0 = \varrho^g, \text{ with } \varrho_i^g = \varrho_g \text{ for } i = 1, \dots, L_z, \Gamma(\varrho^g) = 0, \quad (4.34)$$

$$\varrho^{P+1} = \varrho^{\text{wl}}, \text{ with } \Omega[\varrho^{\text{wl}}] \text{ and } \varrho_{L_z}^{\text{wl}} \approx \varrho_l. \quad (4.35)$$

We now have to formulate initial guesses for the intermediate points of the chain corresponding to profiles with increasing adsorption. Here, we choose a set of profiles $\{\varrho^I\}$ with:

$$\varrho_i^I = \frac{1}{2}(\varrho_g - \varrho_l)\tanh(i\sigma - a_I L_z) + \frac{1}{2}, \quad (4.36)$$

where the parameter a_I controls the position of the interface and thus the adsorption.

Finally, in order to define the elastic forces acting between two adjacent profiles, a measure of

¹¹The work presented in this subsection is a collaboration with Oleg Buller (Institute for Physical Chemistry, Münster) and Andrew Archer (Loughborough University). The numerical approach based on the NEB algorithm has been elaborated in close cooperation and the implementation has been conducted based on a code written by O. Buller. The results for the fictitious potential approach have been obtained based on a code made available by A. J. Archer. The work was jointly published in [BTA⁺17], our presentation in this subsection follows along the lines of [BTA⁺17].

distance has to be formulated. In our case, we set the elastic forces proportional to the metric induced by the the L^2 norm:

$$\left| \left(\boldsymbol{q}^{I+1} - \boldsymbol{q}^I \right) \right|^2 = \sum_{i=1}^{L_z} \left(q_i^{I+1} - q_i^I \right)^2. \quad (4.37)$$

An appropriate minimization algorithm is now employed on the overall force vector for all points of the chain. For each point, the force vector consists of the parallel component of the elastic force and the perpendicular component of the force resulting from the free energy landscape (i.e., from the grand potential). The overall force vector reads [BTA⁺17]:

$$\boldsymbol{F}_{\text{NEB}} = \{ \boldsymbol{F}_{\text{NEB}}^1, \dots, \boldsymbol{F}_{\text{NEB}}^P \}, \text{ with } \boldsymbol{F}_{\text{NEB}}^I = \underline{\boldsymbol{P}}^{\parallel} \boldsymbol{F}_{\text{elastic}}^I + \underline{\boldsymbol{P}}^{\perp} \boldsymbol{F}_{\text{FE}}^I. \quad (4.38)$$

Here, $\underline{\boldsymbol{P}}^{\parallel}$ and $\underline{\boldsymbol{P}}^{\perp}$ are projection operators onto the direction parallel and perpendicular to the chain, respectively. For details concerning the formulation of the elastic force we refer to [HJ00]. As minimization algorithm, geometric optimization with direct inversion in the interactive subspace (GDIIS) is used (cf. [CP84]).

Note that the NEB algorithm is in fact an algorithm for the calculation of *steepest descent paths* (SDPs) connecting minima and the equally calculated saddle points. The concept of a SDP depends on a metric specified for the formulation of the gradients but the saddle points and minima found by the algorithm are nonetheless independent of the metric. Here, we calculate the steepest descent path with respect to the Euklclidean metric. While we have no formal

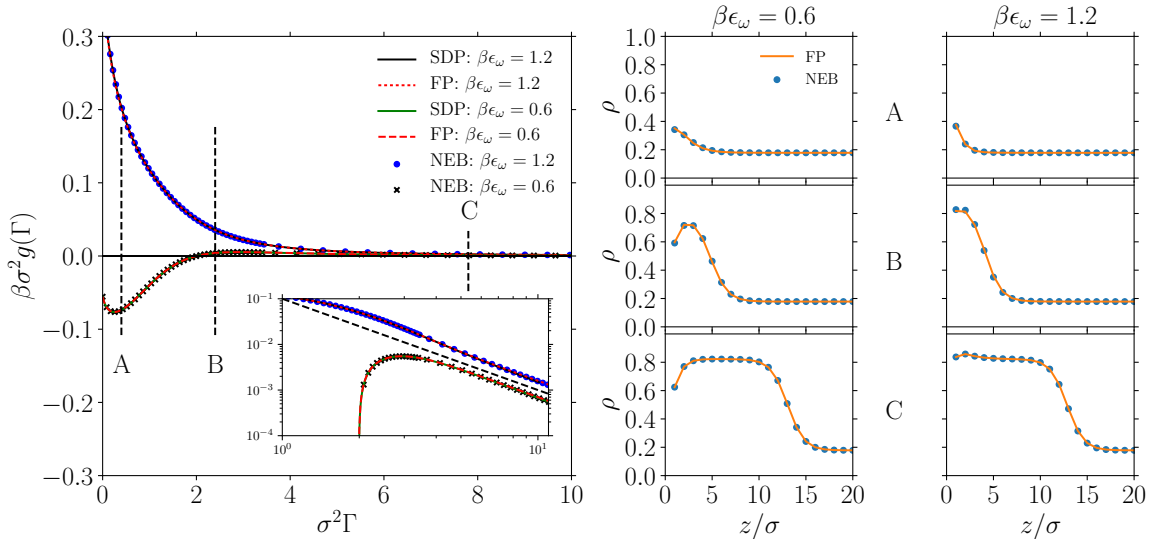


Figure 4.17: Left: Comparison of binding potentials as functions of the adsorption Γ calculated by the NEB algorithm, the fictitious potential approach [HTA15] and the steepest descent paths obtained from a simulation of the pseudo-dynamics (4.39). Right: Comparison of density profiles obtained from the NEB and the fictitious potential approach at given specific values of the adsorption Γ denoted by A, B, C in the left plot. All results for two different wall interaction energies are in excellent agreement. Figure reproduced from [BTA⁺17].

argument why this specific SDP gives the best approximation for the constrained minima at a specified adsorption, the result can be very successfully compared to binding potentials obtained for the same system employing the aforementioned fictitious potential approach. Thus, the obtained binding potentials can be successfully employed for the construction of interface profiles in good agreement with the DFT. In FIG. 4.17, we show a comparison between results obtained by the NEB algorithm described above and the fictitious potential approach for two different values of the wall interaction energy ϵ_ω . The binding energies and the profiles (exemplarily shown on the right of FIG. 4.17) are in excellent agreement for both algorithms. In addition, in order to verify whether the NEB algorithm correctly give the SDP, we show the SDPs as calculated by pseudo-dynamics given by

$$\dot{\boldsymbol{\rho}} = -\frac{\partial\Omega}{\partial\boldsymbol{\rho}}, \quad (4.39)$$

starting from the profiles $\boldsymbol{\rho}^0$ and for the case of $\beta\epsilon_\omega = 0.6$ equally from the saddle point with small perturbations to each direction.

4.4.4 Outlook: Mapping of Mean Field Dynamics to Effective Interface Dynamics

To coarse-grain the average dynamics of the liquid-gas interface of a KMC model as the one described in §4.3, the first step (which is already rather tedious) is to formulate adequate mean field dynamical equations. Approaches for lattice gas dynamics are discussed in [PB92, Mon08, GPDM03, ART10, CSA17a]. In [Mon08, GPDM03, CSA17a] ODEs for the evolution of the density on a lattice are considered, and it is pointed out in [Mon08] that the there derived ODEs correspond to a finite difference version of a Cahn-Hilliard- (or DDFT-) type dynamics. In [PB92] and also in [ART10], a continuum PDE for the density field is employed. The general form of a continuum theory for the dynamics of the density field $\varrho(\mathbf{x})$ (excluding the density on the solid wall) found in the aforementioned literature reads:

$$\partial_t \varrho(\mathbf{x}, t) = \nabla \cdot \left(M(\varrho) \nabla \frac{\delta\Omega[\varrho]}{\delta\varrho(\mathbf{x}, t)} \right). \quad (4.40)$$

In particular, in [PB92], this equation is supplemented by no-flux boundary conditions at the wall as well as a boundary condition corresponding to an Allen-Cahn type relaxation of a surface energy functional.

Given an adequate evolution equation of the form (4.40), the next step would be to extract a coarse-grained (dimensionally-reduced) equation for the adsorption Γ . It is reasonable to assume that the evolution equation for the adsorption is – as the evolution equation for the density field – of variational form (cf. §2.1) and reads

$$\frac{\delta\mathcal{R}_{\text{EI}}}{\delta\dot{\Gamma}(x, t)} = 0, \text{ where } \mathcal{R}_{\text{EI}} = \mathcal{D}_{\text{EI}}[\Gamma, \dot{\Gamma}] + \frac{d}{dt}\mathcal{F}_{\text{IH}}[\Gamma]. \quad (4.41)$$

The underlying assumption for a reduction to the form (4.41), where \mathcal{F}_{IH} is the effective interface Hamiltonian (4.29), is that the density field $\varrho(x, z)$ at each fixed position x relaxes fast enough to the constrained extrema $\varrho_\Gamma(z)$ for given adsorptions $\Gamma(x)$, i.e.

$$\varrho(\mathbf{x}, t) = \varrho_{\Gamma(x, t)}(z). \quad (4.42)$$

While in the previous subsection, we outlined how the binding potential (and thus the effective interface Hamiltonian in general) can be obtained numerically from the energetics dependent on the density field, the discussion of reduced dissipation functionals $\mathcal{D}_{\text{EI}}[\Gamma, \dot{\Gamma}]$ is out of the scope of the present work. In general, a numerical calculation building on the numerically known density profiles $\varrho_{\Gamma}(z)$ which are obtained as a byproduct of the calculation of the binding potential employing the NEB algorithm, might be promising. However, we emphasize once again that the calculation of stability *limits* as done for the transversal stability of ridges in the context of the thin-film equation does not necessitate the knowledge of the dissipation.

4.5 Conclusion

In the first part of the present chapter, motivated by the deposition experiments discussed in [WDW⁺11, WC12], we have investigated a thin-film model for chemically prepatterned substrates. More precisely, the stability of liquid ridges on prepattern stripes has been discussed in terms of NTS, as well as numerical and semi-analytical calculations. For a single ridge, we have highlighted the fact that the transversal stability limit is fully encoded in the energetics of corresponding 1D steady state solutions (cf. [MRD08]). The stability of two adjacent stripes has been investigated and dynamical effects of diffusion outrunning transversal instabilities have been discussed, motivated by experimental findings in [WDW⁺11]. As illustrated by the snapshot FIG. 4.18, the established numerical techniques using DUNE-PDELab [BBD⁺08a, BBD⁺08b, BHM10] allow large-scale simulations of the dynamics of liquids on prepatterned substrates. An interesting topic for future work on the thin-film equation with heterogeneous binding potential is the investigation of 2D steady states on different prepattern geometries. Here, one solution type which is also found experimentally in [WC12] corresponds to bridge states between adjacent prepattern stripes (cf. FIG. 4.18). The numerical study of such 2D steady states using 2D continuation techniques (cf. [EGU⁺18]) and focusing on interfacial energies seems promising.

In the second part of the chapter, a systematic but qualitative comparison of time simulations of the thin-film equation and simulations based on a KMC algorithm has been shown. Here, we have mainly focussed on a qualitative comparison of transversal dispersion relations, which are in good agreement and also qualitatively agree with a phenomenon seen in the corresponding experiments (i.e., larger dominant wavelength for broader prepattern stripes). Finally, we have presented a novel numerical approach for the extraction of effective wetting energies from a DFT and discussed a possible outline for the coarse-graining of KMC dynamics.

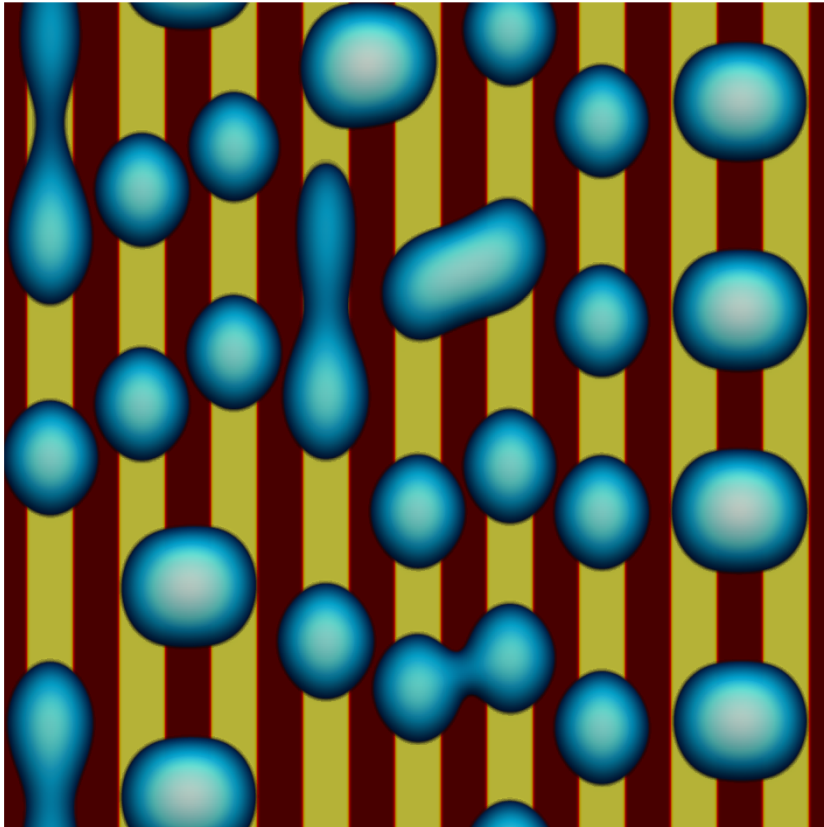


Figure 4.18: Rendered snapshot of a NTS of (4.3) with the prestructure function (more wettable areas are visualized in gold) as employed in §4.3, modeling nine prepatter stripes on a domain of size $L_x \times L_y = 600 \times 600$ with a mean film height $h_0 = 4.0$ and a contrast $\rho = 0.2$. Note the “bridge” structures formed subsequently to the transversal instability of the ridges due to coarsening of the bulges.

5 Propagation of Instabilities

The instabilities shown in the numerical simulations in the previous chapter (e.g., FIG. 4.4 or FIG. 4.8) are triggered by perturbations which are extended throughout the entire simulation domain. Thus, the Plateau-Rayleigh instabilities correspond to a more or less simultaneous breakup of the entire initial ridge into bulges. In contrast, in the first part of the present chapter, we investigate a different mode of instability growth, namely the spreading of linear instabilities starting at *localized* perturbations. With other words, from the local perturbations, the instabilities *propagate* into the linearly unstable steady state. For linearly unstable flat liquid films and liquid ridges on homogeneous substrates, we show that NTS suggest that this propagation corresponds to the well-known class of so-called *pulled fronts*, which denotes front propagations into *linearly unstable* states where the front speed is dictated by the linear dispersion relation [Van03].

In the second part of the chapter, we introduce a more complex geometry, namely the so-called *dip-coating* geometry, where a substrate is pulled from a liquid bath at an externally imposed fixed speed. For this geometry, we discuss a solution type mentioned in [Wil16] but otherwise not yet described in the literature. This solution type corresponds to the time-periodic formation of droplets (or ridges in 2D) close to the meniscus. A boundary of the parameter space region where the latter occurs is related to the aforementioned results for pulled fronts in liquid films.

5.1 Pulled Fronts in Free Surface Liquids

5.1.1 Pulled Patterning Fronts

The propagation of fronts into linearly unstable states is a well-investigated phenomenon in nonlinear physics, in particular in the theory of pattern formation. For an extensive review of the matter, we refer to [Van03]. Here, following [Pis06], we shortly outline the basic idea behind the concept of the pulled fronts:

Consider an appropriate nonlinear PDE for the spatio-temporal evolution of an order parameter $u(x, t)$ that has a solution consisting of a linearly unstable steady homogeneous state $u_{\text{us}}(x) = u_{\text{us}}$.¹

$$\partial_t u(x, t) = \mathcal{N}[u], \text{ with } \mathcal{N}[u_{\text{us}}] = 0. \quad (5.1)$$

More specifically, consider a front propagating into the unstable state u_{us} with a constant propagation velocity c . At the *leading edge* of the front, the deviation $v(x) = u(x) - u_{\text{us}}$ is sufficiently small to consider the linearization of (5.1) about the steady state:

$$\partial_t v = \mathfrak{L}[u_{\text{us}}]v \xrightarrow{\xi:=x-ct} v(\xi, t) = \int_{-\infty}^{\infty} dk \tilde{v}(k) e^{ik\xi + (ick + \omega(k))t}, \quad (5.2)$$

¹ For simplicity, we consider a 1D geometry. The operator \mathcal{N} is a, in general, nonlinear differential operator.

where the dispersion relation $\omega(k)$ obtained from the linearized operator \mathfrak{L} is given by

$$\mathfrak{L}[u_{\text{us}}]e^{ikx} = \omega(k)e^{ikx}. \quad (5.3)$$

We now assume that the Fourier integral solution in the comoving frame (5.2) can be rewritten as a path integral in the complex plane (using Cauchy's integral theorem [BSMM12]) passing through a saddle point of the argument of the exponential function in (5.2). The integral can then be approximated by the contribution at the saddle point only and we obtain for large times t :

$$v \sim e^{ik\xi + (ick^* + \omega(k^*))t}, \text{ where } \left. \frac{d}{dk}(-ck + i\omega(k)) \right|_{k=k^*} = 0. \quad (5.4)$$

We impose that the leading edge solution does not grow or decay in the comoving frame for long times and thus $\Re(ick^* + \omega(k^*)) = 0$. Together with the condition that the speed is real valued, the following set of equations defining the saddle point k^* and the speed c is obtained [DL83, Pis06]:

$$\frac{\Re(\omega(k^*))}{\Im(k^*)} = c, \quad (5.5)$$

$$\Re(\omega'(k^*)) = 0, \quad (5.6)$$

$$-\Im(\omega'(k^*)) = c. \quad (5.7)$$

The above calculation, which is also termed *marginal stability analysis* (MSA) was first employed by A.N. Kolmogorov et al. for the calculation of propagation velocity of a front described by the so-called *Fisher equation* [KPP37]. For this case, the state invading the unstable homogeneous steady state corresponds to a stable homogeneous state. The analysis can however also be employed for pattern forming fronts invading unstable states as shown in [DL83]. A very similar analysis is even possible for unstable periodic states which are invaded by an instability front (cf. [Sch17]). Note also that depending on initial perturbations, different fronts than the discussed pulled fronts may be selected by the system in question. The propagation speed is then larger than the speed obtained from the marginal stability analysis².

For the case of pattern forming systems, not only the speed of propagation but also the wavenumber of the patterns selected behind the moving front is of interest. In order to obtain an expression for this wavenumber, following along the lines of the argumentation given in [DL83], we once again inspect the asymptotic leading edge solution (5.4). In the comoving frame, this corresponds to a wave with wavenumber k^* and angular frequency $\Omega := \Re(k^*)c + \Im(\omega(k^*))$. The angular frequency can be interpreted as the flux of the nodes of the wave.³ This flux should be conserved during the transition of the solution from the leading edge to the stationary pattern left behind the front. Still in the comoving frame of the leading edge, the flux of nodes of the stationary pattern with wavenumber k_s behind the front is given by ck_s . Thus, the wavenumber k_s reads

$$k_s = \frac{\Omega}{c} = \Re(k^*) + \frac{\Im(\omega(k^*))}{c}. \quad (5.8)$$

² For a thorough discussion of this matter, we refer once again to [Van03] and references therein.

³ Consider a plane wave of the form $e^{ikx + i\Omega t}$. Then, the phase velocity is given by $c = \Omega/k$ and interpreting the wavenumber as the "density of nodes", a flux J of nodes can be written as $J = kc = \Omega$.

5.1.2 Marginal Stability Analysis for Flat Linearly Unstable Liquid Films⁴

Let us now consider instability fronts invading linearly unstable homogeneous solutions of (3.38). In order to calculate the linear asymptotic speed of invasion and the wavelength of the pattern selected behind the front given by (5.5)-(5.7) and (5.8)⁵, respectively, we first need to compute the dispersion relation for a linearization of (3.38) about the flat film. Inserting the ansatz

$$h(x, t) = h_0 + \varepsilon e^{ikx + \omega(k)t}, \quad (5.9)$$

into (3.38) and dropping all terms of $\mathcal{O}(\varepsilon^2)$, we obtain the dispersion relation

$$\omega(k) = -M(h_0) \left(k^4 + (f''(h_0) + g) k^2 \right) + ik\alpha g M'(h_0). \quad (5.10)$$

We now define

$$\xi := -(f''(h_0) + g); \quad \eta := g \frac{\alpha M'(h_0)}{M(h_0)}; \quad \tilde{\omega}(k) := \frac{\omega(k)}{M(h_0)} = \xi k^2 - k^4 + \eta ik. \quad (5.11)$$

The rescaled dispersion relation $\tilde{\omega}(k)$ and its derivative $\tilde{\omega}'(k)$ evaluated at complex wavenumbers $k = kr + ik_i$ (note that the derivative is taken considering $\tilde{\omega}(k)$ as a real function) read:

$$\omega(k) = \xi \left(k_r^2 + 2k_i k_r i - k_i^2 \right) - \left[k_r^4 + k_i^4 - 6k_i^2 k_r^2 + i \left(4k_i k_r^3 - 4k_i^3 k_r \right) \right] + i\eta k_r - \eta k_i \quad (5.12)$$

$$\omega'(k) = 2 \left[\xi (k_r + ik_i) - 2 \left(k_r^3 + i3k_r^2 k_i - 3k_i^2 k_r - ik_i^3 \right) \right] + i\eta. \quad (5.13)$$

Here and in the following, the real and imaginary part of the variables are denoted by indices r and i , respectively. From (5.6), we obtain

$$k_r^2 = \frac{\xi}{2} + 3k_i^2 \quad (5.14)$$

and from (5.7) follows

$$\frac{\tilde{c}k_i}{2} = -(k_i^2 \xi - 6k_r^2 k_i^2 + 2k_i^4) - \frac{k_i \eta}{2}, \quad (5.15)$$

whereas (5.5) gives

$$\frac{\tilde{c}k_i}{2} = \frac{1}{2} \left((\xi k_r^2 - \xi k_i^2) - (k_r^4 + k_i^4 - 6k_i^2 k_r^2) - \eta k_i \right). \quad (5.16)$$

For the linearly unstable regime ($\xi > 0$), (5.14)-(5.16) can then be combined to result in

$$k_i^2 = \frac{\xi}{24} (\sqrt{7} - 1) \quad (5.17)$$

$$\tilde{c}_\pm = -\Im(\tilde{\omega}'(k)) = -\eta \pm \frac{2}{3} \xi^{\frac{3}{2}} \left((2 + \sqrt{7}) \sqrt{\frac{\sqrt{7} - 1}{6}} \right). \quad (5.18)$$

The two different propagation velocities correspond to up- and downstream propagating fronts. Note that for the case $\eta = 0$, i.e., for a non-inclined substrate, we recover the symmetry $|c_+| = |c_-|$.

⁴ Recently, after the work presented in this subsection and the subsequent one had been carried out, in [LCK18], a marginal stability analysis for a thin-film model has been published.

⁵ A very similar calculation for the Cahn-Hilliard equation is outlined in [Köp11].

5.1.3 Propagating Spinodal Dewetting Fronts Without Gravity⁶

As a first system, let us consider the front propagation into flat liquid films without gravity effects (3.36). The general results from the previous subsection are readily applied to (3.36) by setting $g = 0$ such that, in particular, $\eta = 0$. As binding potential, we employ (3.37). Then, films of all heights $h > h_{\text{lim}} \approx 1.25$ are linearly unstable, as can be seen by inspection of the dispersion relation, where a band of unstable wavenumbers $0 < k < k_c = \sqrt{-f''(h_0)}$ is obtained as long as $f''(h_0) < 0$ (cf. (5.10)). The breakup of liquid films due to a linear instability induced by the binding potential is termed *spinodal dewetting* [Mit93, Pis04, HJM⁺98] due to its mathematical similarity to the *spinodal decomposition* of a binary mixture modeled by the Cahn-Hilliard equation [Cah65]. A plot of the binding potential and its first derivative can be found in FIG. 5.1.

We consider NTS of (3.36) in 1D with flat films of varying heights h_0 which on the left side fall off smoothly but sufficiently sharp to an equilibrium adsorption layer as initial conditions. The NTS are performed on a domain of size $L = 6000$ for $h_0 < 4.3$ and $L = 10000$ for $h_0 \geq 4.3$. No-flux boundary conditions are chosen on both sides. In order to obtain a "clean" propagation front and to prevent breakup of the film ahead of the front due to numerical noise, we furthermore impose a "freezing front" ahead of the instability front with a speed well above the propagation speed of the latter.⁷ A similar numerical approach was pursued in [Sch17] in a study of instability fronts in the Cahn-Hilliard system. For small film heights

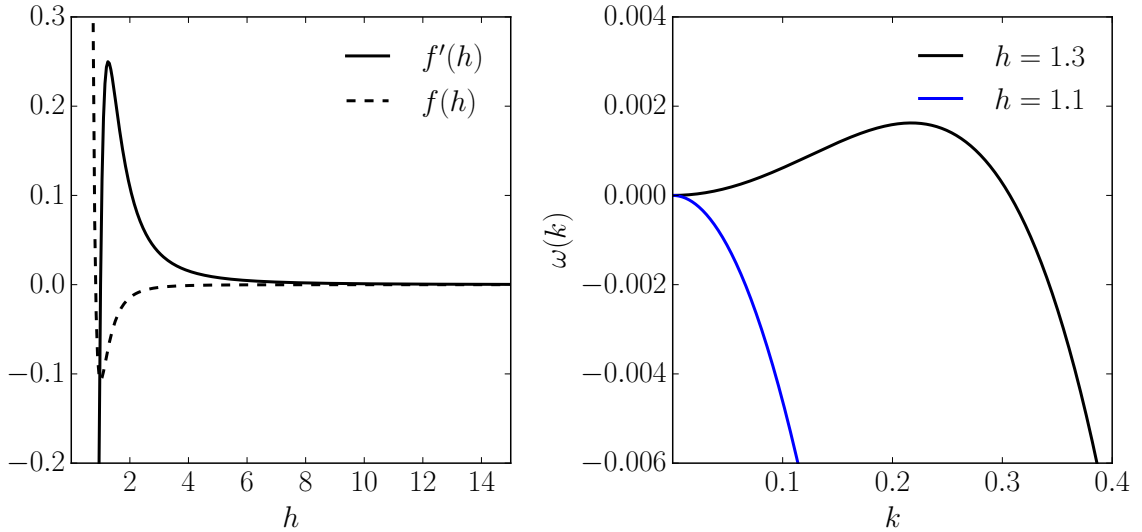


Figure 5.1: Left: Binding potential $f(h)$ (3.37) and its first derivative $f'(h)$. Flat films of all heights h above the height where $f'(h)$ is maximal are linearly unstable. Right: Dispersion relation for flat films described by (3.36) for two different film heights as given in the legend (below and above the stability limit).

⁶ Recently, after the work presented in this subsection had been carried out, in [LCK18], a marginal stability analysis for a thin-film model has been published.

⁷ I.e., we impose a location x_f moving at a given speed c_{freeze} such that $\partial_t h(x > x_f) := 0$. By comparison of different speeds of the freezing front, it is ensured that the dynamics of the instability front are not altered by this simulation technique.

$1.5 \leq h_0 < 1.9$, we find instability fronts leaving behind a regular pattern of droplets of equal height, which are unstable w.r.t. coarsening. In fact, for some NTS, a coarsening front can be seen following the initial instability front. These coarsening fronts are studied in detail in [Sch17] for the Cahn-Hilliard equation, where the speed of the coarsening fronts is calculated by an extension of the arguments shown in §5.1.1 towards linearly unstable *periodic* states. At $h_0 \approx 3.0$, this secondary instability grows already close to the leading edge of the front, such that after initial propagation leaving behind droplets of equal size, quasi-instantaneous coarsening behind the front sets in and more involved periodic droplet patterns are produced (cf. FIG. 5.2). Investigating instability fronts for larger film heights, a variety of periodic patterns can be found. However, independently of the complexity of the deposition pattern left behind by the front, all fronts found in the NTS propagate to a very good approximation with a constant speed after an initial transient phase. This can be conveniently seen in the space-time plots shown in FIG. 5.2.

We proceed to quantify the results from NTS concerning the propagation speed and the deposition patterns. In order to extract the propagation speed as a function of film height, we define a level set of the film height sufficiently close to the initial film height h_0 and numerically track the maximal position at which this height is reached (for fronts propagating towards $x \rightarrow \infty$). The speed is then obtained by a linear fit of these positions over time. As can be seen in FIG. 5.2 and FIG. 5.3, the thus obtained propagation speed in the NTS is in excellent agreement with the analytically calculated speed (5.18) for $g = 0$ (after rescaling). This agreement is independent of the type of deposition pattern behind the front, i.e., a secondary front is locked into the primary one.

In FIG. 5.4, we show results of the analysis of deposition patterns produced in the final stages of the NTS on the limited simulation domain considered. These results are compared to predictions based on (5.8) where no phase slip is assumed during the transition of the periodic patterns from the leading edge to the area behind the front. The results shown in FIG. 5.4 have to be taken with a grain of salt, since a further relaxation of the deposition behavior for larger simulation domains and thus longer propagation times is to be assumed and could be found exemplarily in extended simulations. Nevertheless, lacking a theoretical prediction of the stable deposition mode, the results obtained for the limited simulation domain are shown as an overview of patterning modes which are possibly transient. In particular, in FIG. 5.4, for different values of h_0 , we display the different maximal heights of the deposited droplets⁸ found within one spatial period as well as the wavelength of the latter. The wavelength of the deposition pattern can be directly compared to the wavelength $\lambda_s = \frac{2\pi}{k_s}$, where k_s is given by (5.8) with the respective results obtained in §5.1.2.

The height of the droplets can be compared to results from numerical continuation of the steady state droplets (cf. §4.2.3), where the system size is set as the wavelength λ_s and the mean mass m is adapted as $m = h_0$. For both the wavelength and the droplet height, we find excellent agreement for small film height $h_0 < 2.9$, where the secondary instability of the deposition mode is not present. For film heights above the limit $h_0 \approx 3.0$, the wavelength extracted from the NTS seems rather unsteady, which can probably be attributed to the analysis of possibly transient propagation modes. In fact, a certain trend of the wavelength re-approaching the wavelength λ_s for increasing film heights might be inferred.

⁸ As already mentioned, the deposited droplets are unstable to coarsening through diffusive fluxes, therefore we show the height of the droplets within one of the first spatial period shortly after the passage of the front.

This deserves further investigation, possibly in combination with theoretical predictions concerning the stability of the patterning modes. The deviation of the maximal height of the droplets from the results assuming no phase slip is found to increase monotonically. This might be a possible route towards a more common dewetting front which is found for linearly stable films and corresponds to a so-called dewetting rim [SHJ01], i.e., a droplet (or ridge) invading the film without detaching from it.

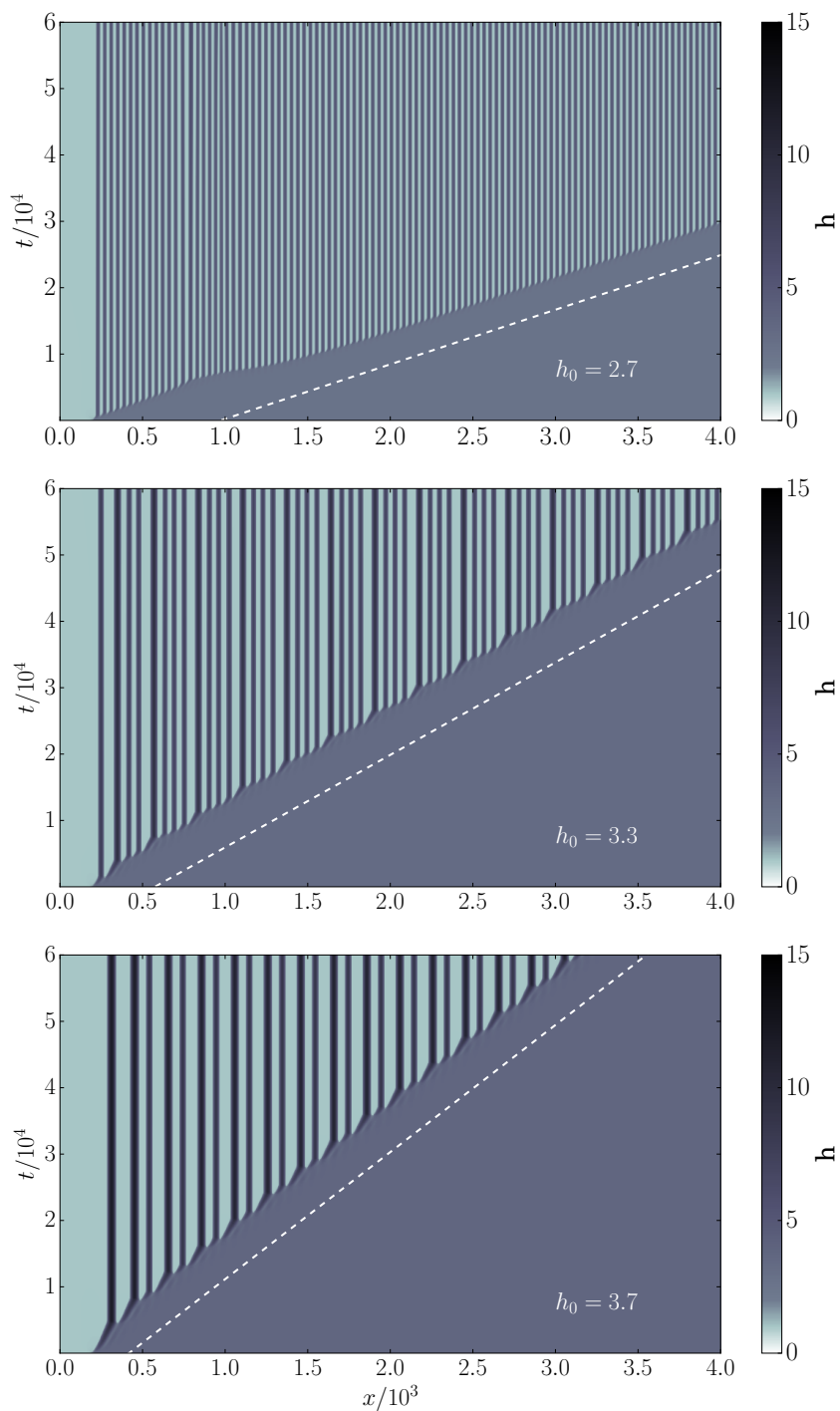


Figure 5.2: Space-time plots showing NTS of instability fronts found for (3.36) and three different heights h_0 of the initial flat film. Note the nontrivial periodic pattern of droplets obtained for the two larger film heights. The dashed lines indicate the speed obtained analytically from the marginal stability analysis (5.18).

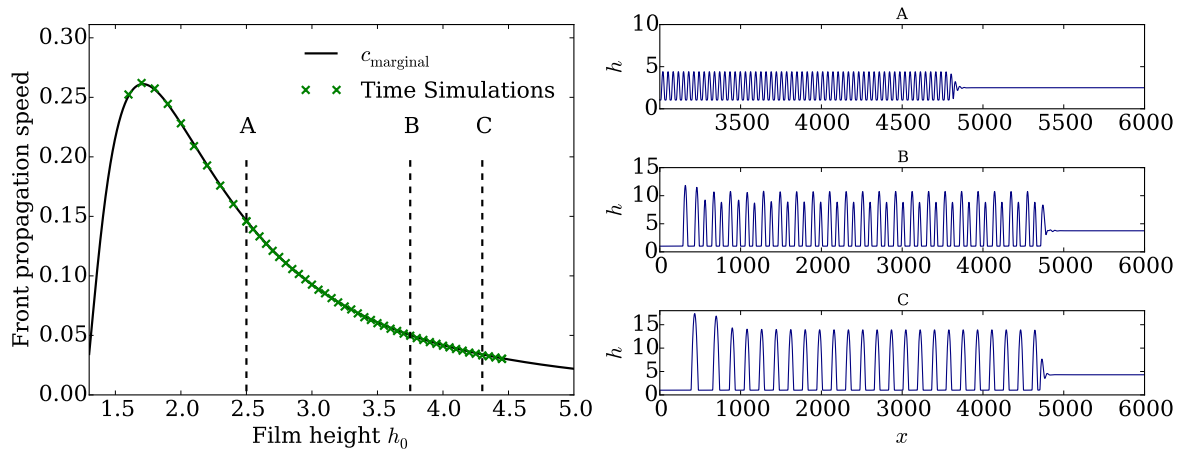


Figure 5.3: Left: Speed of propagation of spinodal fronts (solid line) calculated by the marginal stability analysis outlined in §5.1.2 as a function of the height of the initial flat film in comparison to propagation speeds as obtained from NTS of (3.36) (crosses). Note that the two speeds are in excellent agreement independent of the complexity of the deposition pattern behind the leading edge of the front. Right: Snapshots of NTS showing the different droplet patterns left behind the propagating front for different film heights.

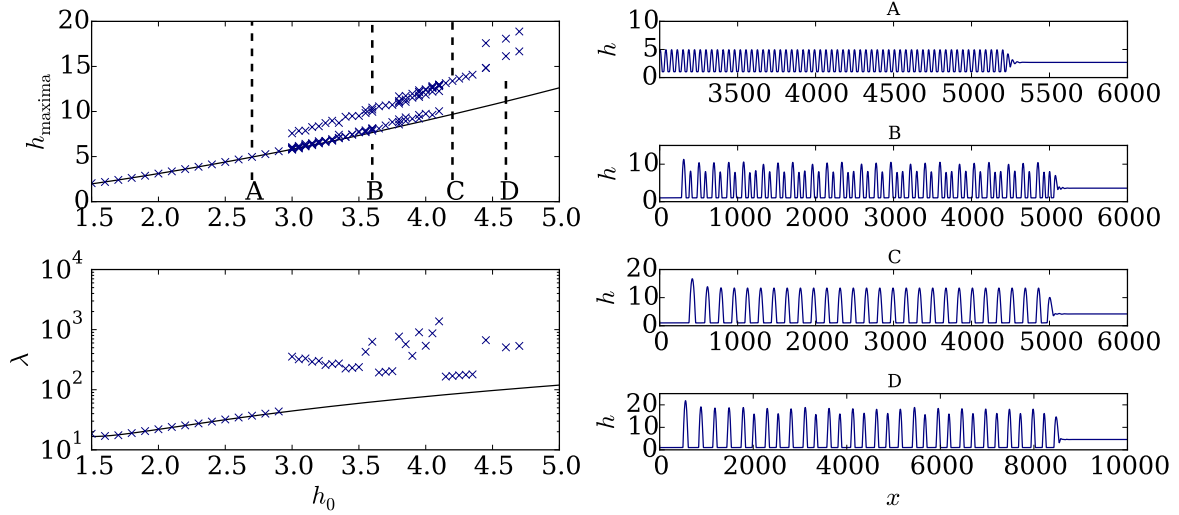


Figure 5.4: Analysis of the droplet patterns deposited behind the leading edge of the spinodal fronts as obtained from NTS. Left top: All maximal heights of different droplets deposited behind the front as obtained shortly after deposition (all droplet patterns are unstable to coarsening). The solid line denotes the height of droplets calculated by numerical continuation of steady states of (3.36) assuming the wavelength of the deposition pattern obtained from (5.8) as the domain size and a droplet mass as imposed by the conservation of the mass after passage of the instability front. Left bottom: Wavelength of the deposition pattern as seen in the late stages of the propagation on the considered domain size. The solid line shows the wavelength calculated by (5.8). At about $h_0 = 3.0$, a secondary instability close to the leading edge is found, such that coarsening directly at the instability front leads to periodic droplet patterns of greater wavelength than the one predicted by (5.8) assuming no phase slip. Note that we show results obtained from NTS on a finite domain, for the cases of $h_0 > 3.0$, a further relaxation of the propagation behavior is to be expected for longer simulations of the propagating front. Right: Snapshots of NTS at initial film heights indicated by the vertical dashed lines in the top left panel.

5.1.4 Propagating Plateau-Rayleigh Instabilities

In a small series of publications [GNPS96, PZGS98, PG97], R. Goldstein et al. investigated the propagation of Plateau-Rayleigh instabilities for liquids and vesicles of initially cylindrical geometry. As a result, they found that some instability fronts associated with the pinching of droplets from the unstable initial cylindrical structure can be described by a marginal stability analysis (cf. §5.1.1). Here, we show results of a similar analysis applied to the propagation of the Plateau-Rayleigh instability of liquid ridges on substrates, an instability which has already been discussed in §4.2.4. While corresponding experiments with macroscopic liquid ridges [GDGG07] (cf. FIG. 5.5) were investigated in terms of simulation and linear stability analysis, e.g., in [DGK09, DG16], to our best knowledge, the instability has not yet been discussed theoretically as a front propagation problem in the spirit of the works of R. Goldstein et al..

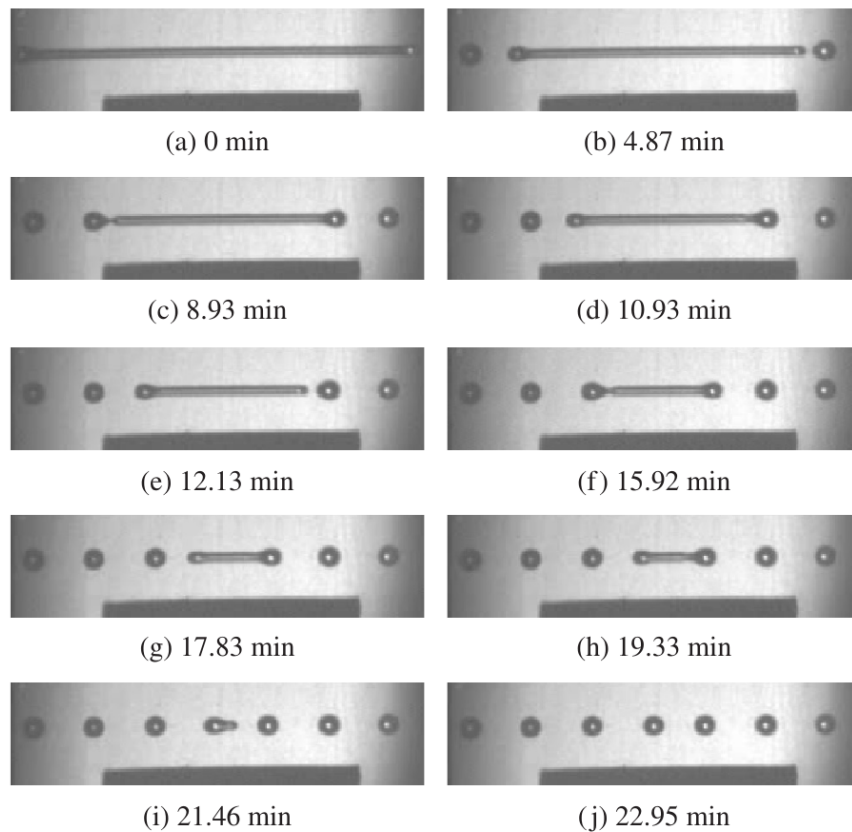


Figure 5.5: Optical images showing snapshots from the time evolution of a propagating Plateau-Rayleigh instability of a strip of silicon oil on a coated substrate. An equidistant array of droplets results from the instability. Modeling and theoretical considerations for the experiment can be found in [DGK09, DG16]. Picture reproduced with permission from [GDGG07], © Europhysics Letters Association.

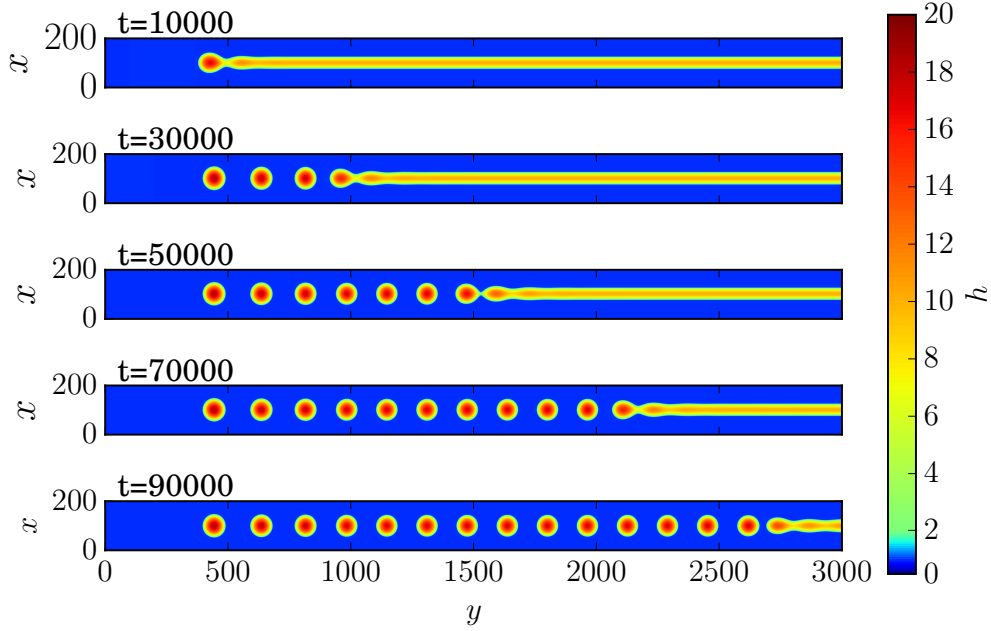


Figure 5.6: Snapshots of a NTS in 2D of (3.36) on a domain of size $[0, 200] \times [0, 3000]$. The initial ridge is based on a steady 1D drop solution obtained by numerical continuation. We subject the initial ridge to a localized perturbation at one end. The instability propagates at approximately constant speed and leaves a well ordered array of droplets behind.

As in §4.2.4, we consider a liquid ridge, where the cross-section is given by a 1D steady state $h_0(x)$ of (4.3). Analogously to the argumentation in §5.1.1, we now focus on the leading edge of a propagating front, such that the deviation from the unstable initial state can be described by a linearization of (4.3). The resulting deviation $\tilde{h}(\mathbf{x}, t) = h(\mathbf{x}, t) - h_0(x)$ from the initial state can be expressed as (cf. (5.2))

$$\tilde{h}(\mathbf{x}, t) = \int dk h_1(x, k) e^{iky + \omega(k)t}, \quad (5.19)$$

where $\omega(k)$ is obtained from $\omega(k)h_1 = \mathfrak{L}[h_0, k]h_1$, with the linearized operator given by (4.16) and h_1 being the dominant unstable eigenmode. Following the same reasoning as in §5.1.1, we thus obtain (5.5)-(5.7) as constituting equations for the propagation speed, where now the dispersion relation is the one for the Plateau-Rayleigh instability as discussed in §4.2.4. To solve (5.5)-(5.7), an analytical expression for $\omega(k)$ is needed, whereas in §4.2.4, we only obtained the dispersion relation numerically. In the following, we focus on ridges on homogeneous substrates, however, the subsequent calculation can be readily performed for the case of $\rho \neq 0$ in (4.3). FIG. 5.7 displays two fits of the numerically obtained dispersion relation for an exemplary mean mass $m = 2.0$ of the ridge. While a quartic fit does not perform sufficiently well for our purpose, a hexic fit gives significantly better results. To obtain the hexic fit, we fix the locus and the value of the maximum of $\omega(k)$ as well as the position of the zero crossing as defining quantities for the fit parameters. The latter quantities can be obtained readily by

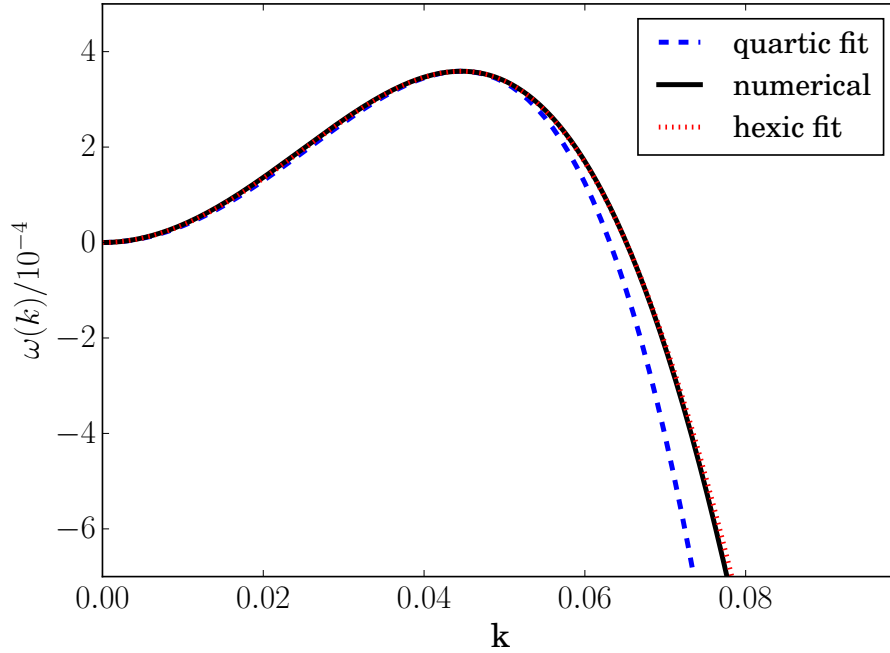


Figure 5.7: Numerically obtained dispersion relation (black solid line) and corresponding fit functions for a liquid ridge of mean mass $m = 2.0$ with a domain size orthogonal to the ridge of $L = 200$ (cf. §4.2.4). Note that while the quartic fit (blue dashed) shows at large wavenumbers a large deviation from the numerical dispersion relation, the hexic fit (red dotted) performs significantly better.

numerical (fold-) continuation of the dispersion relation. Given a dispersion relation which is a hexic polynomial in k , we can now solve (5.5)-(5.7) numerically, with the analytically available solution for a quartic fit as initial guesses. The thus obtained results for the propagation speed of the Plateau-Rayleigh instability can be compared to results from NTS of (3.36).

For the NTS, we initialize ridges with a cross-section obtained from steady state continuation of (3.36). The simulations are performed on a domain of $L_x \times L_y = 200 \times 3000$, on a rectangular grid with $dx = dy = 1.0$. In x -direction, we employ periodic boundary conditions, whereas in y -direction, no-flux boundary conditions are imposed. As for the case of a 1D liquid film discussed in §5.1.3, a localized perturbation is initialized at one side of the structure by a smooth but sufficiently sharp transition to approximately the height of the adsorption layer. In FIG. 5.6, we show snapshots of a simulation of the propagating instability. The front speed is extracted by a level set method analogous to the one described in §5.1.3. The results for the front speed are in good agreement with the prediction of marginal stability analysis, employing the numerical solution of (5.5)-(5.7), assuming that the front is in fact a pulled front (cf. FIG. 5.8). The deviation of the NTS results from the speed obtained from the marginal stability analysis can be mainly attributed to numerical discretization effects. Here, they could not be further reduced, due to the numerically very costly 2D simulations (with large domain size parallel to the ridge).

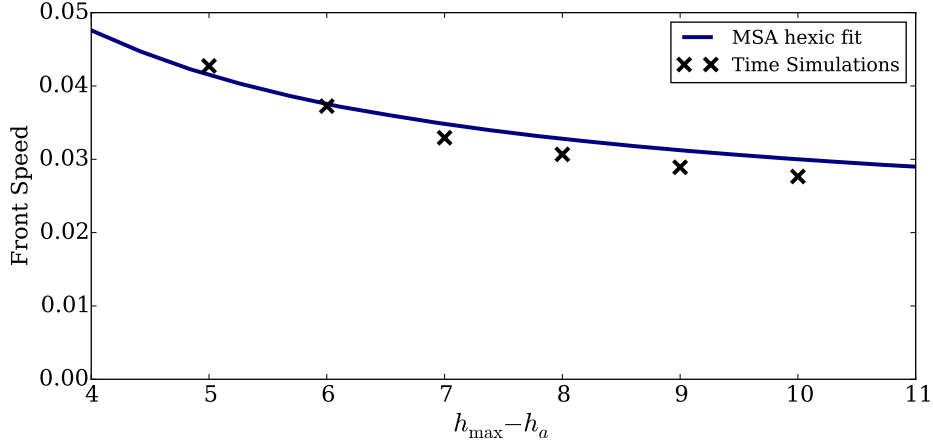


Figure 5.8: Shown is the propagation speed of the Plateau-Rayleigh instability in dependence of ridge height (h_{\max} is the total height of the initial ridge and h_a denotes the adsorption layer height). The solid line shows the marginal stability result obtained as numerical solution of (5.5)-(5.7) employing the hexic fit for the dispersion relation. The crosses indicate speeds obtained from NTS of (3.36) (cf. FIG. 5.6).

5.2 Controlled Dewetting Patterns in a Dip-Coating Geometry⁹

While up to now, we have only considered the behavior of partially wetting liquids on a resting substrate without external forcing (*passive geometry*), in this section, we will discuss results for an *active geometry*, namely the *dip-coating* geometry. In this geometry, a solid substrate is withdrawn from a bath of simple or complex liquid, normally, to coat the substrate with the liquid. A sketch is shown in FIG. 5.9. For complex liquids, such as colloidal suspensions (e.g., [GFS07]) or surfactant laden liquids¹⁰ with volatile solvent (e.g., [CLH⁺07]), recently, dip-coating was employed to obtain periodic deposits on the substrate (for reviews of deposits at moving contact lines, see [HL12, Thi14, Lar14]). In the present section, we discuss deposition of periodic structures that can be found for *simple* partially wetting liquids¹¹ which exhibit spinodal dewetting on sufficiently small time scales at small film heights. The presentation in the present section is very similar to the presentation in [TWGT18].

5.2.1 Steady State Solutions and the Landau–Levich Transition

To model the behavior of a partially wetting liquid in the dip-coating geometry, we consider (3.38) and include an advection term, modeling the withdrawal of the plate with a speed U :

$$\partial_t h(\mathbf{r}, t) = \nabla \cdot \left[M(h) \nabla \left(-\nabla^2 h + f'(h) \right) + \chi(h) \right] - \mathbf{u} \cdot \nabla h, \quad (5.20)$$

$$\text{where } \chi(h) = g \frac{h^3}{3} (\nabla h + \boldsymbol{\alpha}); \quad \mathbf{u} = (U, 0)^T; \quad \boldsymbol{\alpha} = (\alpha, 0)^T; \quad M(h) = \frac{h^3}{3}. \quad (5.21)$$

⁹ The work presented in this section is a collaboration with Markus Wilczek. The NTS for the dip-coating geometry were conducted by M. Wilczek, whereas the analysis based on the MSA was done by W.T.. The continuation results were obtained in close cooperation. The work will be jointly published in [TWGT18].

¹⁰ A well-established dip-coating technique employing surfactants is the so-called *Langmuir–Blodgett transfer*.

¹¹ These periodic structures have first been mentioned in [Wil16].

The following boundary conditions are employed:

$$h = h_0, \nabla h = (-\alpha, 0)^T; \quad \mathbf{n} \cdot \nabla \nabla^2 h = 0 \quad \text{at } x = 0 \quad (5.22)$$

$$\mathbf{n} \cdot \nabla h = 0; \quad \mathbf{n} \cdot \nabla \nabla^2 h = 0 \quad \text{at } x = L_x; \quad \mathbf{n} = (1, 0)^T \quad (5.23)$$

$$h(x, y = 0) = h(x, y = L_y). \quad (5.24)$$

Here, (5.22) models the transition to the liquid bath, assuming an inclination angle α of the plate (cf. FIG. 5.9). Equation (5.23) models an outflux of mass at the r.h.s. boundary of the simulation domain. In y -direction, we assume periodic boundary conditions.

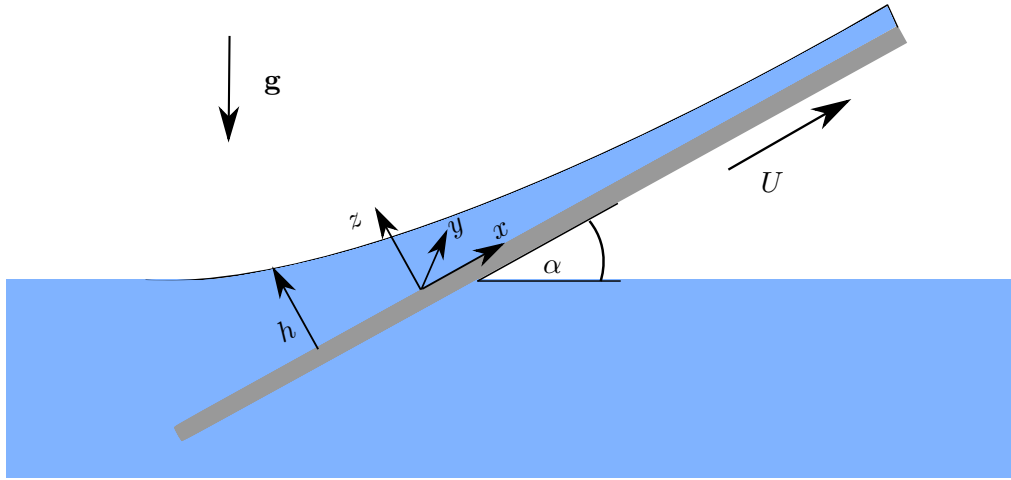


Figure 5.9: Sketch of a dip-coating geometry. A solid plate is withdrawn under an angle α from a liquid bath. Here, the speed of withdrawal U is kept constant and represents a main control parameter.

We start by reviewing steady state solutions of (5.20)-(5.22) in 1D, in dependence of the inclination angle α and the speed of withdrawal U . These solutions have recently been studied in detail in [Gal15]. An overview of steady state solutions obtained by numerical continuation for an inclination angle of $\alpha = 2.0$ is displayed in FIG. 5.10. Here and in the following, the height h_0 in (5.22) is fixed at $h_0 = 100$ and the gravity parameter is chosen as $g = 0.001$. For small values of U , no macroscopic film is transferred onto the plate, which is then only covered by the microscopic adsorption layer (solution V in FIG. 5.10). For large values of U , a homogeneous, macroscopic liquid film, the so-called *Landau-Levich* film, is deposited onto the substrate (solutions I and II in FIG. 5.10). As suggested by the nomenclature, this film deposition was first studied by L.D. Landau and B. Levich [LL42] (and also by B. Derjaguin [Der45]), who derived the following scaling law for the deposited film thickness h_f :

$$h_f \propto U^{2/3}. \quad (5.25)$$

As seen in FIG. 5.11, the scaling of the thickness of the deposited film holds for sufficiently large values of U in the framework of the thin-film model.

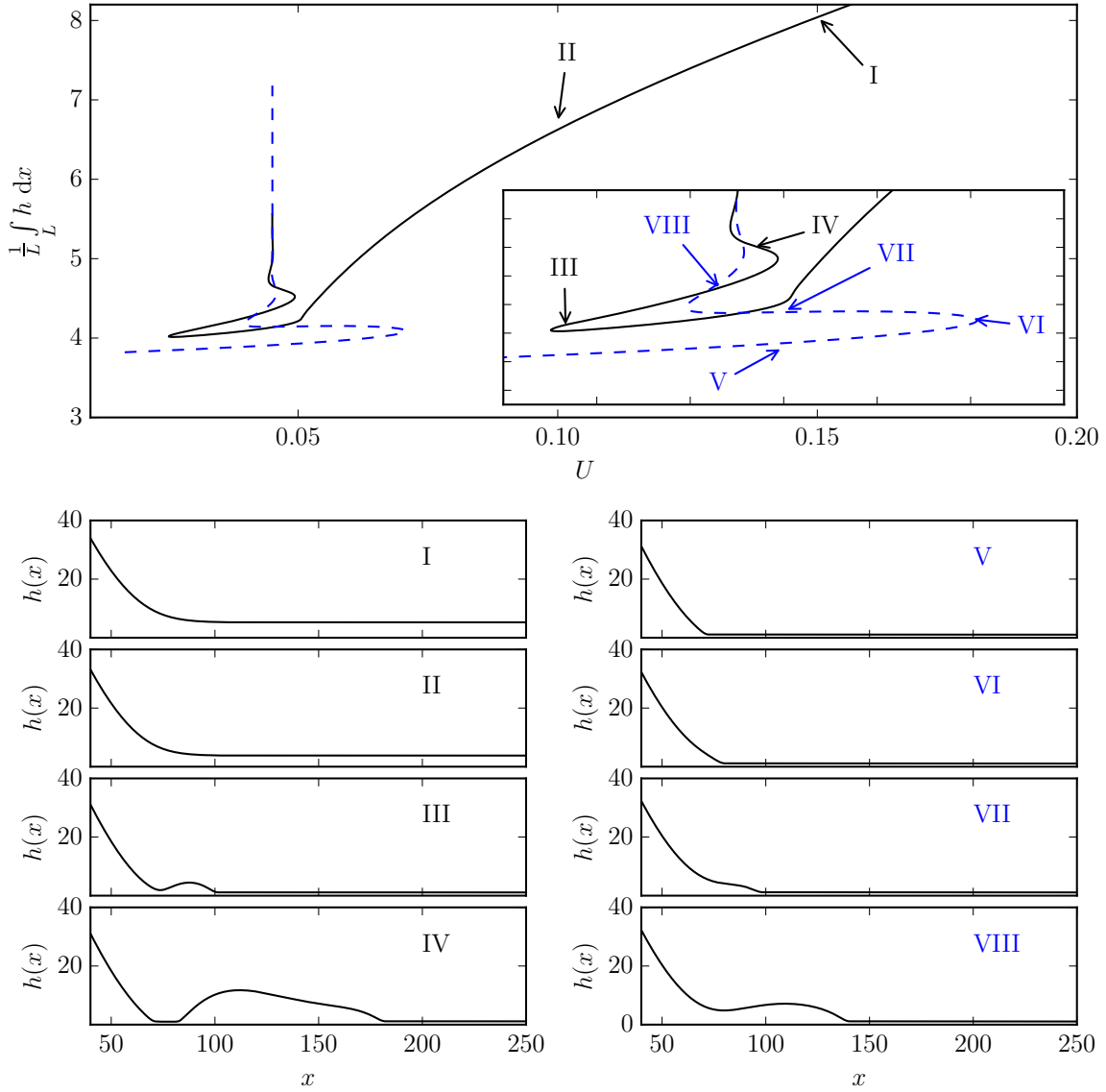


Figure 5.10: Bifurcation diagram for steady state solutions of (5.20)-(5.23). Exemplary solutions are denoted by roman numbers and shown in the lower panels. The solid line corresponds to Landau–Levich type solutions for high values of U (solutions I and II). At lower values of U , this branch becomes a snaking branch of detached foot solutions (solution IV). The dashed line corresponds to a different snaking branch of attached foot solutions (solutions III, IV, cf. [GTLT14, TGT14] for a detailed analysis of this) and becomes a branch of meniscus solutions, where the substrate is only wetted by a thin adsorption layer, for $U \rightarrow 0$ (solutions V, VI).

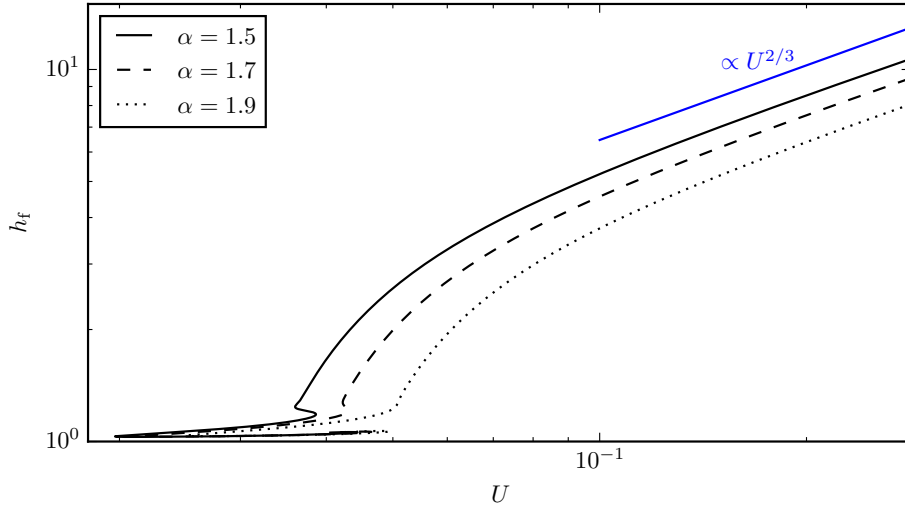


Figure 5.11: Bifurcation diagram obtained by numerical continuation of (5.20)-(5.23), showing the transferred film height h_f (film height at the upper boundary of the domain), in dependence of U for different inclination angles. For all considered values of α , h_f follows the Landau–Levich scaling ((5.25), blue line) for sufficiently large values of U (cf. [GTLT14]).

As the thickness of the deposited film decreases with decreasing speed of withdrawal, the effect of the binding potential (3.37) becomes increasingly important. The binding potential plays a crucial role for the steady state solutions of low mass at values of U above the range of U where no macroscopic film is transferred and below the macroscopic Landau–Levich regime. The transition from the former regime to the latter will be denoted as the Landau–Levich transition in what follows. As shown in FIG. 5.10, for $\alpha = 2.0$, the branch of Landau–Levich solutions is found to be connected to a branch of *detached foot* solutions (e.g., solution IV in FIG. 5.10). Those solutions might be related to transient structures found experimentally in [SZA⁺08], where the speed of withdrawal is increased from below the Landau–Levich transition to values above. In roughly the same range of U , where the snaking branch of detached foot solutions can be computed, a second snaking solution branch is found. This branch corresponds to attached foot solutions (solution VIII in FIG. 5.10) and has recently been discussed theoretically in [TGT14, GTLT14] and previously in [SADF07].

We now proceed to discuss another solution type present at low values of U , namely space-time periodic depositions of droplets (1D) or ridges.

5.2.2 Space-Time Periodic Solutions – Phase Diagram and Analysis

When performing NTS of (5.20)-(5.22), for a certain parameter set, where the speed of withdrawal is not too far away from the Landau–Levich transition, the Landau–Levich solution turns out to be unstable. In these cases, a solution type which has previously not been discussed emerges, namely a solution where the deposition of periodic arrays of droplets (or ridges in 2D) occurs (cf. FIG. 5.12).

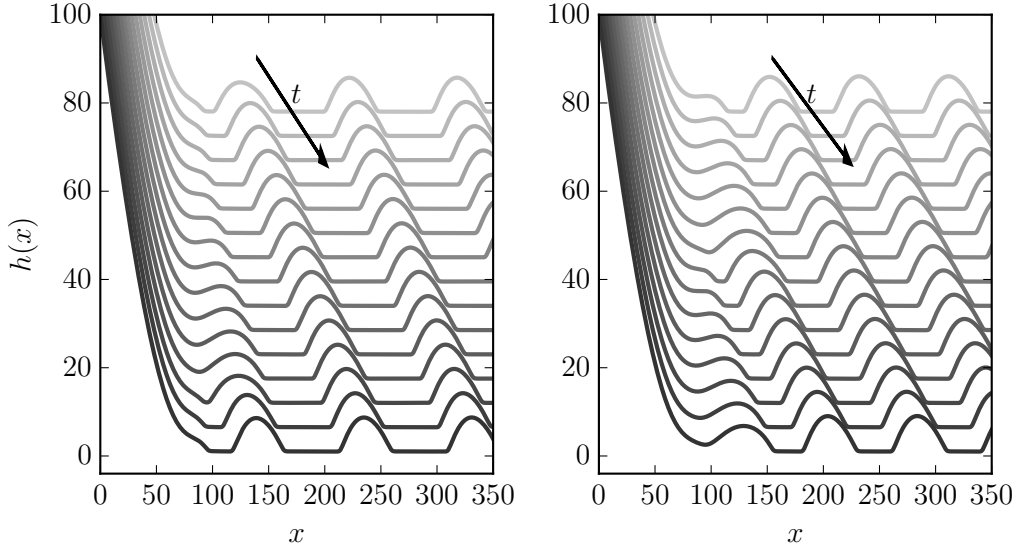


Figure 5.12: Time series representing time-periodic solutions found in NTS of (5.20)-(5.22) for $\alpha = 2.0$, $U = 0.07$ (left), $U = 0.08$ (left) and $h_0 = 100$. The time evolution is visualized by a vertical shift of the snapshots. Droplets are formed periodically close to the meniscus and are subsequently advected away from the latter.

To obtain a phase diagram of the stable solution type shown by the system in dependence of the inclination angle α and the speed U , a parameter study is conducted for two different types of initial conditions. For one, the NTS are initialized by a steady state Landau–Levich solution, for the other, a non steady state sharp meniscus profile is employed. As depicted in FIG. 5.13, the parameter sets for which periodic solutions are found do not completely coincide for the different initial conditions, which implies bistability and hysteresis of the system.

Employing an analysis very similar to an approach described in [KGFT12], we now try to quantify semi-analytically the upper boundary of the periodic deposition domain in terms of the velocity U . It can be observed in the NTS that for values of U above the range where periodic depositions occur, initial perturbances of the monotonic Landau–Levich solution are advected away from the meniscus region. We therefore assume that the upper boundary of the patterning region can be calculated by consideration of the propagation speed of instabilities into the Landau–Levich solutions. More specifically, since the Landau–Levich solutions converge to a flat film far away from the bath, we consider the linear propagation speed of pulled fronts into flat films of height h_f as given by the marginal stability analysis described in §5.1.1 and §5.1.2. Thus, for each speed of withdrawal, a speed $c_- = M(h_f)|\tilde{c}_-|$ of propagation towards the bath can be calculated, where \tilde{c}_- is given by (5.18) and h_f is obtained by numerical continuation (cf. FIG. 5.11). The upper limit of the patterning regime is then obtained by the condition (cf. [KGFT12])

$$g(U) := c_-(h_f(U)) - U = 0, \quad (5.26)$$

i.e., by requiring that the propagation of the dewetting instability matches the speed of withdrawal U . The criterion (5.26) can be solved numerically for U for different inclination angles

α and indeed reproduces very accurately the upper limit of the patterning region found for the initial conditions given by the Landau–Levich solution in the NTS.

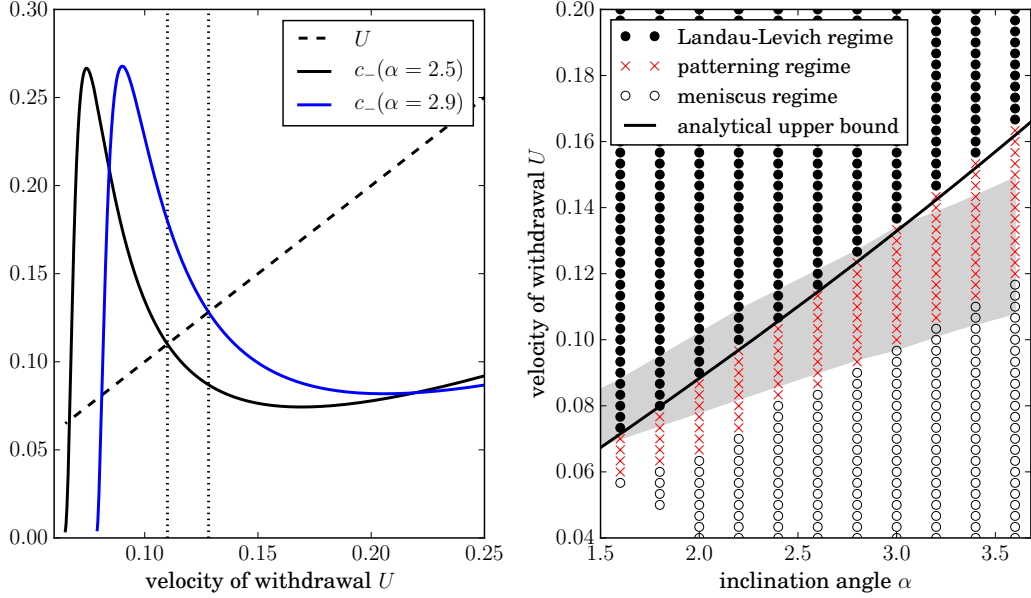


Figure 5.13: Right: Phase diagram obtained by NTS of (5.20)-(5.22), showing solution types in dependence of α and U . Full circles, crosses and hollow circles correspond to flat films solutions, time-periodic solutions and meniscus solutions found when the NTS is initialized by steady state solutions obtained from numerical continuation (cf. FIG. 5.10). The gray shaded area depicts the patterning region when sharp meniscus initial conditions are employed. The solid line shows the relevant zero crossing of $g(U)$ in dependence of α (cf. (5.26)) and reproduces in very good approximation the upper bound of the patterning regime for steady state initial conditions. Left: Visualisation of the criterion (5.26). We show the propagation speed c_- (see (5.18)) of instabilities in the flat Landau–Levich film, calculated from (5.20)-(5.22) in dependence of U for two different values of α .

5.2.3 Numerical Continuation of Time-Periodic Solutions

To explain the bistability found in the NTS and to further explore the solution structure of the system (5.20)-(5.22), we proceed by performing numerical continuation of time-periodic solutions. In order to do so using the tool AUTO-07p, we need to discretize (5.20)-(5.22) in the spatial variable x to get a system of ODEs. While in [LRTT16], such a spatial discretization is effectively done using a fast Fourier transform approach, here the discretization is performed in terms of finite differences.¹² Considering stationary solutions, the resulting bifurcation diagrams obtained are in reasonably good agreement with the corresponding bifurcation diagrams obtained by consideration of the systems (5.20)-(5.22) as a BVP in AUTO-07p. However,

¹² This approach is also followed in [KT14] for a simplified model for periodic depositions in Langmuir–Blodgett transfer.

due to the large number of degrees of freedom, the continuation of the spatially discretized system is computationally very costly and we therefore restrict ourselves to a smaller system size ($L=100$) and a smaller boundary height ($h_0 = 40$) than in §5.2.1 and §5.2.2. A thereby obtained bifurcation diagram including time-periodic solution branches is shown in FIG. 5.14.

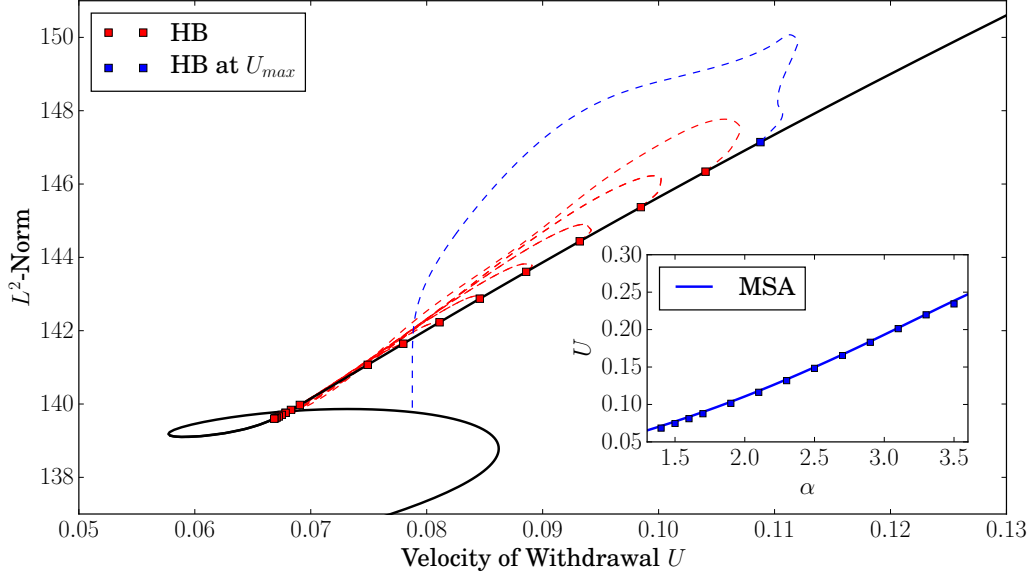


Figure 5.14: Bifurcation diagram of (5.20)-(5.22) for $\alpha = 2.0$, showing the (time-averaged) L^2 -norm of stationary and time-periodic solutions. A sequence of Hopf bifurcations on the Landau–Levich branch (cf. FIG. 5.10) is found which are connected in pairs by branches of time-periodic solutions. The Hopf bifurcation at the highest velocity (U_{max}) gives rise to a branch of time-periodic solutions that terminates in a global bifurcation on the subbranch corresponding to the detached foot solutions. In the inset, we show the very good agreement of the loci of U_{max} for different values of α with the curve corresponding to the marginal stability analysis criterion (5.26) employing the Landau–Levich films heights h_f obtained by continuation of the system as a BVP (cf. FIG. 5.11).

As a solution measure, we use the standard L^2 -norm whenever considering stationary solutions and a time-averaged L^2 -norm for time-periodic solutions. Along the solution branch corresponding to Landau–Levich solutions, a sequence of Hopf bifurcations is detected. The Hopf bifurcation found for the largest value of U is connected to the subbranch of detached foot solutions via a global bifurcation. All the other Hopf bifurcations are connected in pairs by branches of time-periodic solutions. The overall solution structure associated with the time-periodic solutions is very reminiscent of the one found for periodic depositions in Langmuir–Blodgett transfer [KT14], where the authors introduced the term “*harp-like*” bifurcation structure. The Hopf bifurcations at the upper end (i.e., at higher values of U) of the time-periodic solution branches are all subcritical. In FIG. 5.15, we show the dominant time-periodic branch for $\alpha = 2.5$ in more detail and together with snapshots of the solutions.

The subcriticality of the Hopf bifurcation explains the bistability observed in the NTS discussed in §5.2.2. Furthermore, a closer look at the solutions at different sections of the time-periodic

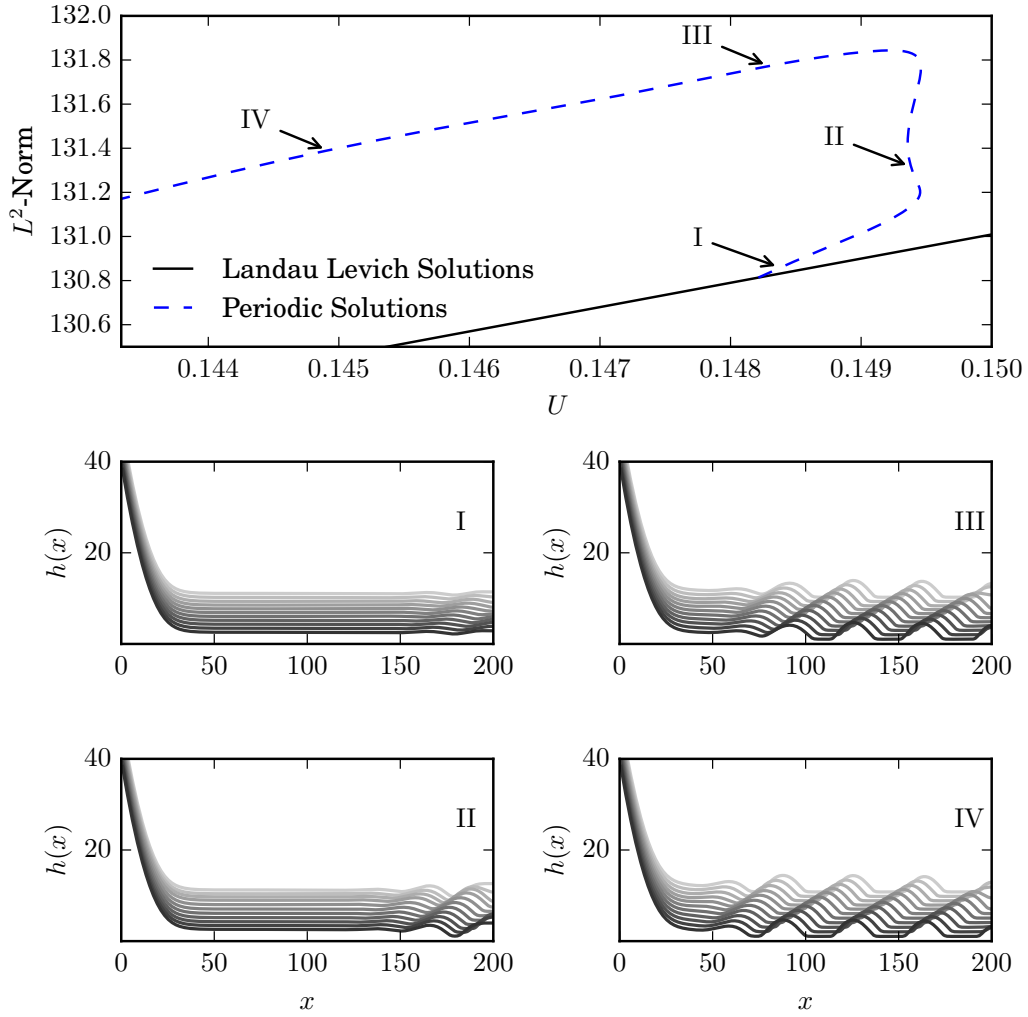


Figure 5.15: Top: Dominant branch of time-periodic solutions of (5.20)-(5.22) for $\alpha = 2.5$ and $h_0 = 40$ found by numerical continuation. Lower panels: Time-series of exemplary solutions denoted by roman numbers. The time evolution is visualized by an increasing vertical shift of the solutions for increasing time. Close to the subcritical Hopf bifurcation, a small oscillation can be seen only at the upper boundary of the domain (solution I). However, for smaller velocities, droplets are formed periodically close to the meniscus (solution IV).

solution branch shown in FIG. 5.15 further elaborates the picture of a pinned instability “trying” to invade the Landau–Levich solution: In very close proximity of the Hopf bifurcation, the time-periodicity of the solution only affects the solutions at the upper end of the simulation domain, while the rest is approximately constant in time. At the upper (r.h.s.) end, small amplitude oscillations about the Landau–Levich film height h_f can be seen. Along the uppermost subbranch of the solution branch in FIG. 5.15, the time-periodic oscillations approach the meniscus further and further. In fact, the loci of the Hopf bifurcations giving rise to the

dominant time-periodic solution branch for different inclination angles α agree remarkably well with the limiting curve calculated from (5.26) with $h_f(U)$ being the upper boundary value obtained from a continuation of (5.20)-(5.22) as a boundary value problem (cf. FIG. 5.11).

5.2.4 2D Simulations

The periodic depositions discussed in the previous subsections correspond to ridges on 2D substrates. While these are, as mentioned in 4.2.4, unstable w.r.t. Plateau-Rayleigh instabilities after deposition, these instabilities may occur on time scales significantly larger than the time-periodicity. An interesting question concerning the behavior of the periodic solutions in 2D is

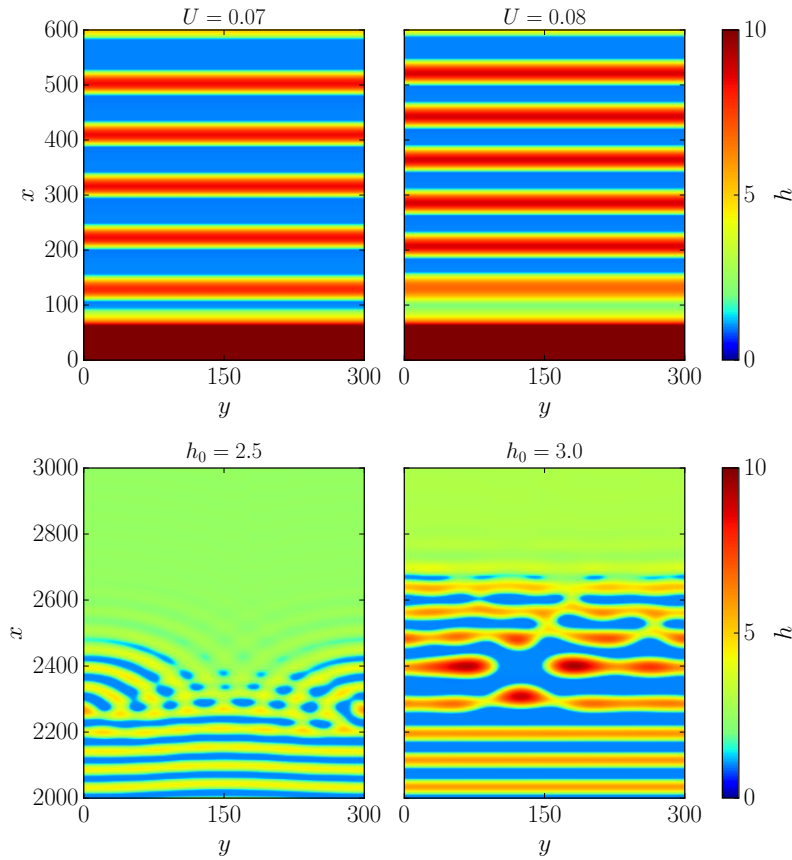


Figure 5.16: Top panels: Snapshots of NTS of (5.20)-(5.22) in 2D after relaxation to a time-periodic state. No transversal instability of the ridges could be seen in the NTS. Bottom panels: Dewetting fronts in 2D obtained from NTS of (5.20)-(5.21) for $\alpha = U = 0$ with no-flux boundary conditions in x -direction and periodic boundary conditions in y -direction. As initial heights of the flat films, we chose approximately the heights h_f corresponding to the velocities in the top panels. After an initial propagation time where nearly translationally invariant stripes are formed, a transversal instability sets in (note that we only show part of the simulation domain).

whether a transversal instability at the onset of the patterning region close to the liquid bath is found. In principle, a transversal stability analysis similar to the one performed in §4.2.4 has to be performed in order to answer this question conclusively. However, such an analysis for time-periodic solutions is rather involved and we thus restrict ourselves to exemplary NTS in 2D in the present work. In FIG. 5.16, we show that on a flat substrate ($\alpha = 0$) without advection, an instability front propagating into a flat film of height $h_f(\alpha = 2.0, U = 0.07, 0.08)$ eventually becomes transversally unstable. However such an instability could not be observed for the dip-coating geometry (cf. FIG. 5.16 for a NTS with $\alpha = 2.0$ and $U = 0.07, 0.08$). We therefore infer that the broken isotropy due to the liquid bath in combination with the advection term leads to a stabilization of the dewetting front in 2D. However, as already mentioned this conjecture is in need of further theoretical foundation.

5.3 Conclusion

In the present chapter, we have discussed the propagation of instabilities for liquid films and ridges, applying the concept of pulled, patterning fronts. For flat films showing spinodal dewetting, the speed of dewetting fronts has been calculated analytically. The patterns behind the front were shown to be rather intricate for certain initial film heights due to secondary instabilities acting directly behind the leading edge of the front. Here, a weakly nonlinear analysis in the comoving frame of the leading edge could give further insight into the structure formation behind the front.

Furthermore, investigating numerically the propagation of Plateau-Rayleigh instabilities of liquid ridges on solid substrates, we have been able to show that the process belongs to the class of fronts discussed in [GNPS96, PZGS98, PG97].

Finally, for the dip-coating geometry, we have discussed a novel solution type of time-periodic depositions. At onset, these solutions can be interpreted as pulled dewetting fronts invading the quasi-flat Landau–Levich layer, while being counteracted by the advection. Here, experimental results concerning this solution type would be of great interest. In order to achieve mesoscopic periodic depositions experimentally, a further destabilization of the liquid on the plate through external fields (e.g., electric fields) might be necessary. In addition, the present work should be of interest for ongoing experimental and theoretical work considering menisci of liquids subjected to surface acoustic waves (SAW) [MM17, AM16] that act in a similar way as the plate-withdrawal in the dip-coating geometry.

6 Statistical and Analytical Coarse Graining

In this chapter, we discuss two inherently different coarse graining procedures, each applied to the modeling of two respective phenomena associated with instabilities of driven liquids on solid substrates.

First, we present a statistical modeling of the coarsening of ensembles of sliding droplets on inclined substrates. Here, we formulate a statistical model, adopting and extending the *Smoluchowski coagulation equation* [Smo16] and employing information obtained from steady state continuation of single sliding droplets. The presentation follows along the lines of our recent work [WTE⁺17].

In the second part of the chapter, we once again return to the notion of the variational principle introduced in §2.1. More specifically, we present two different derivations of an order parameter equation for the depinning of a droplet of partially wetting liquid on a rotating cylinder, where one of the derivations is based on Onsager's variational principle (2.14), whereas the other relies on a projection approach. The resulting order parameter equation is the well-known *Adler equation* [Adl46], a prototype equation for *SNIPER* (saddle-node infinite period) bifurcations [Str14].

6.1 Statistical Description of Sliding Drop Ensembles¹

The coarsening behavior of ensembles of structures like bubbles, droplets or, in general, clusters of particles is a fundamental research topic in soft matter science. Perhaps the best known specific type of coarsening is the so-called *Ostwald ripening* (cf. [Ost97, Ost96]). It can, e.g., be observed in the growth of larger crystals in solution at the expense of smaller ones. The first successful modeling of the diffusive coarsening associated with Ostwald ripening was achieved by I.M. Lifshitz and V.V. Slyozov [LS61] and independently by C. Wagner [Wag61].

Here, we will discuss the coarsening of liquid droplets on an inclined surface. A review of particle-based simulations and statistical modeling of the coarsening of droplets on surfaces can be found in [Mea92a]. In [Mea92b, CRMF89], also ensemble dynamics of liquid droplets on inclined substrates are discussed, focusing on initially pinned droplets and avalanche dynamics. In [GW03, GW09, GW08, GORS09], the authors discuss the coarsening behavior of liquid droplets on flat substrates in terms of coarse graining of the thin-film equation.

Here, we focus on the coarsening behavior of sliding droplets on a solid substrate in absence of *contact line hysteresis* and pinning. Such a system is modeled in terms of (3.38)-(3.39).

¹The work presented in this section is a collaboration with Markus Wilczek and Sebastian Engelkemper. The bifurcation diagrams were calculated by S. Engelkemper, the NTS and its analysis (in terms of extraction of number of droplets and droplet size distribution by KDE) were conducted by M. Wilczek. The formulation and simulation of the statistical model has been done in close cooperation between M. Wilczek and W.T.. The work was jointly published in [WTE⁺17]

6.1.1 Statistical Results from NTS and Connection to Bifurcations of Single Drops

To obtain statistical results for the time evolutions of large ensembles of sliding droplets, large scale NTS of (3.38)-(3.39) with $\chi(h) = g\frac{h^3}{3}\alpha$ are conducted. We consider a domain of $L_x \times L_y = 4000 \times 4000$ with periodic boundary conditions. The simulations performed for different inclination angles are initialized by a flat film of height $h_0 = 2.0$ (which is linearly unstable, cf. (5.10)) and additional uniform noise. After fast initial spinodal breakup of the thin film, the resulting large ensemble of droplets begins to slide. In this early stage, the

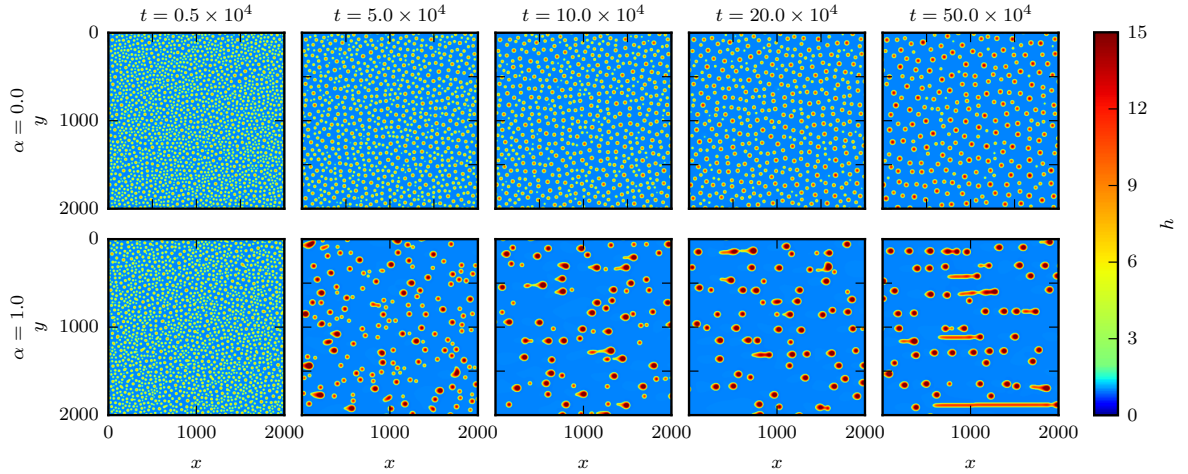


Figure 6.1: Comparison of snapshots from time evolutions of ensembles of droplets for a horizontal ($\alpha = 0$, top row) and inclined substrate ($\alpha = 1.0$, bottom row). We show NTS of (3.38)-(3.39) with $g = 0.001$ on a domain of $L_x \times L_y = 4000 \times 4000$ (only one quarter of the simulation domain is shown) initialized by a flat film of height $h_0 = 2.0$. Figure reproduced from [WTE⁺17], © 2017 American Physical Society.

average droplet size is related to the most unstable wavelength of the linear instability of the flat film. In the subsequent time evolution, both, coalescence events and breakup of droplets into two parts, are observed. Coalescence occurs whenever two droplets meet, a scenario which is promoted by the fact that droplets of different volumes slide at different velocities. Breakup of droplets is observed for large droplets. In comparison to smaller, stable droplets, the footprint of the larger drops exhibit a cusp at their tail.²

To quantify the coarsening behavior, droplet size distributions $\tilde{f}(V)$ are extracted from the NTS by kernel density estimation (cf. [Wil16] for details). Furthermore, the time evolution of the overall number of droplets in the NTS is tracked. Considering the dynamics of the droplet size distribution $\tilde{f}(V)$ shown in FIG. 6.2, the following observation can be made for all investigated values of $\alpha \neq 0$: The initial peak of the distributions at low droplet sizes (related to the most unstable wavelength) disappears swiftly, while a new peak at larger droplet sizes appears. After some time, the positions of the new maxima of the distributions remain approximately constant and even the shape relaxes to a quasi-stationary state.

² For experimental results concerning the pearling instability of sliding drops in relation to a cusp formation, we refer to [PFL01], a recent numerical study can be found in [EWGT16].

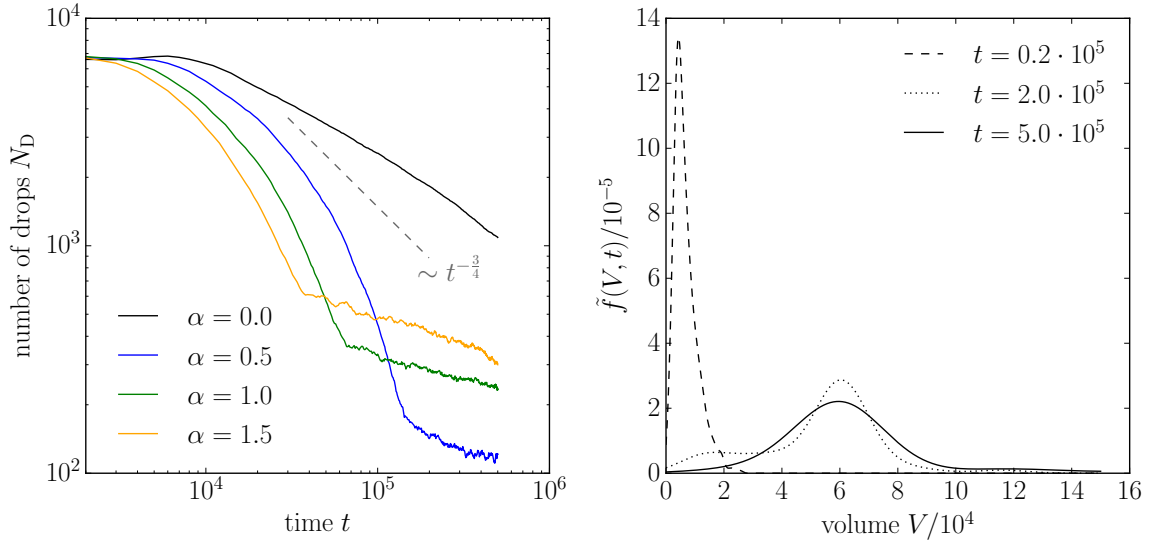


Figure 6.2: Left: Time evolution of the number of droplets as extracted from NTS of (3.38)-(3.39) for different inclination angles of the substrate (all other parameters are as in FIG. 6.1). The dashed line shows a rigorous upper bound for the coarsening rate for non-inclined substrates [ORS06]. Right: Normalized distribution of droplet volumes obtained by KDE of NTS at three different times for a time evolution at $\alpha = 1.0$. The results were obtained by Markus Wilczek (cf. [WTE⁺17]).

This saturation behavior is of course also reflected in the time evolution of the number of droplets, where - as imposed by mass conservation - the number of droplets quickly decreases as more drops of larger volume are formed. The quasi-stationary distribution is reflected in a saturation of the number of droplets. In general, it is observed that the coarsening leading to quasi-stationary distributions for the driven droplet ensembles ($\alpha \neq 0$) is significantly faster than for the case of horizontal substrates. For the latter, building on the gradient structure of (3.36), in [ORS06], a rigorous upper bound for the coarsening rate could be derived. In FIG. 6.2 this upper bound is shown together with the results from NTS. The driving gravity effects lead to frequent encounters of droplets, and therefore this upper bound is clearly exceeded for $\alpha \neq 0$.³

We proceed to discuss the phenomenon of a stationary droplet size distribution in more detail. As already mentioned, two main effects are responsible for the specific coarsening dynamics (and thus also for its saturation): The collision of droplets of different speed and the fragmentation of droplets which have become too large to be stable. An inspection of the bifurcation diagram of a single sliding droplet in dependence of its volume gives further insight into droplet stability. In FIG. 6.3, the solution subbranch present at the lowest volumes corresponds to the *simple* droplet shape (cf. solution (a) in FIG. 6.3), which is most frequently observed in the NTS at sufficiently small α . This subbranch ends in a saddle-node bifurcation at a critical volume V_{crit} . Droplets of smaller volumes are stable w.r.t. a *pearling* instability (cf. [EWGT16] for details)

³ As emphasized in, e.g., [GW03], also on flat substrates, droplets may collide due to motion induced by fluxes through the adsorption layer (see also [PP04]). This effect is not negligible for the coarsening dynamics. However, collisions are significantly more frequent for all $\alpha \neq 0$.

leading to the fragmentation. All droplets of larger volume which do not relax to an elongated droplet type⁴ (solution (d) in FIG. 6.3) are subject to fragmentation. The upper limit V_{crit} is in close relation (but not equal to) the drop size at the maximum of the droplet size distribution. This is clearly demonstrated in FIG. 6.4, where for different inclination angles α , the inflection point of the quasi-stationary distribution is located roughly at V_{crit} .

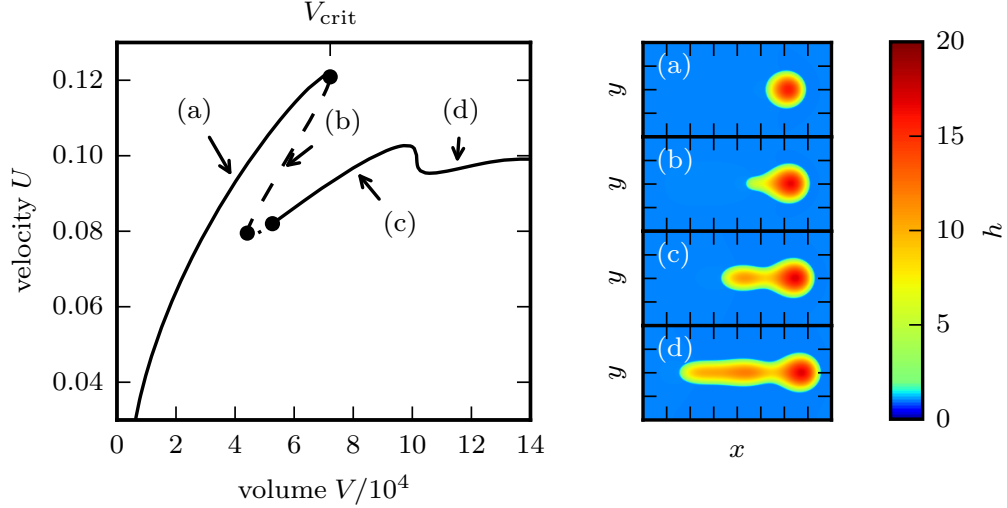


Figure 6.3: Left: Bifurcation diagram for a single sliding drop in 2D, showing the sliding velocity in dependence of its volume. Right: Exemplary solutions correspond to different subbranches of the bifurcation curve in the left panel, as indicated by the labels (a)-(d). For the ensemble statistics, we are mainly interested in the subbranch of simple droplets (solution type (a)), which ends in a saddle-node bifurcation at a volume V_{crit} . The bifurcation diagram has been obtained by Sebastian Engelkemper, cf. [EWGT16] for details. Figure adapted from [WTE⁺17], © 2017 American Physical Society.

⁴ This solution type can also be stable and is sometimes found in ensemble simulations (cf. FIG. 6.1). However, at sufficiently small inclination angles, the solution type is not very frequent in the NTS and we neglect it in the statistical modeling outlined in §6.1.2.

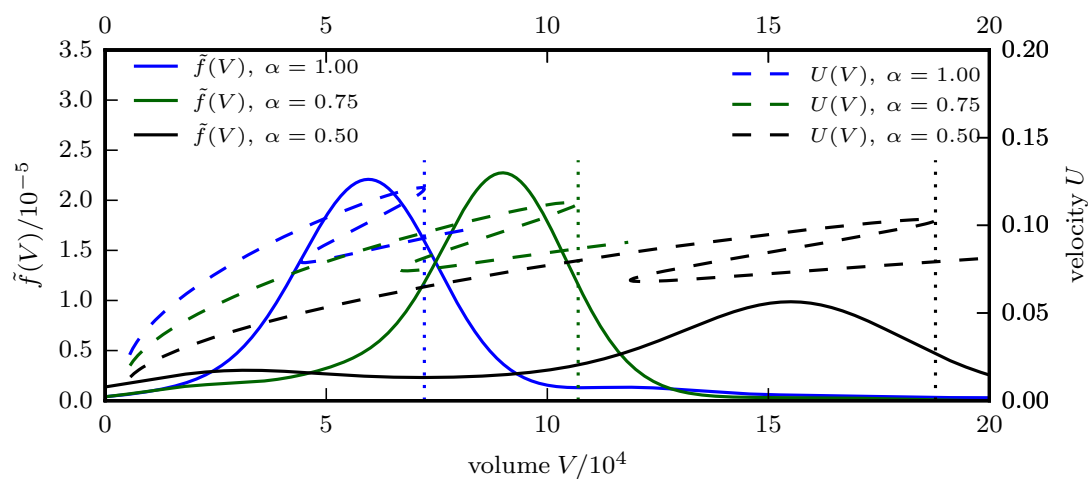


Figure 6.4: Shown is a comparison of late stage normalized volume distributions (solid lines) obtained by KDE of the NTS (cf. FIG. 6.2) with corresponding bifurcation diagrams for single droplets (dashed lines, cf. FIG. 6.3) for three different inclination angles α . For all cases, the upper inflection point of the quasi-stationary distribution is located roughly at the bifurcation point V_{crit} . (Cf. [WTE⁺17])

6.1.2 Statistical Model

While the locus of the maximum of the saturated droplet size distribution could be predicted by a corresponding bifurcation diagram (cf. FIG. 6.4), a complete statistical description should also include the coarsening dynamics leading to the saturated state. For this purpose, we formulate a Smoluchowski-type statistical model based on information from bifurcation diagrams of single droplets. The Smoluchowski equation [Smo16] is a well known integro-differential equation for a non-normalized volume distribution function $f(V) = N\tilde{f}(V)$, where

$$N_{[V, V+dV]} = f(V)dV \quad (6.1)$$

is the number of entities with a volume in the interval $[V, V + dV]$. The classical Smoluchowski equation only describes coalescence processes. Our minimal model, however, has to include both the mechanisms of coalescence of two droplets due to different sliding velocities and of fragmentation of droplets with volumes above V_{crit} . Modeling of the coarsening of droplets on substrates in terms of generalized Smoluchowski equations is also reviewed in [Mea92a] and in [Mea92b] also fragmentation is considered.

The general form of a Smoluchowski type equation capturing coalescence of pairs of droplets and fragmentation of individual drops reads [WTE⁺17]:

$$\begin{aligned} \partial_t f(V, t) = & - \underbrace{\int_0^\infty K(V, \tilde{V}) f(V) f(\tilde{V}) d\tilde{V}}_{\text{loss due to coalescence}} + \underbrace{\int_0^V \frac{1}{2} K(\tilde{V}, V - \tilde{V}) f(\tilde{V}) f(V - \tilde{V}) d\tilde{V}}_{\text{gain due to coalescence}} \\ & - \underbrace{\int_0^\infty \frac{1}{2} J(V, \tilde{V}) f(V) d\tilde{V}}_{\text{loss due to fragmentation}} + \underbrace{\int_0^\infty J(\tilde{V}, V) f(\tilde{V}) d\tilde{V}}_{\text{gain due to fragmentation}} . \end{aligned} \quad (6.2)$$

This equation is best understood as a continuous *rate equation* (cf., e.g., [Hak04]), where the kernels J and K give rates of fragmentation and coalescence, respectively in dependence of the volumina of droplets involved in the respective processes. More specifically, $K(V_1, V_2)$ models the rate of collisions of two droplets of volumes V_1 and V_2 , whereas $J(V_1, V_2)$ models the rate of fragmentation of a droplet of volume V_1 into two droplets, of volumes V_2 and $V_1 - V_2$. Conveniently, in our case, nearly all information needed for the formulation of adequate rate kernels can be obtained from the bifurcation diagrams of single sliding drops (cf. FIG. 6.3): The rate of collision $K(V_1, V_2)$ is assumed to be imposed by the mean distance of a droplet in the ensemble to any other droplets (assuming that the position of the droplets is statistically independent of their volume) and the velocity difference between two droplets of volumes V_1 and V_2 . We therefore formulate the kernel $K(V_1, V_2)$ as

$$K(V_1, V_2) = \frac{2k_1}{L} |U(V_1) - U(V_2)| . \quad (6.3)$$

Here, $L/2$ is the average distance of two droplets on the whole domain with periodic boundary conditions. The sliding velocity $U(V)$ is found from the bifurcation diagrams to follow a power law in V and to be linearly dependent on the inclination angle α :

$$U(V) = a_0 \alpha V^{\beta_0} \quad (6.4)$$

with $a_0 = 2.2 \cdot 10^{-4}$, $\beta_0 = 0.569$. Thus, a single free parameter k_1 is left in the kernel K .⁵ Slightly less information is available concerning the kernel J . While we are able to obtain the power law

$$V_{\text{crit}} = a_1 \alpha^{\beta_1}, \quad (6.5)$$

with $a_1 = 7.18 \cdot 10^4$ and $\beta_1 = -1.40$ from a large set of bifurcation diagrams for different α , we have no information on the dependence of the rate of breakup on the resulting combination of droplet sizes. To avoid unsubstantial bias, we therefore assume a breakup rate that is independent of the sizes of the droplets resulting from the fragmentation. This rate j is approached smoothly by a sigmoidal function $j\sigma(V_1, V_{\text{crit}}) = j \frac{1}{2} \left(1 + \tanh \left(\frac{V_1 - (V_{\text{crit}} + 2b_V)}{b_V} \right) \right)$ centered at the critical volume $V_1 = V_{\text{crit}}$:

$$J(V_1, V_2) = j \sigma(V_1, V_{\text{cr}}) \Theta(V_1 - V_2). \quad (6.6)$$

Here, $\Theta(V_1 - V_2)$ is the Heaviside function accounting for the fact that no fragment droplet can be larger than the initial droplet.

With the definitions of the two kernels K and J (cf. FIG. 6.5), the statistical model now depends in principle only on two free parameters (after fixing the width of the transition in the sigmoidal function in J). By rescaling time (which does not affect the steady states), this can be reduced to a single free parameter corresponding to a ratio of fragmentation and coalescence rates. Note also that with the kernels (6.3) and (6.6), the generalized Smoluchowski equation (6.2) is mass conserving in a statistical sense, i.e.,

$$\frac{d}{dt} \int_0^\infty dV V f(V) = 0. \quad (6.7)$$

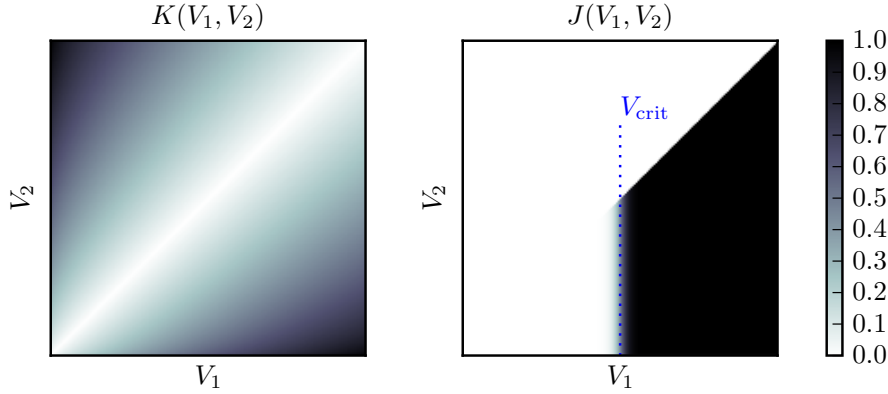


Figure 6.5: Plot of the kernel functions J and K defined by (6.6) and (6.3).

We perform numerical simulations of (6.2) by discretization of the distribution in volume-space and explicit Runge-Kutta time-stepping. Taking the distribution obtained by KDE of NTS of

⁵ This parameter can be interpreted as accounting for *laning effects*, i.e., for the fact that not all droplets on the 2D domain interact with each other, but only the ones within a certain range orthogonal to their sliding direction.

the thin-film model at an early stage as initial conditions, the time evolutions of the distribution and the number of droplets can be compared to results from simulation of (3.38)-(3.39). The discussed free parameters of the statistical model are fitted employing the NTS for $\alpha = 1$. No further fitting is performed for the other considered inclination angles. FIG. 6.6 shows that the statistical model reproduces all prominent qualitative features of the time evolution of the distribution function from KDE. More specifically, we find the fast relaxation of the distribution to a broadened stationary distribution at slightly lower values of V than the critical volume V_{crit} (shown as a dashed line in FIG. 6.6). For the time evolution of the number of droplets (which can be calculated by integration of $f(V)$), we find good quantitative agreement between the KDE and (6.2) for different inclination angles α (as emphasized before, by fitting only once for the case of $\alpha = 1$). Both, the rate of decay of the number of droplets and the time at which the saturation sets in are well reproduced (cf. FIG. 6.7). In the inset in FIG. 6.7, we further show that rescaling the time axis by the inclination angle α achieves an approximate collapse of all curves in the decay regime onto a master curve. This collapse is not only reproduced by the statistical model but can also be explained by it: In the regime of fast decay of the number of droplets, the coarsening is dominated by collision events. In (6.2), however, the rate of these events scales linearly in α , since $K(\alpha) \sim |U(\alpha)| \sim \alpha$ by virtue of (6.4).

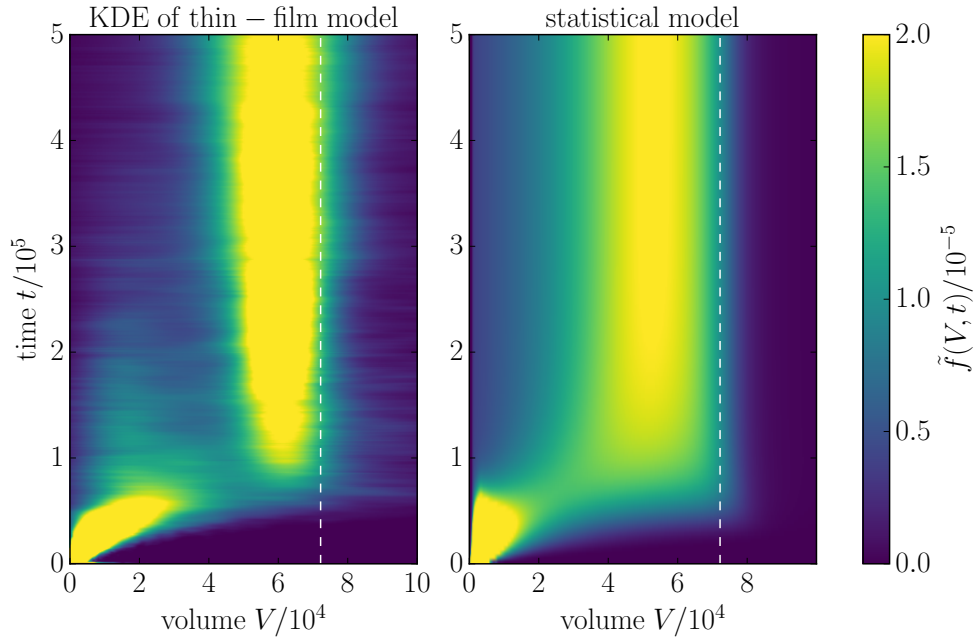


Figure 6.6: Comparison of the time evolution of the droplet size distribution $\tilde{f}(V)$ as obtained from KDE for NTS of the thin-film model (left panel) and from a numerical simulation of the statistical model (6.2). Here, the simulation of the statistical model is initialized by an early-time distribution obtained from NTS of the thin-film model. The parameters for the thin-film model are as in FIG. 6.2 and $\alpha = 1.0$. The dashed line shows the threshold volume V_{crit} (cf. FIG. 6.4). Figure adapted from [WTE⁺17].

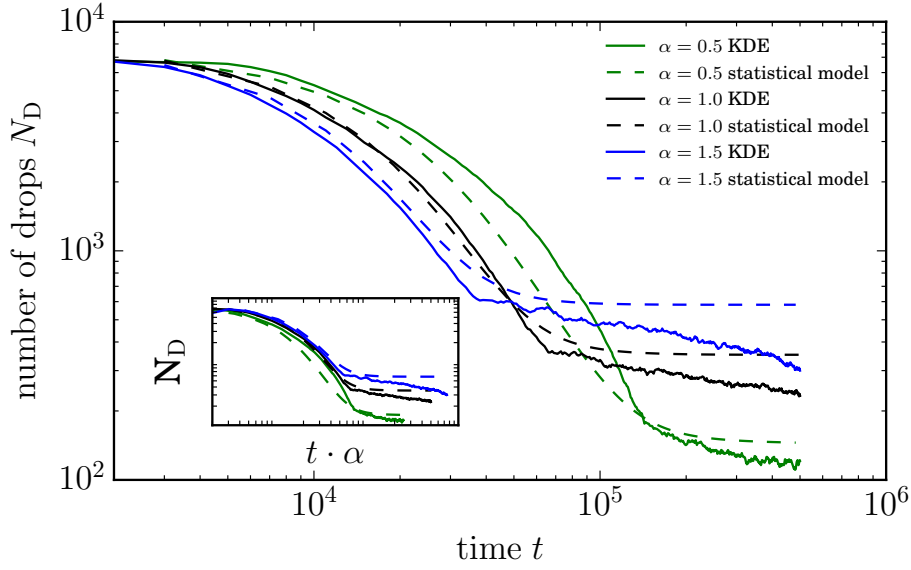


Figure 6.7: Time evolution of the number N_D of droplets for different inclination angles obtained from KDE of NTS of (3.38)-(3.39) (solid lines) and from numerical simulations of the statistical model (6.2) (dashed lines) for different inclination angles α . The free parameters in (6.2) are fitted employing the time evolution for $\alpha = 1.0$. They are kept unchanged for the other values of α . The inset shows the same results as a function of a rescaled time $\tilde{t} = t\alpha$. The curves collapse in good approximation to a master curve for the collision dominated rapid decay phase. Figure adapted from [WTE⁺17].

6.2 Order Parameter Equation For a Drop of Partially Wetting Liquid on a Rotating Cylinder

As another model system for driven liquids on solid substrates, we now consider a drop of partially wetting liquid on a rotating cylinder in 1D. As already implied in §3.2.3, for wetting liquids, there is a long tradition of studies [Mof77, Puk77, DW99, Kel09, vTH18], however, for partially wetting liquids, the system was first investigated theoretically in [Thi11]. There, analogies to the depinning of sliding droplets from heterogeneous substrates as studied, e.g., in [TK06] are elaborated. In a subsequent work [LRTT16], the bifurcation structure of the system has been analyzed in great detail, also taking into account solutions which are not droplet-like. The focus in the present work is on the analytical derivation of an order parameter equation for the system which holds in the limiting case of small Bond numbers, i.e., for small ratios of the influences of gravity and surface tension.

6.2.1 Model Equation

In §3.2.3, we have introduced a model equation for a partially wetting liquid on a cylindrical surface. To model the active rotation of the cylinder, we introduce an advection term into (3.41) and obtain (cf. FIG. 3.3):

$$\partial_t h = \partial_\theta \left(h^3 \partial_\theta [-\partial_{\theta\theta} h - h + \text{Bo} \cos(\theta) + f'(h)] - \Omega h \right). \quad (6.8)$$

We furthermore adopt the scaling from [Thi11] such that the derivative of the binding potential reads:

$$f'(h) = \frac{5}{3} \frac{\beta_0^2 h_a^2}{h^3} \left(1 - \frac{h_a^3}{h^3} \right). \quad (6.9)$$

Here, β_0 is the macroscopic contact angle of the liquid and h_a is the height of the adsorption layer in the limit of infinite domains (cf. §3.2.3). The constants in (6.8) are the already introduced Bond number Bo and the nondimensional angular driving velocity Ω . As prescribed by the geometry of the system, we consider (6.8) on a periodic domain $\theta \in [0, 2\pi]$.

In order to obtain steady states, we integrate (6.8) once and write:

$$-c_0 = h^3 \partial_\theta [-\partial_{\theta\theta} h + \text{Bo} \cos(\theta) + f'(h) - h] - \Omega h \quad (6.10)$$

$$\Leftrightarrow \partial_{\theta\theta\theta} h = -\text{Bo} \sin(\theta) + \partial_\theta (f'(h) - h) - \frac{\Omega h}{h^3} + \frac{c_0}{h^3}, \quad (6.11)$$

where c_0 is a constant, corresponding to the flux in the system. For vanishing driving velocity and vanishing flux ($c_0 = \Omega = 0$), we can integrate (6.11) once more and obtain a steady state equation analogous to (4.7):

$$-\partial_{\theta\theta} h - h + f'(h) + \text{Bo} \cos(\theta) = \mu \quad (6.12)$$

In absence of gravity ($\text{Bo}=0$), the core droplet solution⁶ of (6.12) is however a cut-off cosine and not a parabola:

$$-\partial_{\theta\theta} h - h = \mu \Rightarrow h(\theta) \propto \cos(\theta + \phi) + C, \quad (6.13)$$

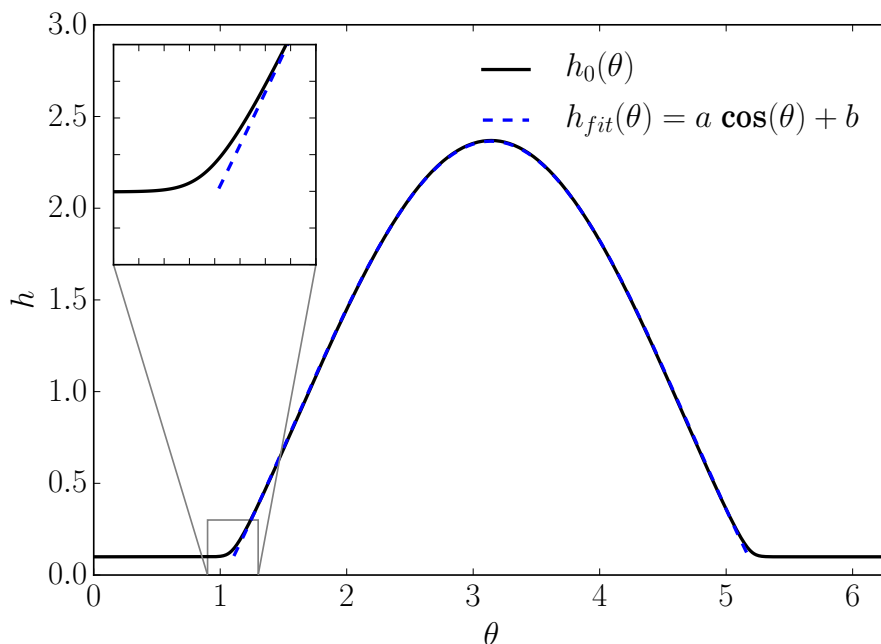


Figure 6.8: Steady state of (6.8) obtained by numerical continuation for $h_a = 0.1$, $\beta_0^2 = 2.0$, $\text{Bo} = 0$ and a mean mass $m = 1.0$. In comparison, we show a fit based on the steady state equation (6.12) which is valid in the core region. Only in the contact line region, a deviation is clearly visible.

where ϕ is an arbitrary phase constant reflecting the translational invariance for $\text{Bo} = 0$. In FIG. 6.8, we show a steady state solution of (6.8) for $\Omega = \text{Bo} = 0$ and $\beta_0^2 = 2.0$ in comparison to a fitted cosine function. For $\text{Bo} > 0$, the stable steady state solution of the system is a droplet pending on the down-side of the cylinder, i.e., at $\theta = \pi$.

Taking into account non-vanishing angular driving velocities at a given $\text{Bo} > 0$, two different scenarios were found in [Thi11] for the droplets: For sufficiently small values of Ω , the pending droplet is dragged by the rotation from the $\theta = \pi$ position. However, held back by gravity, it remains pinned at a certain angle θ_{pin} . Above a certain threshold velocity Ω_{crit} , the droplet depins and starts to rotate with the cylinder. Here, the droplet does not instantaneously follow the rotation of the cylinder, but depending on the current position exhibits a certain slip with respect to the surface of the cylinder (cf. FIG. 6.9 for an exemplary NTS of the rotation dynamics). For small Bond numbers, it was found numerically in [Thi11] that the period T of the rotation of the droplet diverges as

$$T \sim (\Omega - \Omega_{\text{crit}})^{-1/2} \quad (6.14)$$

when the threshold driving velocity Ω_{crit} is approached. It could thus be inferred that the bifurcation associated with the depinning of the droplet is a global bifurcation commonly referred to as *SNIPER* bifurcation [Str14].

⁶ As in 4.2.3, by *core*, we mean the region of a droplet where due to a large film height contributions from the binding potential can be neglected.

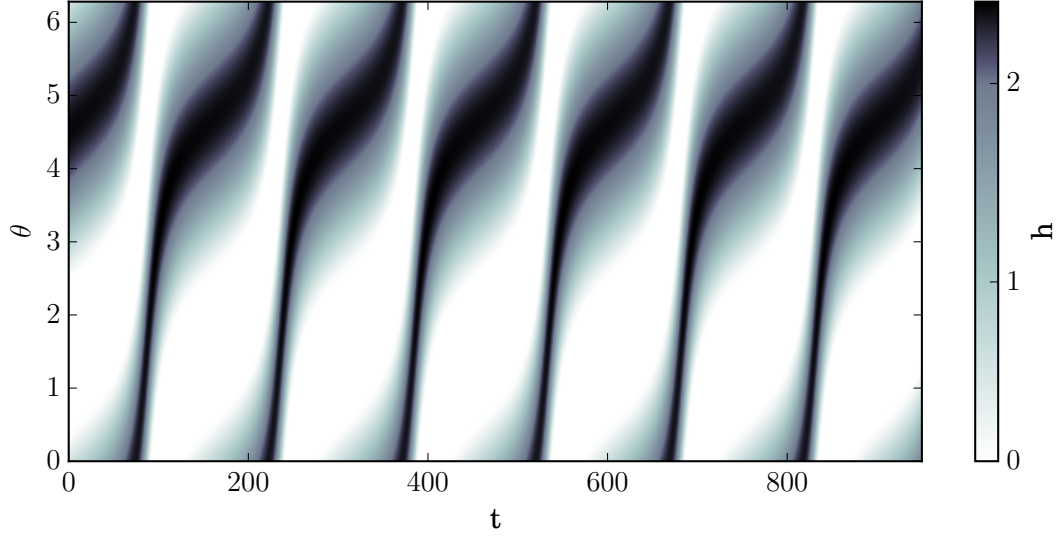


Figure 6.9: Space-time plot of a NTS of (6.8), showing the periodic but strongly nonuniform motion of a depinned droplet at $\Omega = 0.16$, $\text{Bo} = 0.1$. All other parameters are as in FIG. 6.8.

6.2.2 First Derivation of the Order Parameter Equation

We now derive an order parameter equation for the position of a single droplet on the rotating cylinder, valid at angular velocities which are not far above the depinning threshold and for very small Bond numbers Bo . We therefore assume the two parameters Ω and Bo to be of order $\mathcal{O}(\epsilon)$ with $\epsilon \ll 1$. Thus, we formally introduce scaled parameters $\Omega = \epsilon \tilde{\Omega}$ and $\text{Bo} = \epsilon \tilde{\text{Bo}}$ in (6.8) but immediately drop the tildes for convenience. In this regime, we conjecture that the droplet is only weakly (correction of $\mathcal{O}(\epsilon)$) deformed by gravity. The derivation presented in this subsection is based on a projection approach very similar to the one outlined in, e.g., [GW03]. The following ansatz is employed⁷:

$$h(\theta, t) = h_0(\theta, \tau) + \epsilon h_1(\theta, \tau) = h_0(\theta - \eta(\tau)) + \epsilon h_1(\theta, \tau), \quad (6.15)$$

where $h_0(\theta)$ solves the equation ((6.11)) on the periodic domain with vanishing gravity (thus vanishing Bond number Bo and for $\Omega = 0$). For convenience, the solution $h_0(\theta)$ is chosen such

⁷For similar perturbative treatment of a heterogeneity see also, e.g., [LBE12] for front propagation with heterogeneities or [TSTG17] for optical solitons in an inhomogeneous laser cavity. However, in those cases the linear operator of the homogeneous system is self-adjoint which is here not the case.

that $h_0(\pi + \theta) = h_0(\pi - \theta)$. Furthermore, the slow timescale $\tau := \epsilon t$ has been introduced.⁸ Inserting the ansatz in equation (6.8), gives:

$$\begin{aligned} -\epsilon \dot{\eta} \partial_\theta h_0(\theta - \eta) = & \epsilon \partial_\theta \left(h_0(\theta - \eta)^3 \partial_\theta [-\partial_{\theta\theta} h_1 - f''(h_0)h_1 - h_1] \right) \\ & - \epsilon \Omega \partial_\theta h_0(\theta - \eta) + \epsilon \partial_\theta \left[h_0(\theta - \eta)^3 \partial_\theta (\text{Bo} \cos(\theta)) \right] + \mathcal{O}(\epsilon^2) \end{aligned}$$

We now introduce $\bar{\theta} = \theta - \eta$ as a new variable and immediately omit the tildes, all the derivatives remain unaltered. All terms which were previously identified as $\mathcal{O}(\epsilon^2)$ are also dropped.

$$\begin{aligned} (-\dot{\eta} + \Omega) \partial_\theta h_0(\theta) = & \partial_\theta \left(h_0(\theta)^3 \partial_\theta [-\partial_{\theta\theta} h_1 - f''(h_0)h_1 - h_1] \right) \\ & + \partial_\theta \left(h_0(\theta)^3 \text{Bo} \partial_\theta \cos(\theta + \eta) \right). \end{aligned} \quad (6.16)$$

Note that $h_0(\theta)$ is now centered around π once again. We define the linear operator

$$\mathfrak{L}[h_0]h_1 := \partial_\theta \left(h_0^3 \partial_\theta [-\partial_{\theta\theta} h_1 - f''(h_0)h_1 - h_1] \right) \quad (6.17)$$

and perform a projection of (6.16) onto the adjoint translational eigenmode ξ of \mathfrak{L} which is given by (cf. [GW03]):

$$\xi(\theta) = \int_{\pi}^{\theta} d\theta' \frac{h_0(\theta') - h_{\min}}{h_0(\theta')^3}, \quad (6.18)$$

where h_{\min} denotes the effective adsorption layer height which is reached at $\theta = 0$ for the solution h_0 . Equation (6.16) projected onto ξ yields:

$$\begin{aligned} (-\dot{\eta} + \Omega) \underbrace{\int_0^{2\pi} \xi(\theta) \partial_\theta h_0 \, d\theta}_{(i)} = & \epsilon \underbrace{\int_0^{2\pi} \xi(\theta) \partial_\theta \left(h_0^3 \partial_\theta [-\partial_{\theta\theta} h_1 - f''(h_0)h_1 - h_1] \right) d\theta}_{(ii)} \\ & - \underbrace{\int_0^{2\pi} \xi(\theta) \partial_\theta \left(h_0^3 \text{Bo} \sin(\theta + \eta) \right) d\theta}_{(iii)}, \end{aligned} \quad (6.19)$$

⁸ The time derivatives denoted by a dot which are used in the following correspond to derivatives with respect to τ .

where

$$\begin{aligned}
 (i) : & \int_0^{2\pi} \int_{\pi}^{\theta} \frac{h_0(\theta') - h_{\min}}{h_0(\theta')^3} d\theta' \partial_{\theta} (h_0(\theta) - h_{\min}) d\theta \\
 & = \underbrace{\left[\int_{\pi}^{\theta} \frac{h_0(\theta') - h_{\min}}{h_0(\theta')^3} d\theta' (h_0(\theta) - h_{\min}) \right]_0^{2\pi}}_{=0} - \int_0^{2\pi} \frac{(h_0(\theta) - h_{\min})^2}{h_0(\theta)^3} d\theta =: -\mathfrak{D} \quad (6.20)
 \end{aligned}$$

$$\begin{aligned}
 (ii) : & \int_0^{2\pi} \int_{\pi}^{\theta} \frac{h_0(\theta') - h_{\min}}{h_0(\theta')^3} d\theta' \partial_{\theta} \left(h_0^3 \partial_{\theta} [-\partial_{\theta\theta} h_1 - f''(h_0) h_1 - h_1] \right) d\theta \\
 & = \underbrace{\left[\int_{\pi}^{\theta} \frac{h_0(\theta') - h_{\min}}{h_0(\theta')^3} d\theta' \left(h_0^3 \partial_{\theta} [-\partial_{\theta\theta} h_1 - f''(h_0) h_1 - h_1] \right) \right]_0^{2\pi}}_{\mathcal{O}(\epsilon^2)} \\
 & \quad - \underbrace{\int_0^{2\pi} (h_0(\theta) - h_{\min}) \partial_{\theta} (-\partial_{\theta\theta} h_1 - f''(h_0) h_1 - h_1) d\theta}_{\int_0^{2\pi} \partial_{\theta} h_0(\theta) (-\partial_{\theta\theta} h_1 - f''(h_0) h_1 - h_1) d\theta = 0} \quad (6.21)
 \end{aligned}$$

$$\begin{aligned}
 (iii) : & \int_0^{2\pi} \int_{\pi}^{\theta} \frac{h_0(\theta') - h_{\min}}{h_0(\theta')^3} d\theta' \partial_{\theta} \left(h_0^3 \text{Bo} \sin(\theta + \eta) \right) d\theta \\
 & = \left[\int_{\pi}^{\theta} \frac{h_0(\theta') - h_{\min}}{h_0(\theta')^3} d\theta' \left(\text{Bo} h_0^3 \sin(\theta + \eta) \right) \right]_0^{2\pi} - \int_0^{2\pi} h_0(\theta) \text{Bo} \sin(\theta + \eta) d\theta \\
 & = \underbrace{\int_0^{2\pi} \frac{h_0(\theta') - h_{\min}}{h_0(\theta')^3} d\theta' \text{Bo} h_{\min}^3 \sin(\eta)}_{\mathcal{O}(h_{\min}^3)} - \text{Bo} \int_0^{2\pi} h_0(\theta) \sin(\theta + \eta) d\theta, \quad (6.22)
 \end{aligned}$$

with

$$\int_0^{2\pi} h_0(\theta) \sin(\theta + \eta) d\theta = \int_0^{2\pi} h_0(\theta) \sin(\theta) \cos(\eta) + \sin(\eta) \cos(\theta) d\theta = \tilde{h}_{0,1} \sin(\eta), \quad (6.23)$$

where we defined the Fouriermode

$$\tilde{h}_{0,1} = \int_0^{2\pi} h_0(\theta) \cos(\theta) d\theta. \quad (6.24)$$

Collecting the terms (i),(ii) and (iii), equation (6.19) describing the time evolution of the position of the droplet becomes ⁹:

$$\dot{\eta} = \frac{\text{Bo}\tilde{h}_{0,1}}{\mathfrak{D}} \sin(\eta) + \Omega \quad (6.25)$$

which is in fact the well known Adler equation [Adl46]. The constant \mathfrak{D} is defined in (6.20). Note that this equation is valid up to the order $\mathcal{O}(\epsilon^2)$.

6.2.3 Second Derivation of the Order Parameter Equation

We will now show that (6.25) can also be derived through the use of the variational principle (2.14). We thereby give an explicit example for the equivalence of the projection approach and a variational approach for a quasistatic approximation as discussed in §2.2.2. We first consider (6.8) without external driving ($\Omega = 0$). It can then be formulated in the following variational form

$$\mathcal{R}_{\text{rot}} = \underbrace{\frac{1}{2} \int_0^{2\pi} \frac{J^2}{h^3} d\theta}_{=\mathcal{D}} - \int_0^{2\pi} \frac{\delta \mathcal{F}}{\delta h} \partial_\theta J d\theta, \quad \frac{\delta \mathcal{R}_{\text{rot}}}{\delta J} = 0, \quad \partial_t h = -\partial_\theta J. \quad (6.26)$$

In the spirit of §2.2.2, the energy functional can be splitted into two contributions :

$$\mathcal{F} = \underbrace{\int_0^{2\pi} \frac{1}{2} \left((\partial_\theta h)^2 - h^2 \right) + f(h) d\theta}_{\mathcal{F}_0} + \epsilon \underbrace{\int_0^{2\pi} \text{Bo} \cos(\theta) h d\theta}_{\mathcal{F}_1}. \quad (6.27)$$

We employ the ansatz $h(\theta, t) = h_0(\theta - \eta(\tau))$, $\tau = et$, where h_0 is, as before, a solution of (6.12) for $\text{Bo}=0$ and therefore an extremum of the unperturbed energy \mathcal{F}_0 . We now intend to formulate a reduced Rayleighian as a function of $(\theta, \dot{\theta})$. The dissipation \mathcal{D} in dependence of η can be calculated as

$$\begin{aligned} -\epsilon \dot{\eta} \partial_\theta h_0 &= \partial_\theta \left(h^3 \partial_\theta \frac{\delta F}{\delta h} \right) \\ \Rightarrow -\dot{\eta} (h_0 - h_{\min}) &= \underbrace{h^3 \partial_\theta \frac{\delta F}{\delta h}}_{=J} - \underbrace{h^3 \partial_\theta \frac{\delta F}{\delta h} |_{h_{\min}}}_{\approx -\text{Bo} h_{\min}^3 \sin(\eta)} \end{aligned} \quad (6.28)$$

with

$$\mathcal{D} = \frac{1}{2} \int_0^{2\pi} \frac{J^2}{h_0^3} d\theta. \quad (6.29)$$

⁹ We also omitted the first summand in (6.22).

Neglecting the second summand of the r.h.s. in (6.28), we now compute

$$\frac{\partial}{\partial \dot{\eta}} \mathcal{D} = \underbrace{\epsilon^2 \dot{\eta} \int_0^{2\pi} \frac{(h_0 - h_{\min})^2}{h_0^3} d\theta}_{\mathfrak{D}} \quad (6.30)$$

$$\frac{\partial F}{\partial \eta} = \epsilon \frac{\partial F_1}{\partial \eta} = -\epsilon \text{Bo} \int_0^{2\pi} h_0 \sin(\theta + \eta) d\theta = -\epsilon \text{Bo} \tilde{h}_{0,1} \sin(\eta). \quad (6.31)$$

The coarse-grained variational principle then results in (cf. §(2.2.2)):

$$\epsilon \frac{\partial F}{\partial \eta} + \frac{\partial}{\partial \dot{\eta}} \mathcal{D} = 0 \Rightarrow \dot{\eta} = \frac{\text{Bo} \tilde{h}_{0,1}}{\mathfrak{D}} \sin(\eta) \quad (6.32)$$

Adding the active advection term Ω to the equation of motion for the position of the droplet (6.32), we finally obtain the Adler equation for the depinning of the droplet in agreement with the first derivation §6.2.2 (cf. (6.25)). It is noteworthy that for this second derivation no knowledge about the adjoint eigenfunction of the non-selfadjoint linearised operator is necessary.

6.2.4 Results of the Order Parameter Equation and Outlook

After calculating $\tilde{h}_{0,1}$ and \mathfrak{D} numerically from the steady state solution obtained by numerical continuation (cf. FIG. 6.8), the order parameter equation (6.25) can be treated analytically.¹⁰ For the steady states in the pinning regime, we have to solve

$$\frac{\text{Bo} \tilde{h}_{0,1}}{\mathfrak{D}} \sin(\eta_{\text{pin}}) + \Omega = 0. \quad (6.33)$$

For sufficiently small Bond numbers, the resulting pinning angles $\theta_{\text{pin}} = \eta_{\text{pin}} + \pi$ coincide remarkably well with the pinning positions obtained by numerical continuation of (6.11) (cf. FIG. 6.10). For the time-periodic (depinning) regime, (6.25) can be integrated by separation of variables [Str14] resulting in the following implicit analytical solution:

$$t(\eta) = -\frac{2}{\sqrt{\Omega^2 - \xi^2}} \arctan \left(\frac{-\Omega \tan(\eta/2) + \xi}{\sqrt{\Omega^2 - \xi^2}} \right) + C \quad \text{where} \quad \xi = -\frac{\text{Bo} \tilde{h}_{0,1}}{\mathfrak{D}}. \quad (6.34)$$

This solution exhibits the scaling (6.14) which was found numerically in [Thi11]. Furthermore, it reproduces the time evolution of the position of the droplets maximum in good approximation (cf. FIG. 6.11). Note that the main discrepancy is a slight mismatch in the periods. We have thus shown that for sufficiently small Bond numbers the order parameter equation (6.25) describes the droplet very well both in the pinned and in the depinned regime. However, for larger Bond numbers, the critical driving velocities Ω_{crit} and the deformation of the droplets increase significantly and the quasistatic ansatz outlined in §6.2.2 and §6.2.3 is not sufficient anymore. In [Gla05] and more recently also in [MD17], in the context of Onsager's variational principle, the authors discuss more elaborated ansatz functions depending on two parameters which are related to the position and the deformation of a driven droplet.

¹⁰ In the following, Bo and Ω will denote the non-scaled values of the Bond number and the driving velocity in contrast to the scaled parameters introduced in 6.2.2.

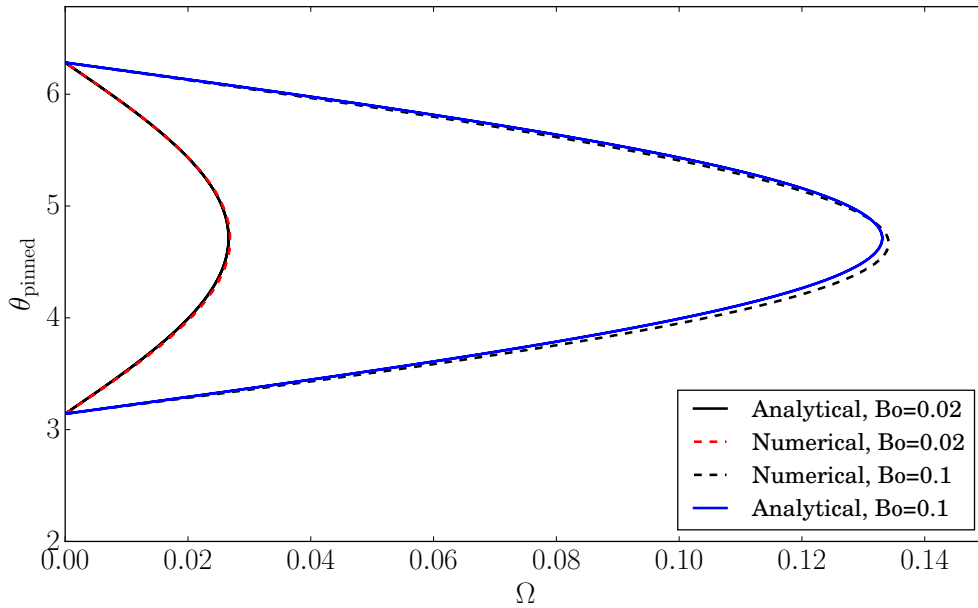


Figure 6.10: (Semi-)analytically calculated (stable and unstable) pinning positions θ_{pin} obtained from the order parameter equation (6.25) in comparison with the pinning position obtained by numerical continuation of (6.11) for two different Bond numbers Bo . For $Bo=0.02$ barely any deviation can be seen, for $Bo=0.1$, the deviation is of the order of magnitude anticipated in the derivation 6.2.2.

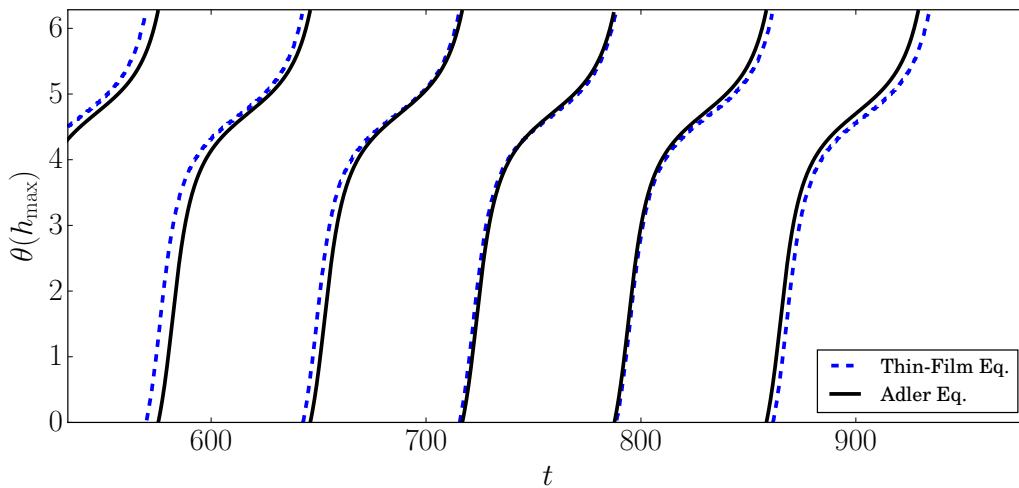


Figure 6.11: Comparison of NTS results (dashed lines) for the time evolution the maximum position of a depinned droplet in comparison to the analytical solution (6.34) (solid lines). We chose $Bo=0.1$, $\Omega = 0.16$ and the remaining parameters as in FIG. 6.8.

While in [Gla05], the approximation outlined for sliding droplets on inclined surfaces is still of quasistatic type (i.e., the ansatz function is formulated based on a family of extrema of an unperturbed energy functional), this is not the case in [MD17]. There, to model the deformation of a droplet, a parabolic ansatzfunction is supplemented by a simple deformation factor. In the spirit of [MD17], a possible extended ansatz function for the system discussed in this chapter could be the following function parametrized by three dynamic order parameters:

$$h_{\text{h.o.}}(\theta) = m [\cos(\theta - \theta_c) - \cos(a)] (1.0 + \delta(\theta - \theta_c)) \quad (6.35)$$

where m fixes the constant mass of the droplet, the position of the droplet is described by $\theta_c(\tau)$, a symmetrical deformation (“broadening”) is described by $a(\tau)$ and an asymmetrical deformation (“tilting”) is captured by $\delta(\tau)$. The derivation of a three dimensional order parameter equation based on this ansatz function is a possible path for future work on the system.¹¹

6.3 Conclusion

In this chapter, we have outlined two different coarse graining procedures for the description of driven liquids on substrates. For the case of ensembles of sliding droplets, a minimal statistical model, substantiated by information from bifurcation studies of single droplets, reproduces in good approximation the coarsening dynamics captured by large scale NTS of the full thin-film model. There are multiple aspects interesting for future work on the system: As discussed, for now, the model does not include any information about the breakup probabilities for different combinations of fragment droplets. These could possibly be obtained by a more detailed analysis of the large scale NTS and then readily included into the formulation of the corresponding kernel. However, here, also memory effects could be important, e.g., fragmentation probabilities that depend on previous coalescence events. Furthermore, at larger inclination angles of the substrate, the elongated droplet type (cf. FIG. 6.3) is more frequent and thus not anymore negligible. Effects of their presence thus have to be included in the statistical model for larger inclination angles. Finally, recently, also large scale NTS of a thin-film model including condensation have been conducted and statistically analyzed [Eng17]. A modeling of the statistics of such a system would also be of interest but is highly nontrivial.

In the second part of the chapter, a quasistatic approximation of the dynamics of a droplet on a rotating cylinder has been outlined based on a projection approach and a variational approach. The presented approaches are semi-analytical in the sense that a numerically obtained steady state solution is required. As discussed in §6.2.4, a possible further extension of the approach would be based on a parametrically deformed core solution. A very important aspect of such an extension is the appropriate treatment of the dissipation at the contact line. An elaborated treatment of this problem, possibly in combination with experimental results or information from microscopic modeling (cf. [QWS06]) would be of great interest also for a larger class of systems of liquids on surfaces.

¹¹ Note that while employing the numerical steady state solution of (6.11) as in 6.2.3, the dissipation integral can be calculated without restrictions. The dissipation at the contact line is then regularized by the adsorption layer approach (cf. 3.2.3). When employing the ansatz function (6.35), one way to regularize the dissipation is the introduction of a cut-off height $h_{\text{cut}} > 0$ (cf. [Gla05, MD17] for details). This cut-off height can be seen as a fitting parameter of the approximation.

7 Summary and Conclusion

In the present thesis, we have investigated phenomena related to different instabilities occurring for films, drops and ridges on solid substrates in terms of modeling, simulation and theoretical analysis. From a conceptual point of view, we have thus illustrated by multiple examples how the combination of numerical continuation, direct numerical simulations and analytical approaches results in a fruitful symbiosis.

The main focus has been on the so-called *thin-film equation*, a nonlinear PDE for the time evolution of the height profile of shallow liquid structures on a solid substrate. This equation belongs to the class of *gradient systems* and can be formulated based on *Onsager's variational principle* (cf. e.g., [XTQ15]).

The general introduction of this principle and the derivation of the thin-film equation emphasizing the variational structure underlying the hydrodynamic equations has been the topic of Chap. 2 and Chap. 3 of the thesis. In Chap. 2, we have also elaborated the use of the variational principle for coarse graining (cf. [Doi15]) and presented a - to the author's awareness - novel derivation of order parameter equations both for the standard and the conserved Swift-Hohenberg equation.

In the subsequent chapter, the Plateau-Rayleigh instability of liquid ridges on chemically prepatterned substrates has been investigated first in terms of the thin-film equation. We have been able to reproduce qualitative experimental observations from [WDW⁺11] and have investigated, in particular, the growth of coupled instabilities of adjacent ridges. Here, an interesting topic for future work would be the investigation of 2D structures like bridge states between adjacent prepattern stripes (cf. [WC12]) through 2D numerical continuation.

Furthermore, results from the modeling of the instability based on the thin-film equation have been shown to be in good qualitative agreement with corresponding results from KMC simulations. Also in Chap. 4, as a first step towards a quantitative mapping of KMC simulations to a thin-film type model, we have discussed the concept of the *binding potential* and a novel approach to the numerical extraction of the latter from DFT. In future work, the mapping of dynamics of the KMC model to a DDFT, like, e.g., recently presented in [CSA17a] would give further insight for the multiscale modeling of liquids on prepatterned substrates. In the next step, such a DDFT model could be further coarse-grained in order to obtain a gradient dynamics model on an effective interface Hamiltonian which is in quantitative agreement with averaged results from KMC.

In the first part of Chap. 5, we have demonstrated the applicability of the concept of *pulled fronts* for the theoretical analysis of instabilities which are spreading in shallow free surface liquids through front propagation. More specifically, we have investigated the front propagation of spinodal dewetting fronts in flat thin films and the propagation of Plateau-Rayleigh instabilities of ridges on substrates. For both systems a further improved numerical approach, e.g., employing an adaptive spatial mesh would allow for a more thorough investigation of the front propagation, which necessitates large simulation domains. For the case of front propagation into flat linearly unstable films, a numerical continuation of fronts leaving behind periodic states would be of great interest.

In the second part of Chap. 5, we have then discussed pattern formation in a driven system, i.e., in the *dip-coating* geometry: Time periodic solutions have been analyzed in terms of numerical time simulations and numerical continuation and an onset of the patterning regime in parameter space could be related to the analytically calculated propagation speed of instability fronts into flat films of Landau–Levich film height. Here, an interesting question is whether the described pattern formation through dip-coating employing simple liquids can be realized experimentally.

In the final chapter, we have shown two examples for the formulation of coarse-grained dynamical equations for driven liquids on substrates. More specifically, in the first part, we have discussed a statistical model for the coarsening dynamics in a large ensemble of sliding droplets in terms of an augmented Smoluchowski coagulation equation. Here, coalescence and fragmentation kernels have been formulated based on results from numerical continuation of a thin-film equation describing individual sliding droplets. The resulting integro-differential equation is able to reproduce qualitatively the time evolution of the droplet size distribution as obtained from numerical time simulations of the thin-film model. The time evolution of the number of droplets has been reproduced quantitatively for different inclination angles of the substrate. In Chap. 6, we have already discussed further possible extensions of the statistical investigation of the coarsening of sliding droplets. However, the general approach of the formulation of a statistical model of many interacting structures based on information obtained from the numerical continuation of individual structures might also be beneficial for different nonlinear nonequilibrium systems.

In the second part of Chap. 6, we have shown that for the limit of small Bond numbers, the pinning and depinning of a droplet of partially wetting liquid on a rotating cylinder can be described very accurately by an ODE of the form of the well known *Adler equation*. We have presented two different derivations of the ODE, and thereby illustrated the equivalence of a projection approach and a variational approach to the coarse graining of equations which can be formulated by Onsager’s variational principle. We have thus added a further example for the formulation of coarse-grained model equations for thin liquids on substrates based on Onsager’s variational principle. This approach has recently been put forward in a number of publications [XDD16, MD17, Gla05, MD16, DXZD18] and seems very promising for future analytical work on viscous liquids on substrates. As discussed in Chap. 6, an inclusion of results for the dissipation at the contact line obtained from microscopic models into the formalism is desirable.

List of Publications

The following manuscripts were published during the course of this thesis, sorted in chronological order. Authors marked with an asterisk contributed equally to the publication:

[WTG⁺15] M. Wilczek, W. B. H. Tewes, S. V. Gurevich, M. H. Koöpf, L. F. Chi, and U. Thiele. Modelling pattern formation in dip-coating experiments. *Math. Model. Nat. Phenom.*, 10(4):44–60, 2015.

[TBH⁺17] W. Tewes*, O. Buller*, A. Heuer, U. Thiele, and S. V. Gurevich. Comparing kinetic Monte Carlo and thin-film modeling of transversal instabilities of ridges on patterned substrates. *J. Chem. Phys.*, 146(9):94704, 2017.

[BTA⁺17] O. Buller*, W. Tewes*, A. J. Archer, A. Heuer, U. Thiele, and S. V. Gurevich. Nudged elastic band calculation of the binding potential for liquids at interfaces. *J. Chem. Phys.*, 147(2):24701, 2017.

[WTE⁺17] M. Wilczek, W. Tewes, S. Engelnkemper, S. V. Gurevich, and U. Thiele. Sliding Drops: Ensemble Statistics from Single Drop Bifurcations. *Phys. Rev. Lett.*, 119(20):204501, 2017.

Furthermore, the following manuscript is in preparation:

[TWGT18] W. Tewes, M. Wilczek, S. V. Gurevich, and U. Thiele. Self-organised dip-coating patterns of simple, partially wetting, nonvolatile liquids. *In preparation*, 2018.

Bibliography

- [AC79] S. M. Allen and J. W. Cahn. A microscopic theory for antiphase boundary motion and its application to antiphase domain coarsening. *Acta Metall.*, 27(6):1085–1095, 1979.
- [Adl46] R. Adler. A study of locking phenomena in oscillators. *Proc. IRE*, 34(6):351–357, 1946.
- [AE04] A. J. Archer and R. Evans. Dynamical density functional theory and its application to spinodal decomposition. *J. Chem. Phys.*, 121(9):4246–4254, 2004.
- [AE11] A. J. Archer and R. Evans. Nucleation of liquid droplets in a fluid with competing interactions. *Mol. Phys.*, 109(23-24):2711–2722, 2011.
- [Ale77] R. Alexander. Diagonally implicit Runge–Kutta methods for stiff ODE’s. *SIAM J. Numer. Anal.*, 14(6):1006–1021, 1977.
- [AM16] G. Altshuler and O. Manor. Free films of a partially wetting liquid under the influence of a propagating MHz surface acoustic wave. *Phys. Fluids*, 28(7):72102, 2016.
- [AR04] A. J. Archer and M. Rauscher. Dynamical density functional theory for interacting Brownian particles: Stochastic or deterministic? *J. Phys. A-Math. Gen.*, 37(40):9325–9333, 2004.
- [ART10] A. J. Archer, M. J. Robbins, and U. Thiele. Dynamical density functional theory for the dewetting of evaporating thin films of nanoparticle suspensions exhibiting pattern formation. *Phys. Rev. E*, 81(2):21602, 2010.
- [Bas07] J.-L. Basdevant. *Variational principles in physics*. Springer Science & Business Media, New York, 2007.
- [BBD⁺08a] P. Bastian, M. Blatt, A. Dedner, C. Engwer, R. Klöforn, R. Kornhuber, M. Ohlberger, and O. Sander. A generic grid interface for parallel and adaptive scientific computing. Part II: Implementation and tests in DUNE. *Computing*, 82(2-3):121–138, 2008.
- [BBD⁺08b] P. Bastian, M. Blatt, A. Dedner, C. Engwer, R. Klöforn, M. Ohlberger, and O. Sander. A generic grid interface for parallel and adaptive scientific computing. Part I: abstract framework. *Computing*, 82(2-3):103–119, 2008.
- [BHM10] P. Bastian, F. Heimann, and S. Marnach. Generic implementation of finite element methods in the distributed and unified numerics environment (DUNE). *Kybernetika*, 46(2):294–315, 2010.

- [BKTB02] L. Bruschi, H. Kühne, U. Thiele, and M. Bär. Dewetting of thin films on heterogeneous substrates: Pinning versus coarsening. *Phys. Rev. E*, 66(1):11602, 2002.
- [BSMM12] I. N. Bronstein, K. A. Semendjajew, G. Musiol, and H. Mühlig. *Taschenbuch der Mathematik*. Wissenschaftlicher Verlag Harri Deutsch, Frankfurt, 7th edition, 2012.
- [BTA⁺17] O. Buller, W. Tewes, A. J. Archer, A. Heuer, U. Thiele, and S. V. Gurevich. Nudged elastic band calculation of the binding potential for liquids at interfaces. *J. Chem. Phys.*, 147(2):24701, 2017.
- [Cah59] J. W. Cahn. Free energy of a nonuniform system. II. Thermodynamic basis. *J. Chem. Phys.*, 30(5):1121–1124, 1959.
- [Cah65] J. W. Cahn. Phase separation by spinodal decomposition in isotropic systems. *J. Chem. Phys.*, 42(1):93–99, 1965.
- [CG09] P. Y. Chan and N. Goldenfeld. Nonlinear elasticity of the phase-field crystal model from the renormalization group. *Phys. Rev. E*, 80(6):65105, 2009.
- [CH58] J. W. Cahn and J. E. Hilliard. Free energy of a nonuniform system. I. Interfacial free energy. *J. Chem. Phys.*, 28(2):258–267, 1958.
- [CH93] M. C. Cross and P. C. Hohenberg. Pattern formation outside of equilibrium. *Rev. Mod. Phys.*, 65(3):851, 1993.
- [CLH⁺07] X. Chen, S. Lenhart, M. Hirtz, N. Lu, H. Fuchs, and L. Chi. Langmuir–Blodgett patterning: a bottom–up way to build mesostructures over large areas. *Acc. Chem. Res.*, 40(6):393–401, 2007.
- [CM09] R. V. Craster and O. K. Matar. Dynamics and stability of thin liquid films. *Rev. Mod. Phys.*, 81(3):1131–1198, 2009.
- [CP84] P. Császár and P. Pulay. Geometry optimization by direct inversion in the iterative subspace. *J. Mol. Struct.*, 114:31–34, 1984.
- [CRMF89] Z. Cheng, S. Redner, P. Meakin, and F. Family. Avalanche dynamics in a deposition model with sliding. *Phys. Rev. A*, 40(10):5922, 1989.
- [CSA17a] C. Chalmers, R. Smith, and A. J. Archer. Dynamical density functional theory for the evaporation of droplets of nanoparticle suspension. *Langmuir*, 33(50):14490–14501, 2017.
- [CSA17b] C. Chalmers, R. Smith, and A. J. Archer. Modelling the evaporation of nanoparticle suspensions from heterogeneous surfaces. *J. Phys. Condens. Matter*, 29(29):295102, 2017.
- [Der45] B. Derjaguin. On the thickness of the liquid film adhering to the walls of a vessel after emptying. *Acta Physicochim. URSS*, 20:349–352, 1945.

-
- [DG16] J. A. Diez and A. G. González. Breakup of thin liquid filaments on partially wetting substrates: From micrometric to nanometric scales. *Braz. J. Phys.*, 46(2):225–237, 2016.
- [dGBWQ04] P.-G. de Gennes, F. Brochard-Wyart, and D. Quéré. *Capillarity and Wetting Phenomena: Drops, Bubbles, Pearls, Waves*. Springer Science & Business Media, New York, 2004.
- [DGK09] J. A. Diez, A. G. González, and L. Kondic. On the breakup of fluid rivulets. *Phys. Fluids*, 21(8):82105, 2009.
- [DKK91a] E. Doedel, H. B. Keller, and J. P. Kernevez. Numerical analysis and control of bifurcation problems (I) Bifurcation in finite dimensions. *Int. J. Bifurc. Chaos*, 1(3):493–520, 1991.
- [DKK91b] E. Doedel, H. B. Keller, and J. P. Kernevez. Numerical analysis and control of bifurcation problems (II) Bifurcation in infinite dimensions. *Int. J. Bifurc. Chaos*, 1(4):745–772, 1991.
- [DL83] G. Dee and J. S. Langer. Propagating pattern selection. *Phys. Rev. Lett.*, 50(6):383, 1983.
- [Doi11] M. Doi. Onsager’s variational principle in soft matter. *J. Phys. Condens. Matter*, 23(28):284118, 2011.
- [Doi12] M. Doi. Onsager’s variational principle in soft matter dynamics. In S. Komura and T. Ohta, editors, *Non-Equilibrium Soft Matter Physics*, volume 4, pages 1–35. World Scientific, 2012.
- [Doi13] M. Doi. *Soft matter physics*. Oxford University Press, Oxford, 2013.
- [Doi15] M. Doi. Onsager principle as a tool for approximation. *Chin. Phys. B*, 24(020505):1056–1674, 2015.
- [Doi16] M. Doi. A principle in dynamic coarse graining—Onsager principle and its applications. *Eur. Phys. J. ST*, 225(8-9):1411–1421, 2016.
- [DOO12] E. J. Doedel, B. E. Oldeman, and Others. *AUTO-07P: Continuation and bifurcation software for ordinary differential equations*. Concordia University, Montreal Canada, 2012. Documentation of the software, available from <http://indy.cs.concordia.ca/auto/> (February 2018).
- [DW99] B. R. Duffy and S. K. Wilson. Thin-film and curtain flows on the outside of a rotating horizontal cylinder. *J. Fluid Mech.*, 394:29–49, 1999.
- [DWC⁺14] H. A. Dijkstra, F. W. Wubs, A. K. Cliffe, E. Doedel, I. Dragomirescu, B. Eckhardt, A. Y. Gelfgat, A. L. Hazel, V. Lucarini, A. G. Salinger, and Others. Numerical bifurcation methods and their application to fluid dynamics: analysis beyond simulation. *Commun. Comput. Phys.*, 15(1):1–45, 2014.
- [DXZD18] Y. Di, X. Xu, J. Zhou, and M. Doi. Thin film dynamics in coating problems using Onsager principle. *Chinese Phys. B*, 27(2):24501, 2018.

- [EGU⁺18] S. Engelnkemper, S. V. Gurevich, H. Uecker, D. Wetzel, and U. Thiele. Continuation for thin film hydrodynamics and related scalar problems. In A. Gelfgat, editor, *Computational Modeling of Bifurcations and Instabilities in Fluid Mechanics*. Springer, 2018. (at press).
- [Ein05] A. Einstein. Über die von der molekularkinetischen Theorie der Wärme geforderte Bewegung von in ruhenden Flüssigkeiten suspendierten Teilchen. *Ann. Phys.*, 322(8):549–560, 1905.
- [ELW⁺12] H. Emmerich, H. Löwen, R. Wittkowski, T. Gruhn, G. I. Tóth, G. Tegze, and L. Gránásy. Phase-field-crystal models for condensed matter dynamics on atomic length and diffusive time scales: an overview. *Adv. Phys.*, 61(6):665–743, 2012.
- [Eng17] S. Engelnkemper. *Nichtlineare Analyse physikochemisch getriebener Entnetzung - Statik und Dynamik -*. PhD thesis, University of Münster, 2017.
- [Eva79] R. Evans. Nature of the liquid-vapor interface and other topics in the statistical-mechanics of nonuniform, classical fluids. *Adv. Phys.*, 28(2):143–200, 1979.
- [EWGT16] S. Engelnkemper, M. Wilczek, S. V. Gurevich, and U. Thiele. Morphological transitions of sliding drops: Dynamics and bifurcations. *Phys. Rev. Fluids*, 1(7):73901, 2016.
- [Gal15] M. Galvagno. *Modelling of driven free surface liquid films*. PhD thesis, Loughborough University, 2015.
- [GDGG07] A. G. González, J. Diez, R. Gratton, and J. Gomba. Rupture of a fluid strip under partial wetting conditions. *EPL*, 77(4):44001, 2007.
- [GFS07] M. Ghosh, F. Fan, and K. J. Stebe. Spontaneous pattern formation by dip coating of colloidal suspensions on homogeneous surfaces. *Langmuir*, 23(4):2180–2183, 2007.
- [Gla05] K. B. Glasner. Variational models for moving contact lines and the quasi-static approximation. *Eur. J. Appl. Math.*, 16(6):713–740, 2005.
- [GNPS96] R. E. Goldstein, P. Nelson, T. Powers, and U. Seifert. Front propagation in the pearling instability of tubular vesicles. *J. Phys. II*, 6(5):767–796, 1996.
- [Gol80] H. Goldstein. *Classical mechanics*. Addison-Wesley, 2nd edition, 1980.
- [GORS09] K. Glasner, F. Otto, T. Rump, and D. Slepcev. Ostwald ripening of droplets: The role of migration. *Eur. J. Appl. Math.*, 20(1):1–67, 2009.
- [GPDM03] J.-F. Gouyet, M. Plapp, W. Dieterich, and P. Maass. Description of far-from-equilibrium processes by mean-field lattice gas models. *Adv. Phys.*, 52(6):523–638, 2003.
- [GTLT14] M. Galvagno, D. Tseluiko, H. Lopez, and U. Thiele. Continuous and Discontinuous Dynamic Unbinding Transitions in Drawn Film Flow. *Phys. Rev. Lett.*, 112(13):137803, 2014.

-
- [GW03] K. B. Glasner and T. P. Witelski. Coarsening dynamics of dewetting films. *Phys. Rev. E*, 67(1):16302, 2003.
- [GW08] M. B. Gratton and T. P. Witelski. Coarsening of unstable thin films subject to gravity. *Phys. Rev. E*, 77(1):16301, 2008.
- [GW09] M. B. Gratton and T. P. Witelski. Transient and self-similar dynamics in thin film coarsening. *Physica D*, 238(23-24):2380–2394, 2009.
- [Hak04] H. Haken. *Synergetics: Introduction and Advanced Topics*. Springer-Verlag, Berlin, 2004.
- [HJ00] G. Henkelman and H. Jónsson. Improved tangent estimate in the nudged elastic band method for finding minimum energy paths and saddle points. *J. Chem. Phys.*, 113(22):9978–9985, 2000.
- [HJJ02] G. Henkelman, G. Jóhannesson, and H. Jónsson. Methods for Finding Saddle Points and Minimum Energy Paths. In Steven D Schwartz, editor, *Theor. Methods Condens. Phase Chem.*, pages 269–302, Dordrecht, 2002. Springer Netherlands.
- [HJM⁺98] S. Herminghaus, K. Jacobs, K. Mecke, J. Bischof, A. Fery, M. Ibn-Elhaj, and S. Schlagowski. Spinodal dewetting in liquid crystal and liquid metal films. *Science*, 282(5390):916–919, 1998.
- [HL12] W. Han and Z. Lin. Learning from "Coffee Rings": Ordered Structures Enabled by Controlled Evaporative Self-Assembly. *Angew. Chem. Int. Ed.*, 51(7):1534–1546, 2012.
- [HLH⁺15] C. Honisch, T.-S. Lin, A. Heuer, U. Thiele, and S. V. Gurevich. Instabilities of Layers of Deposited Molecules on Chemically Stripe Patterned Substrates: Ridges versus Drops. *Langmuir*, 31(38):10618–10631, 2015.
- [Hon13] C. Honisch. *Analysis of complex systems: From stochastic time series to pattern formation in microscopic fluidic films*. PhD thesis, University of Münster, 2013.
- [HS71] C. Huh and L. E. Scriven. Hydrodynamic model of steady movement of a solid/liquid/fluid contact line. *J. Colloid Interf. Sci.*, 35(1):85–101, 1971.
- [HTA14] A. P. Hughes, U. Thiele, and A. J. Archer. An introduction to inhomogeneous liquids, density functional theory, and the wetting transition. *Am. J. Phys.*, 82(12):1119–1129, 2014.
- [HTA15] A. P. Hughes, U. Thiele, and A. J. Archer. Liquid drops on a surface: Using density functional theory to calculate the binding potential and drop profiles and comparing with results from mesoscopic modelling. *J. Chem. Phys.*, 142(7):74702, 2015.
- [HTA17] A. P. Hughes, U. Thiele, and A. J. Archer. Influence of the fluid structure on the binding potential: comparing liquid drop profiles from density functional theory with results from mesoscopic theory. *J. Chem. Phys.*, 146(6):64705, 2017.

- [IT07] T. Ingebrigtsen and S. Toxvaerd. Contact angles of Lennard-Jones liquids and droplets on planar surfaces. *J. Phys. Chem. C*, 111(24):8518–8523, 2007.
- [Kaw72] K. Kawasaki. Kinetics of ising models. In C. Domb and M. S. Green, editors, *Phase transitions and critical phenomena*, volume 2, pages 443–501, New York, 1972. Academic Press.
- [Kel09] M. A. Kelmanson. On inertial effects in the Moffatt-Pukhnachov coating-flow problem. *J. Fluid Mech.*, 633:327–353, 2009.
- [KGFT12] M. H. Köpf, S. V. Gurevich, R. Friedrich, and U. Thiele. Substrate-mediated pattern formation in monolayer transfer: a reduced model. *New J. Phys.*, 14(2):23016, 2012.
- [KLRD06] J. Koplik, T. S. Lo, M. Rauscher, and S. Dietrich. Pearling instability of nanoscale fluid flow confined to a chemical channel. *Phys. Fluids*, 18(3):32104, 2006.
- [KN17] M. Kanduc and R. R. Netz. Atomistic simulations of wetting properties and water films on hydrophilic surfaces. *J. Chem. Phys.*, 146(16):164705, 2017.
- [Köp11] M. H. Köpf. *On the dynamics of surfactant covered thin liquid films and the formation of stripe patterns in Langmuir-Blodgett transfer*. PhD thesis, University of Münster, 2011.
- [KPB02] J. Koplik, S. Pal, and J. R. Banavar. Dynamics of nanoscale droplets. *Phys. Rev. E*, 65(2):21504, 2002.
- [KPP37] A. Kolmogorov, L. Petrovsky, and N. Piskunov. An investigation of the diffusion equation combined with an increase in mass and its application to a biological problem. *Bull. Uni. Moscow Ser. Int. A*, 1(6):1–26, 1937.
- [KT14] M. H. Köpf and U. Thiele. Emergence of the bifurcation structure of a Langmuir-Blodgett transfer model. *Nonlinearity*, 27(11):2711–2734, 2014.
- [Lar14] R. G. Larson. Transport and deposition patterns in drying sessile droplets. *Aiche J.*, 60:1538–1571, 2014.
- [LBE12] J. Löber, M. Bär, and H. Engel. Front propagation in one-dimensional spatially periodic bistable media. *Phys. Rev. E*, 86(6):66210, 2012.
- [LCK18] M.-A. Y.-H. Lam, L. J. Cummings, and L. Kondic. Stability of thin fluid films characterised by a complex form of effective disjoining pressure. *J. Fluid Mech.*, 841:925–961, 2018.
- [LL42] L. Landau and B. Levich. Dragging of a liquid by a moving plane. *Acta Physicochim. URSS*, 17:42, 1942.
- [LL66a] L. D. Landau and E. M. Lifschitz. *Klassische Feldtheorie*. Akademie Verlag, Berlin, 1966.
- [LL66b] L. D. Landau and E. M. Lifschitz. *Mechanik*. Akademie Verlag, Berlin, 1966.

-
- [LL91] L. D. Landau and E. M. Lifschitz. *Hydrodynamik*. Akademie Verlag, Berlin, 1991.
- [LMW⁺12] F. Lied, T. Mues, W. Wang, L. Chi, and A. Heuer. Different growth regimes on prepatterned surfaces: Consistent evidence from simulations and experiments. *J. Chem. Phys.*, 136(2):24704, 2012.
- [LRTT16] T.-S. Lin, S. Rogers, D. Tseluiko, and U. Thiele. Bifurcation analysis of the behavior of partially wetting liquids on a rotating cylinder. *Phys. Fluids*, 28(8):82102, 2016.
- [LS61] I. M. Lifshitz and V. V. Slyozov. The kinetics of precipitation from supersaturated solid solutions. *J. Phys. Chem. Solids*, 19(1-2):35–50, 1961.
- [Lut08] J. F. Lutsko. Theoretical description of the nucleation of vapor bubbles in a superheated fluid. *EPL*, 83(4):46007, 2008.
- [MBKP14] L. G. MacDowell, J. Benet, N. A. Katcho, and J. M. G. Palanco. Disjoining pressure and the film-height-dependent surface tension of thin liquid films: New insight from capillary wave fluctuations. *Adv. Colloid Interface Sci.*, 206:150–171, 2014.
- [MC00] P. C. Matthews and S. M. Cox. Pattern formation with a conservation law. *Nonlinearity*, 13(4):1293, 2000.
- [MD16] X. Man and M. Doi. Ring to mountain transition in deposition pattern of drying droplets. *Phys. Rev. Lett.*, 116(6):66101, 2016.
- [MD17] X. Man and M. Doi. Vapor-Induced Motion of Liquid Droplets on an Inert Substrate. *Phys. Rev. Lett.*, 119(4):44502, 2017.
- [Mea92a] P. Meakin. Droplet deposition growth and coalescence. *Rep. Prog. Phys.*, 55(2):157, 1992.
- [Mea92b] P. Meakin. Steady state behavior in a model for droplet growth, sliding and coalescence: the final stage of dropwise condensation. *Physica A*, 183(4):422–438, 1992.
- [Min15] E. Minguzzi. Rayleigh’s dissipation function at work. *Eur. J. Phys.*, 36(3):35014, 2015.
- [Mit93] V. S. Mitlin. Dewetting of solid surface: Analogy with spinodal decomposition. *J. Colloid Interf. Sci.*, 156(2):491–497, 1993.
- [MM17] M. Morozov and O. Manor. An extended Landau-Levich model for the dragging of a thin liquid film with a propagating surface acoustic wave. *J. Fluid Mech.*, 810:307–322, 2017.
- [Mof77] H. K. Moffatt. Behaviour of a viscous film on the outer surface of a rotating cylinder. *J. mécanique*, 16(5):651–673, 1977.
- [Mon08] P. A. Monson. Mean field kinetic theory for a lattice gas model of fluids confined in porous materials. *J. Chem. Phys.*, 128(8):84701, 2008.

- [MOR⁺07] S. Mechkov, G. Oshanin, M. Rauscher, M. Brinkmann, A. M. Cazabat, and S. Dietrich. Contact line stability of ridges and drops. *EPL*, 80(6):66002, 2007.
- [MRD08] S. Mechkov, M. Rauscher, and S. Dietrich. Stability of liquid ridges on chemical micro- and nanostripes. *Phys. Rev. E*, 77(6):61605, 2008.
- [MRR⁺53] N. Metropolis, A. W. Rosenbluth, M. N. Rosenbluth, A. H. Teller, and E. Teller. Equation of State Calculations by Fast Computing Machines. *J. Chem. Phys.*, 21(6):1087–1092, 1953.
- [MT99] U. M. B. Marconi and P. Tarazona. Dynamic density functional theory of fluids. *J. Chem. Phys.*, 110(16):8032–8044, 1999.
- [MT00] U. M. B. Marconi and P. Tarazona. Dynamic density functional theory of fluids. *J. Phys. Condens. Matter*, 12(8A):A413, 2000.
- [ODB97] A. Oron, S. H. Davis, and S. G. Bankoff. Long-scale evolution of thin liquid films. *Rev. Mod. Phys.*, 69(3):931, 1997.
- [Ons31a] L. Onsager. Reciprocal relations in irreversible processes. I. *Phys. Rev.*, 37(4):405, 1931.
- [Ons31b] L. Onsager. Reciprocal relations in irreversible processes. II. *Phys. Rev.*, 38(12):2265, 1931.
- [ORS06] F. Otto, T. Rump, and D. Slepcev. Coarsening rates for a droplet model: rigorous upper bounds. *SIAM J. Math. Anal.*, 38(2):503–529, 2006.
- [Ost96] W. Ostwald. *Lehrbuch der Allgemeinen Chemie*, volume 2. Leipzig, Germany, 1896.
- [Ost97] W. Ostwald. Studien über die Bildung und Umwandlung fester Körper. *Z. Phys. Chem.*, 22:289–330, 1897.
- [PB92] S. Puri and K. Binder. Surface-directed spinodal decomposition: phenomenology and numerical results. *Phys. Rev. A*, 46(8):R4487, 1992.
- [PFL01] T. Podgorski, J.-M. Flesselles, and L. Limat. Corners, cusps, and pearls in running drops. *Phys. Rev. Lett.*, 87(3):36102, 2001.
- [PG97] T. R. Powers and R. E. Goldstein. Pearling and pinching: propagation of Rayleigh instabilities. *Phys. Rev. Lett.*, 78(13):2555, 1997.
- [Pis01] L. M. Pismen. Nonlocal diffuse interface theory of thin films and the moving contact line. *Phys. Rev. E*, 64(2):21603, 2001.
- [Pis04] L. M. Pismen. Spinodal dewetting in a volatile liquid film. *Phys. Rev. E*, 70(2):21601, 2004.
- [Pis06] L. M. Pismen. *Patterns and interfaces in dissipative dynamics*. Springer Science & Business Media, 2006.

-
- [Pla73] J. A. F. Plateau. *Statique expérimentale et théorique des liquides soumis aux seules forces moléculaires*, volume 2. Gauthier-Villars, 1873.
- [PP00] L. M. Pismen and Y. Pomeau. Disjoining potential and spreading of thin liquid layers in the diffuse-interface model coupled to hydrodynamics. *Phys. Rev. E*, 62(2):2480, 2000.
- [PP04] L. M. Pismen and Y. Pomeau. Mobility and interactions of weakly nonwetting droplets. *Phys. Fluids*, 16(7):2604–2612, 2004.
- [Puk77] V. V. Pukhnachev. The liquid film motion on the rotating cylinder surface at the presence of gravity. *Prikl. Mekh. Teor. Fiz.*, 3:77–88, 1977.
- [PZGS98] T. R. Powers, D. Zhang, R. E. Goldstein, and H. A. Stone. Propagation of a topological transition: The Rayleigh instability. *Phys. Fluids*, 10(5):1052–1057, 1998.
- [QWL⁺09] T. Qian, C. Wu, S. L. Lei, X.-P. Wang, and P. Sheng. Modeling and simulations for molecular scale hydrodynamics of the moving contact line in immiscible two-phase flows. *J. Phys. Condens. Matter*, 21(46):464119, 2009.
- [QWS06] T. Qian, X.-P. Wang, and P. Sheng. A variational approach to moving contact line hydrodynamics. *J. Fluid Mech.*, 564:333–360, 2006.
- [Rit09] W. Ritz. Über eine neue Methode zur Lösung gewisser Variationsprobleme der mathematischen Physik. *J. für die reine und Angew. Math.*, 135:1–61, 1909.
- [RRGB03] E. Rabani, D. R. Reichman, P. L. Geissler, and L. E. Brus. Drying-mediated self-assembly of nanoparticles. *Nature*, 426(6964):271–274, 2003.
- [SADF07] J. H. Snoeijer, B. Andreotti, G. Delon, and M. Fermigier. Relaxation of a dewetting contact line. Part 1. A full-scale hydrodynamic calculation. *J. Fluid Mech.*, 579:63–83, 2007.
- [Sch17] A. Scheel. Spinodal decomposition and coarsening fronts in the Cahn–Hilliard equation. *J. Dyn. Differ. Equations*, 29(2):431–464, 2017.
- [SH77] J. Swift and P. C. Hohenberg. Hydrodynamic fluctuations at the convective instability. *Phys. Rev. A*, 15(1):319, 1977.
- [SHJ01] R. Seemann, S. Herminghaus, and K. Jacobs. Shape of a liquid front upon dewetting. *Phys. Rev. Lett.*, 87(19):196101, 2001.
- [SHR05] C. G. Sztrum, O. Hod, and E. Rabani. Self-assembly of nanoparticles in three-dimensions: Formation of stalagmites. *J. Phys. Chem. B*, 109(14):6741–6747, 2005.
- [Smo16] M. V. Smoluchowski. Drei Vorträge über Diffusion, Brownsche Bewegung und Koagulation von Kolloidteilchen. *Z. Phys.*, 17:557–585, 1916.
- [Str78] J. W. Strutt, 3rd Baron Rayleigh. On the instability of jets. *Proc. London Math. Soc.*, 1(1):4–13, 1878.

- [Str94] J. W. Strutt, 3rd Baron Rayleigh. *The Theory Of Sound Vol. 1*. Macmillan and co., London, 1894.
- [Str14] S. H. Strogatz. *Nonlinear Dynamics and Chaos*. Westview Press, Boulder, Colorado, 2nd edition, 2014.
- [SW09] Y. Sun and E. B. Webb. The atomistic mechanism of high temperature contact line advancement: results from molecular dynamics simulations. *J. Phys. Condens. Matter*, 21(46):464135, 2009.
- [SZA⁺08] J. H. Snoeijer, J. Ziegler, B. Andreotti, M. Fermigier, and J. Eggers. Thick films of viscous fluid coating a plate withdrawn from a liquid reservoir. *Phys. Rev. Lett.*, 100(24):244502, 2008.
- [TAR⁺13] U. Thiele, A. J. Archer, M. J. Robbins, H. Gomez, and E. Knobloch. Localized states in the conserved Swift-Hohenberg equation with cubic nonlinearity. *Phys. Rev. E*, 87(4):42915, 2013.
- [TBBB03] U. Thiele, L. Bruschi, M. Bestehorn, and M. Bär. Modelling thin-film dewetting on structured substrates and templates: Bifurcation analysis and numerical simulations. *Eur. Phys. J. E*, 11(3):255–271, 2003.
- [TBH⁺17] W. Tewes, O. Buller, A. Heuer, U. Thiele, and S. V. Gurevich. Comparing kinetic Monte Carlo and thin-film modeling of transversal instabilities of ridges on patterned substrates. *J. Chem. Phys.*, 146(9):94704, 2017.
- [TGT14] D. Tseluiko, M. Galvagno, and U. Thiele. Collapsed heteroclinic snaking near a heteroclinic chain in dragged meniscus problems. *Eur. Phys. J. E*, 37(4):33, 2014.
- [Thi07] U. Thiele. Structure formation in thin liquid films. In S. Kalliadasis and U. Thiele, editors, *Thin Film. Soft Matter*, pages 25–93, Wien, 2007. Springer.
- [Thi10] U. Thiele. Thin film evolution equations from (evaporating) dewetting liquid layers to epitaxial growth. *J. Phys. Condens. Matter*, 22(8):84019, 2010.
- [Thi11] U. Thiele. On the depinning of a drop of partially wetting liquid on a rotating cylinder. *J. Fluid Mech.*, 671:121–136, 2011.
- [Thi14] U. Thiele. Patterned deposition at moving contact lines. *Adv. Colloid Interface Sci.*, 206:399–413, 2014.
- [TK06] U. Thiele and E. Knobloch. Driven drops on heterogeneous substrates: Onset of sliding motion. *Phys. Rev. Lett.*, 97(20):204501, 2006.
- [TKG14] U. Thiele, O. Kamps, and S. V. Gurevich, editors. *Münsterian Torturials on Nonlinear Science: Continuation*. CeNoS, Münster, 2014. <http://www.uni-muenster.de/CeNoS/Lehre/Tutorials/continuation.html> (last visited 01.02.2018).
- [TMTT13] N. Tretyakov, M. Müller, D. Todorova, and U. Thiele. Parameter passing between molecular dynamics and continuum models for droplets on solid substrates: The static case. *J. Chem. Phys.*, 138(6):64905, 2013.

-
- [TNB⁺02] U. Thiele, K. Neuffer, M. Bestehorn, Y. Pomeau, and M. G. Velarde. Sliding drops on an inclined plane. *Colloids Surf. A*, 206(1-3):87–104, 2002.
- [Tom00] H. Tomita. An explicit form of the equation of motion of the interface in bicontinuous phases. *Progr. Theor. Phys.*, 104(2):307–324, 2000.
- [TSTG17] F. Tabbert, C. Schelte, M. Tlidi, and S. V. Gurevich. Delay-induced depinning of localized structures in a spatially inhomogeneous Swift-Hohenberg model. *Phys. Rev. E*, 95(3):32213, 2017.
- [TVN01a] U. Thiele, M. G. Velarde, and K. Neuffer. Dewetting: Film rupture by nucleation in the spinodal regime. *Phys. Rev. Lett.*, 87(1):16104, 2001.
- [TVN⁺01b] U. Thiele, M. G. Velarde, K. Neuffer, M. Bestehorn, and Y. Pomeau. Sliding drops in the diffuse interface model coupled to hydrodynamics. *Phys. Rev. E*, 64(6):61601, 2001.
- [TWGT18] W. Tewes, M. Wilczek, S. V. Gurevich, and U. Thiele. Self-organised dip-coating patterns of simple, partially wetting, nonvolatile liquids. *In preparation*, 2018.
- [Van03] W. Van Saarloos. Front propagation into unstable states. *Phys. Rep.*, 386(2-6):29–222, 2003.
- [vHHvS94] M. van Hecke, P. C. Hohenberg, and W. van Saarloos. Amplitude equations for pattern forming systems. In H. van Beijeren and M. H. Ernst, editors, *Fundamental Problems in Statistical Mechanics VIII*, pages 245–278, Amsterdam, 1994. North-Holland.
- [vTH18] A. von Borries Lopes, U. Thiele, and A. L. Hazel. On the multiple solutions of coating and rimming flows on rotating cylinders. *J. Fluid Mech.*, 835:540–574, 2018.
- [Wag61] C. Wagner. Theorie der Alterung von Niederschlägen durch Umlösen (Ostwald-Reifung). *Ber. Bunsenges. Phys. Chem.*, 65(7-8):581–591, 1961.
- [WC12] W. Wang and L. Chi. Area-selective growth of functional molecular architectures. *Acc. Chem. Res.*, 45(10):1646–1656, 2012.
- [WDW⁺11] W. Wang, C. Du, C. Wang, M. Hirtz, L. Li, J. Hao, Q. Wu, R. Lu, N. Lu, Y. Wang, and Others. High-Resolution Triple-Color Patterns Based on the Liquid Behavior of Organic Molecules. *small*, 7(10):1403–1406, 2011.
- [Wil16] M. Wilczek. *Pattern Formation in Driven Thin Layers of Simple and Complex Liquids*. PhD thesis, University of Münster, 2016.
- [WTE⁺17] M. Wilczek, W. Tewes, S. Engelkemper, S. V. Gurevich, and U. Thiele. Sliding Drops: Ensemble Statistics from Single Drop Bifurcations. *Phys. Rev. Lett.*, 119(20):204501, 2017.
- [WTG⁺15] M. Wilczek, W. B. H. Tewes, S. V. Gurevich, M. H. Köpf, L. F. Chi, and U. Thiele. Modelling pattern formation in dip-coating experiments. *Math. Model. Nat. Phenom.*, 10(4):44–60, 2015.

- [WZC⁺16] M. Wilczek, J. Zhu, L. Chi, U. Thiele, and S. V. Gurevich. Dip-coating with prestructured substrates: transfer of simple liquids and Langmuir–Blodgett monolayers. *J. Phys. Condens. Matter*, 29(1):14002, 2016.
- [XDD16] X. Xu, Y. Di, and M. Doi. Variational method for liquids moving on a substrate. *Phys. Fluids*, 28(8):87101, 2016.
- [XQ17] X. Xu and T. Qian. Hydrodynamic boundary conditions derived from Onsager’s variational principle. *Procedia IUTAM*, 20:144–151, 2017.
- [XTQ15] X. Xu, U. Thiele, and T. Qian. A variational approach to thin film hydrodynamics of binary mixtures. *J. Phys. Condens. Matter*, 27(8):85005, 2015.

Danksagung

Zum Ende dieser Arbeit möchte ich mich bedanken bei:

- Prof. Dr. Uwe Thiele für die unkomplizierte und sehr engagierte Betreuung meiner Promotion und seine wertvolle Unterstützung in vielen Fragen.
- Prof. Dr. Andreas Heuer für die freundliche Betreuung und die angenehme Zusammenarbeit.
- Dr. Svetlana Gurevich für ihr stets offenes Ohr und ihre sehr hilfsbereite Betreuung seit vielen Jahren.
- Dem deutsch-chinesischen Kollaborationsprojekt Transregio 61 für die finanzielle Unterstützung und interessante Auslandsaufenthalte.
- Prof. Dr. Andrew Archer für eine spannende Zusammenarbeit und aufschlussreiche Diskussionen.
- Oleg Buller für eine sehr angenehme Kooperation.
- Dr. Markus Wilczek für viele spannende Kooperationen, Diskussionen und Reisen, sowie seine beispiellose Hilfsbereitschaft in vielen Fragen.
- Meinen Bürokollegen Felix Tabbert, Sebastian Engelnkemper und Phong-Minh Timmy Ly für eine sehr angenehme Atmosphäre während der Arbeit.
- Meinen Korrekturlesern Sarah Trinschek, Svetlana Gurevich, Felix Tabbert, Ida Tewes, Markus Wilczek, Uwe Thiele, Tobias Frohoff-Hülsmann, Evgenij Travkin und Christian Barthel für viele Verbesserungen.
- Der gesamten Arbeitsgruppe Thiele für eine angenehme Atmosphäre und schöne Fahrten zur Zaferna Hütte.
- Prof. Dr. Jacco Snoeijer für das entgegengebrachte Vertrauen zum Ende der Arbeit.
- Nikolaus Krause, Christian Barthel und Evgenij Travkin für moralische und technische Unterstützung in der schwierigen Endphase der Arbeit.
- Meinen Eltern, sowie meiner Schwester Ida, für ihre bedingungslose Unterstützung während meines gesamten Lebens.

Lebenslauf

Name Walter Bernard Hans Tewes
Geburtsdatum 19.06.1991
Geburtsort Höxter
Staatsangehörigkeit deutsch
Familienstand ledig
Eltern Ulrike Piderit-Tewes, Walter Tewes

Schulbildung

1997–2000 Kath. Grundschule Kollerbeck
2000–2008 Städtisches Gymnasium Steinheim
20.06.2008 Allgemeine Hochschulreife (Note 1,3)

Studium

10/2008–08/2011 Bachelorstudium der Physik an der Westfälischen Wilhelms-Universität Münster
16.08.2011 Abschluss Bachelor of Science in Physik (Note 1,2)
Thema der Bachelorarbeit:
Relative Dispersion Lagrange'scher Teilchen
in der turbulenten inversen Kaskade
03.2010–10.2012 Bachelorstudium 2-Fach Mathematik und Physik an der Westfälischen Wilhelms-Universität Münster
02.10.2012 Abschluss 2-Fach Bachelor of Science
in Mathematik und Physik (Note 1,3)
10/2011–12/2013 Masterstudium der Physik an der Westfälischen Wilhelms-Universität Münster
06.12.2013 Abschluss Master of Science in Physik (Note 1,0)
Thema der Masterarbeit: A Theoretical Description
of Pattern Formation in Thin Solution Layers

Promotionsstudium

seit 01/2014 Promotionsstudium am Institut für Theoretische Physik
der Westfälischen Wilhelms-Universität Münster
unter der Betreuung von Prof. Dr. Uwe Thiele

Berufstätigkeit

04/2010–09/2010 Studentische Hilfskraft am Institut für Didaktik
der Physik der Universität Münster

10/2011–03/2012 Studentische Hilfskraft am Mathematischen Institut
der Universität Münster

10/2012–12/2013 Studentische Hilfskraft am Institut für Theoretische Physik
der Universität Münster

01/2014–02/2018 Wissenschaftlicher Mitarbeiter am Institut
für Theoretische Physik der Universität Münster

seit 03/2018 Wissenschaftlicher Mitarbeiter an der Universität Twente,
Niederlande